NOTE TO USERS

This reproduction is the best copy available.

UMI®

An Investigation of a Compact Micro-optic and Micromirror-based Optical Power Equalizer

Xuyen D. Hoa

Department of Electrical and Computer Engineering
McGill University
Montreal, Quebec, Canada
May 2004

A thesis submitted to the Faculty of Graduate Studies and Research in partial fulfillment of the requirements of the degree of Master of Engineering.

© Xuyen D. Hoa, 2004

Library and Archives Canada

Published Heritage Branch

395 Wellington Street
Ottawa ON K1A 0N4
Canada

Bibliothèque et Archives Canada

Direction du Patrimoine de l'édition

395, rue Wellington
Ottawa ON K1A 0N4
Canada

Your file Votre référence
ISBN: 0-494-06556-7
Our file Notre référence
ISBN: 0-494-06556-7

NOTICE:
The author has granted a non-exclusive license allowing Library and Archives Canada to reproduce, publish, archive, preserve, conserve, communicate to the public by telecommunication or on the Internet, loan, distribute and sell theses worldwide, for commercial or non-commercial purposes, in microform, paper, electronic and/or any other formats.

The author retains copyright ownership and moral rights in this thesis. Neither the thesis nor substantial extracts from it may be printed or otherwise reproduced without the author's permission.

AVIS:
L'auteur a accordé une licence non exclusive permettant à la Bibliothèque et Archives Canada de reproduire, publier, archiver, sauvegarder, conserver, transmettre au public par télécommunication ou par l'Internet, prêter, distribuer et vendre des thèses partout dans le monde, à des fins commerciales ou autres, sur support microforme, papier, électronique et/ou autres formats.

L'auteur conserve la propriété du droit d'auteur et des droits moraux qui protège cette thèse. Ni la thèse ni des extraits substantiels de celle-ci ne doivent être imprimés ou autrement reproduits sans son autorisation.

In compliance with the Canadian Privacy Act some supporting forms may have been removed from this thesis.

While these forms may be included in the document page count, their removal does not represent any loss of content from the thesis.

Conformément à la loi canadienne sur la protection de la vie privée, quelques formulaires secondaires ont été enlevés de cette thèse.

Bien que ces formulaires aient inclus dans la pagination, il n'y aura aucun contenu manquant.

Abstract

This thesis examines the design and characterisation of a compact optical power equalizer module for optical fiber telecommunication applications. The various components of the modules are separately examined in terms of their impact on the overall dimension, performance and loss of the equalizer module. Two components are studied in greater details, namely the micro diffractive optical elements (DOEs), responsible for the multiplexing/demultiplexing of the wavelength channels, and the micromirrors, responsible for creating the beam displacements and thus controlling the attenuation. The DOEs allow for the spatial separation of 64 wavelengths into a two-dimensional array with a compact module. MUMPs surface-micromachined micromirrors have good optical properties: 0.29 dB (93.5%) reflectance, low surface sag and negligible curvature. At operating voltages of less than 15 V, tilts of 16 mrad are obtained, sufficient to provide over 50 dB attenuation for the equalizer. Simulation results show that the diffractive elements have low efficiency due to fabrication limitations. The power loss due to beam clipping is 2.81 dB with overall system efficiency at above 5 dB. Major areas of improvement in the device packaging, assembly and efficiency have been identified for future works.

Sommaire

Cette thèse examine la conception et la caractérisation d'un module compact d'égaliseur de puissance optique pour des applications de télécommunication en fibres optiques. Les divers composants du module sont examinés pour leur impact sur la dimension, la performance et les pertes du module d'égaliseur. Deux composants sont étudiés dans de plus amples détails, à savoir les micro-éléments optiques diffractifs, responsable du multiplexage et démultiplexage des 64 canaux ou longueurs d'onde, et les micromirrors, responsable du déplacement de faisceau créant l'atténuation optique. Les éléments diffractifs permettent la séparation spatiale des 64 longueurs d'onde et la organisation des 64 longueurs d'onde en un vecteur bidimensionnel de façon compacte. Les micromirrors fabriqué par micro usinage de surface (MUMPs) ont de bonnes propriétés optiques: 0.29 dB (93.5%) de réflectivité, fléchissement et courbure des surfaces négligeables. Avec une potentiel électrique de moins de 15 V, des inclinaisons de surface de 16 mrad sont obtenues, suffisamment pour fournir une atténuation de plus de 50 dB. Les résultats démontrent que l'efficacité des éléments diffractifs est limité par les processus de fabrication. Les pertes dues au diaphragme des composants sont de 2.81 dB et l'efficacité total du system est au-delà de 5 dB. Plusieurs améliorations sont identifiées. Le dispositif d'assemblage et l'efficacité des composants sont identifiés pour les travaux futurs.

Acknowledgements

This work would have not been possible without the guidance and support of Dr. Andrew Kirk. His advices, teaching and supervision are greatly appreciated. Also, I would like acknowledge members of the MEMS team: Reza Jafari, Cristina Marinescu, James Prentice, Marc Simard, and Seyed Mohammad Ali Soleymani for their assistance provided over the term of this project. Special thanks go to Juliana E. Lin for getting me interested and started in the MEMS domain. Her technical support was very helpful. Special thanks also go to Frédéric-Thomas Dupuis for this work on the micro-optic (de)multiplexer.

To the many members of the Photonic Systems Group, both past and present, and in particular my office mates in MC-848, thank you. Often, you added drama to an otherwise dull day. Your advices, expertises, and likewise your sense of humour were greatly needed and appreciated. Finally, I would like thank my family and friends, near and far, for their love and encouragement.

This work was completed with financial supports from the Postgraduate Scholarship Program of the National Sciences and Engineering Research Council (NSERC) of Canada, and with additional funding from the Canadian Institute for Telecommunications Research (CITR) and the Canadian Institute for Photonic Innovations (CIPI). This work is also made possible with MEMS fabrication grants from the Canadian Microelectronics Corporation (CMC).

Table of Contents

1 INTRODUCTION 1

1.1 MOTIVATION AND OBJECTIVE 2
1.2 THESIS OUTLINE 6
1.3 BRIEF SYSTEM DESCRIPTION 7

2 LITERATURE REVIEW 9

2.1 SURVEY OF OPTICAL EQUALIZER RESEARCH 9
2.1.1 WAVEGUIDE-BASED AND THERMO-OPTIC-BASED EQUALIZERS 9
2.1.2 AMPLIFIER-BASED EQUALIZERS 12
2.1.3 MEMS-BASED EQUALIZERS 13
2.1.4 ANOTHER EQUALIZER: *USING* ACOUSTO-OPTICS 14
2.1.5 EVALUATION OF DESIGNS 15
2.2 SURVEY OF MEMS MICROMIRROR RESEARCH 19
2.2.1 A BRIEF HISTORY OF MEMS MICROMIRRORS 19

3 MICRO-OPTICS AND MICROMIRROR-BASED EQUALIZER 22

3.1 OVERVIEW 22
3.2 SYSTEM REQUIREMENTS 22
3.3 SYSTEM COMPONENTS 23
3.3.1 OPTICAL CIRCULATOR 24
3.3.2 DISPERSION MODULE 25
3.3.3 REDIRECTION MODULE 29
3.3.4 MICROLENS TELESCOPE 32
3.3.5 POLYSILICON MICROMIRROR ARRAYS 34

4 MEMS MICROMIRRORS 36

4.1 DESIGN 36
4.1.1 FABRICATION: BULK VS. SURFACE-MICROMACHINING 36

4.1.2 MUMPs: *M*ULTI-*U*SER *M*EMS *P*ROCESSE*S* 38
4.1.3 DESIGN REQUIREMENTS 39
4.1.4 ELECTROSTATIC ROTATIONAL MICROMIRRORS 41
4.1.4.1 Design 1: *Electro_1* 41
4.1.4.2 Design 2: *Electro_2* 42
4.1.5 THERMAL ROTATIONAL PISTON MICROMIRRORS 42
4.1.5.1 *Thermo_1* 43
4.2 MICROMIRROR NUMERICAL MODELS 44
4.2.1 SIMPLIFIED MODELS: ELECTROSTATIC CAPACITOR MODELS 44
4.2.2 FINITE ELEMENT MODEL (FEM) 48
4.2.2.1 *Electro_1* 49
4.2.2.2 *Electro_2* 50
4.2.2.3 *Thermo_1* 51
4.3 MICROMIRROR EXPERIMENTAL CHARACTERISATION 53
4.3.1 ELECTROMECHANICAL CHARACTERISTICS 54
4.3.1.1 *Electro_1* 54
4.3.1.2 *Electro_2* 55
4.3.1.3 *Thermo_1* 56
4.3.2 OPTICAL AND SURFACE CHARACTERISTICS 56
4.3.2.1 Surface Curvature 57
4.3.2.2 Reflectivity 58

5 EQUALIZER MODELLING AND CHARACTERISATION 61

5.1 EQUALIZER ATTENUATION MODELING 61
5.1.1 MODELLING CONSIDERATIONS 62
5.1.2 CODE V MODELLING 65
5.1.2.1 Gaussian Beam Analysis 67
5.1.2.2 Coupling Loss vs. Tilt 69
5.1.2.3 Efficiency 71
5.1.3 SIMULATION CONCLUSIONS 73
5.2 EQUALIZER EXPERIMENTAL CHARACTERISATION 73

6 CONCLUSION 76

6.1 FUTURE WORK 77
6.1.1 CROSS-TALK ANALYSIS AND TOLERANCING 78
6.1.2 IMPROVED DIFFRACTIVE OPTICAL ELEMENTS AND MICROMIRROR DESIGNS 78
6.1.3 DYNAMIC FEEDBACK CONTROL AND INTEGRATION 79
6.2 SUMMARY 80

Appendix A Micromirror Chip Layout 83
Appendix B Matrix Analysis 84
Appendix C Code V 87
C.1 Lens Data Manager 87
C.2 System Visualization 88
C.3 Waist Analysis 89
C.3.1 Waist Size in System (with no Micromirror Curvature) 89
C.3.2 Waist Size in System (Micromirror Curvature R = 18.8mm) 90
C.3.3 Comparison of Waist (% Change) 91
Appendix D Gaussian Beam – Fiber Coupling 92

References 94

List of Figures

FIGURE 1.1: TYPICAL EDFA GAIN SPECTRUM 2

FIGURE 1.2: BIT-ERROR RATE VERSUS THE Q PARAMETER FOR TYPICAL OPTICAL RECEIVERS [4] 4

FIGURE 1.3: EQUALIZER – BLOCK DIAGRAM 6

FIGURE 1.4: OPERATION PRINCIPLES OF THE EQUALIZER 7

FIGURE 2.1: Y-BRANCH WAVEGUIDE ATTENUATOR [8] 10

FIGURE 2.2: MACH-ZEHNDER-BASED EQUALIZER 11

FIGURE 2.3: EDFA - AWG EQUALIZER 12

FIGURE 2.4: MEMS-BASED ATTENUATOR CONFIGURATIONS (A) BLOCKING VANE MECHANISM (B) REFLECTOR MECHANISM 14

FIGURE 2.5: ACOUSTO-OPTIC-BASED EQUALIZER 15

FIGURE 2.6: DEFORMABLE MEMBRANE 20

FIGURE 2.7: CANTILEVER MIRROR 20

FIGURE 3.1: EQUALIZER MODULE'S COMPONENTS 23

FIGURE 3.2: OPTICAL CIRCULATOR 24

FIGURE 3.3: UNFOLDED EQUALIZER SYSTEM 25

FIGURE 3.4: FREE-SPACE DISPERSION MODULE 26

FIGURE 3.5: AWG ON A PLC 27

FIGURE 3.6: FIBER-AWG INPUT CONNECTIONS VIA INTERMEDIATE PLC 29

FIGURE 3.7: DOE1 AND DOE2 30

FIGURE 3.8: BLAZED GRATING EQUATION 30

FIGURE 3.9: BLAZED GRATING VS. STEP GRATING 31

FIGURE 3.10: REDIRECTION MODULE 32

FIGURE 3.11: TELESCOPING LENSES 33

FIGURE 3.12: BULK VS. MICROLENSES 33

FIGURE 3.13: MICROMIRROR CONFIGURATION 34

FIGURE 4.1: BASIC SURFACE-MICROMACHINING PROCESS 37

FIGURE 4.2: MUMPS LAYERS AND STRUCTURES 38

FIGURE 4.3: SEM AND GEOMETRY OF ELECTR_1 MICROMIRROR 41

FIGURE 4.4: SEM AND GEOMETRY OF *ELECTRO_2* MICROMIRROR 42

FIGURE 4.5 SEM AND GEOMETRY OF *THERMO_1* MICROMIRROR 43

FIGURE 4.6: GENERALIZED TORSIONAL MICROMIRROR DESIGN 45

FIGURE 4.7: FLEXURE BEAM MICROMIRROR 46

FIGURE 4.8: TORSION BEAM MICROMIRROR 46

FIGURE 4.9: SMALL-ANGLE SOLUTIONS. THE MARKERS DENOTE THE PULL-IN POINT (A) SMALL TILT (ELECTROD_1) (B) LARGE TILT (*ELECTRO_2*) 47

FIGURE 4.10: *ELECTRO_1* SURFACE SAG 49
FIGURE 4.11: *ELECTRO_2* SURFACE SAG 50
FIGURE 4.12 *THERMO_1* SURFACE TILT AT REST 51
FIGURE 4.13: *THERMO_1* SURFACE TILT AT 17V 52
FIGURE 4.14: THERMO_2 TILT-VOLTAGE CHARACTERISTIC FOR FEM 53
FIGURE 4.16: *ELECTRO_1*- COMPARATIVE RESULTS 55
FIGURE 4.17: *ELECTRO_2* - COMPARATIVE RESULTS 56
FIGURE 4.18: SURFACE PROFILE/CURVATURE (A) *ELECTRO_2*: SURFACE AT REST SHOWS SIGNIFICANT CURVATURE 57
FIGURE 4.19: CURVATURE OF *ELECTRO_2* 58
FIGURE 4.21: REFLECTIVITY MEASUREMENT SETUP 59
FIGURE 4.22: SURFACE REFLECTIVITY OF MUMPS MATERIALS 60
FIGURE 5.1: MODELLED SYSTEM 62
FIGURE 5.2: FOCUS-TO-FOCUS CONFIGURATION 64
FIGURE 5.3: ODD VS. EVEN NUMBER OF LENS SYSTEM 65
FIGURE 5.4: CODE V SYSTEM MODEL. LENS3, THE REDIRECTION MODULE, THE MICROLENSES AND THE MICROMIRROR ARE DEPICTED. 67
FIGURE 5.5: BEAM WAIST AT OUTPUT SURFACE (SMF) 68
FIGURE 5.6: LATERAL AND ANGULAR DISPLACEMENTS FOR MICROMIRROR TILT FROM 0 TO 12 MRAD 69
FIGURE 5.7: ATTENUATION LOSS FOR MICROMIRROR TILT OF 0 TO 12 MRAD 70
FIGURE 5.8: ENERGY TRANSFER FOR 4 WAVELENGTHS AND FOR MICROMIRROR TILT FROM 0 TO 11 MRAD 72
FIGURE 5.9: EXPERIMENTAL SETUP 74
FIGURE 5.10: (A) BEAM AT DOE2'S POSITION (B) BEAM PROFILE AT THE MICROMIRROR'S POSITION 75
FIGURE 6.1: FEEDBACK SYSTEM 79

List of Tables

TABLE 1.1: TRAFFIC ON INTERNET BACKBONE [1] 1

TABLE 2.1: PERFORMANCE OF AOD ATTENUATORS (AT λ = 638.8 NM, HENE LASER) 15

TABLE 2.2: EQUALIZERS' COMPARISON 17

TABLE 3.1: OPTICAL CIRCULATOR TECHNOLOGIES 24

TABLE 3.2: FREE-SPACE GRATING DEMULTIPLEXER PERFORMANCE 27

TABLE 3.3: COMPACT AWG SPECIFICATIONS 28

TABLE 4.1: MUMPS LAYERS 39

TABLE 4.2: CAPACITOR PLATE MODEL SPECIFICATIONS AND RESULTS 47

TABLE 4.3: POLYSILICON MATERIAL MODEL 49

TABLE 5.1: LENS SPECIFICATIONS 63

TABLE 5.2: LENS SEPARATION DISTANCES 64

TABLE 5.3: COUPLING LOSS AT FIBER (OVER ALL WAVELENGTHS) 70

TABLE 5.4: LOSS INCURRED AT VARIOUS EQUALIZER COMPONENTS AT ZERO TILT 72

TABLE 5.5: MAXIMUM AND MINIMUM ENERGY TRANSFER 73

Acronyms

AOD:	Acousto-Optic Device
AWG:	Arrayed Waveguide Grating
BPR:	Beam Propagation
CCD:	Charge Coupled Device
CMOS:	Complementary Metal-Oxide Semiconductor
DMD:	Digital Micromirror Device or Deformable Micromirror Device
DOE:	Diffractive Optical Element
ECL:	External Cavity Laser
EDFA:	Erbium-Doped Fiber Amplifier
FEA:	Finite Element Analysis
FEM:	Finite Element Model
MEMS:	Micro-Electro-Mechanical System
MUMPS:	Multi-User MEMS Processes
NA:	Numerical Aperture (Fiber)
OPD:	Optical Path Difference
PDL:	Polarization-Dependent Loss
PLC:	Planar Lightwave Circuit
PSI:	Phase Shifting Interferometry
VCSEL:	Vertical Cavity Surface Emitting Laser
VOA:	Variable Optical Attenuator
VSI:	Vertical Scanning Interferometry

1 Introduction

"If you build it, they will come"

In the decade leading to the year 2001, big and small telecommunication companies, believing that the already astronomical Internet traffic growth rate would only increase, deployed an impressive network of fiber optics. Over the decades, bandwidth was continuously upgraded. New technologies, some still in their development stage, such as Erbium-doped fiber amplifiers (EDFA), were quickly brought to market and deployed in the field. Intellectual and monetary capitals were poured into research for newer and faster technologies that would meet the expected growth. Micro-electromechanical systems (MEMS), for example, receiving much attention matured into a reliable and feasible technology. This trend continued until late 2000. Their exuberance was then proven to be excessively optimistic.

The telecommunication companies believed that "*if you build it, they will come*" and that one can never have too much bandwidth. In retrospect it seems foolish; however, in the 1990s, these companies have many reasons to believe that they were right. Internet traffic grew at an astronomical rate, as shown in Table 1.1. New internet applications were continuously developed. *Dot-coms* were founded daily and a new cyber market was emerging.

Table 1.1: Traffic on Internet Backbone [1]

YEAR	TB†/MONTH
1990	1.0
1992	4.4
1994	16.3
1996	1,500
1998	5,000-8,000
2000	20,000-35,000
2002	80,000-140,000

†TB: Terabyte

Business Week wrote in 2000 that "*Internet traffic is doubling every three months.*" The future looked very bright. The problem was that there was never any real hard data to support this enthusiasm for the future growth. It did not materialize.

Today, the Internet traffic is still growing, although at a slower rate, doubling at approximately every year. The popularity of peer-to-peer applications and the arrival of promised voice-over-IP and video-on-demand will continue to fuel growth. Faster optical fiber-based communication systems will continue to be developed. However, researches are now focused on bridging the last gap in optical communication network and to bring fiber connections to the homes or end-users. The emphasis is on designing, developing and building a switching, routing network in which signals remain optical [2] [3], a so called agile all-optical or all-photonic network.

1.1 Motivation and Objective

The ability to control, adjust, and equalize the optical power of signals is important in current and future all-agile photonic networks. As optical network technologies, fiber and free-space, increasingly move from providing connectivity in the internet backbone toward the metro area network and the eventually to the end-users, higher levels of device performance and integration are necessary. These components must be able to accommodate and handle increasing number of signal channels that undergo more transmission, amplification, add-drop, multiplexing and switching operations. Silica fiber dispersion and loss are wavelength-dependent. The gain spectrums of EDFAs are non-flat with more than 10 dB difference between peaks over the C-band (Figure 1.1).

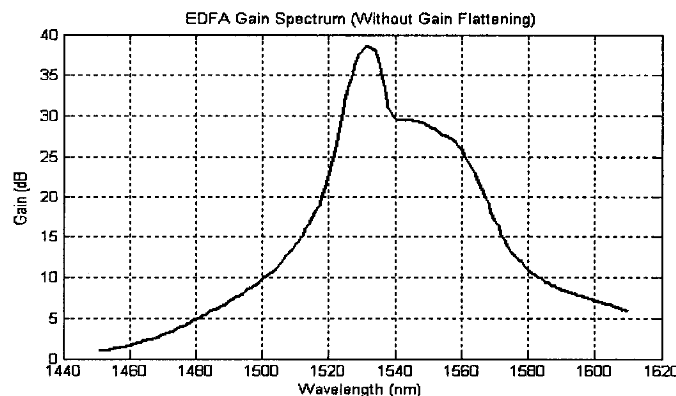

Figure 1.1: Typical EDFA Gain Spectrum

Optical power also varies as channels are dropped, added, separated and routed on to different paths. The insertion loss, crosstalk and performance of these devices are generally wavelength-dependent. Unstable laser sources and uneven spacing of amplifiers in the transmission line and over the network require compensation. The wavelength-dependent characteristics create a drift of the optical power between channels. Variable optical attenuators (VOAs) or power equalizers are needed to compensate for the power drift and maintain peak signal-to-noise ratio. Although the optimization of the various optical components can minimise the wavelength-dependent loss well below, say 1 dB, the cascade loss of the optical signal traversing all these components in on optical path will become significant.

The power equalization is not only required for the optical performance of the network, but also desired as it optimizes the design of many components, mainly the optical receivers. The requirements for such devices are alike other optical components in the network: high sensitivity, fast response, minimal noise, low cost, and high reliability.

The performance criterion normally used to evaluate a given design is the *bit-error rate* (BER). It is defined as the probability of the receiver circuit of incorrectly identifying a signal. Hence a BER of 1×10^{-9}, which is commonly accepted as the minimal performance level, corresponds to one error out one billion bits. The BER of the receiver depends on the design of the decision circuitry and photoelectric effect of the chosen semi-conductor. This rate is also, importantly, dependent on the quality of the incoming optical signal. Shown in Figure 1.2 is a typical BER plotted against a Q parameter. The Q or quality parameter characterizes the incoming signal and is a strong function of the incoming signal power (both the high and low state) and noise level. At higher power level, an overload effect occurs, where the BER increases with increasing power. The efficiency also degrades with decreasing signal power. Therefore, there is an optimal input power level that would ensure an optimal performance for the optical receiver for a given design.

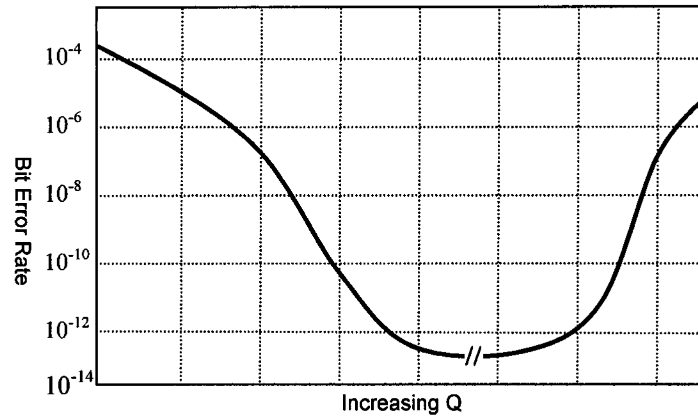

Figure 1.2: Bit-Error Rate versus the Q Parameter for Typical Optical Receivers [4]

In a DWDM network, it is thus important and desired for the signal level in all the channels are equalized to the optimized power level. In turn, this would facilitate the design of the receivers as a given uniform incident power can be assumed.

What is thus required and desired is an equalizer module that will provide the following:

a. **Large dynamic power range attenuation**

To compensate for the variable loss incurred by an optical signal through cascaded operations: amplifications, (de)multiplexing, etc, one would require an equalizer module with large maximum attenuation. A large range allows for flexibility in the network design and avoids the need to cascade multiple equalizer modules in a given lossy transmission link. Existent and proposed attenuator designs offer maximum attenuation ranging from 15 dB to 60 dB. A dynamic attenuation in the upper limit to this range, 50-60 dB is sought for our proposed equalizer module.

b. **High sensitivity/high resolution**

While a large dynamic range is desirable, a constant and high attenuation sensitivity or resolution over the entire dynamic range is also important. A resolution of 0.1 dB is sought.

c. **Scalable channel count**

64 wavelength channels are assumed for the design of the equalizer module. The channels are spaced at 100 GHz on the ITU grid covering the C-band. However, it is highly desired to design a (de)multiplexing operation of the equalizer such that

the channel count is scalable to 128, 256 and higher numbers. Large channel counts are required for broadband optical network.

d. Low insertion loss and low polarization loss

The equalizer module should have a low impact on the power budget of the optical power link. The system's minimal insertion loss, defined as the minimum attenuation level across all wavelengths, should be maintained at less than 1.0 dB. Wavelength and polarization-dependent losses should be minimised as to maintain similar performance across all wavelengths and polarizations.

e. Fast response and attenuation stability

Dynamic equalization requires that the optical power of a signal is adjusted to its desirable level quickly and is maintained at that level over the desired interval of time. For our design, a response time of 20-100 μs and attenuation stability under 0.1 dB are sought.

f. Off-state power stability

In a given network protocol/or specifications, one would desire that the level of attenuation is set and held even after the removal of electrical power. Although the addition of the off-state power stability requires added complexity to the attenuation mechanism, it can lower the device power consumption and increase its robustness.

g. Thermal stability

Although the chosen mechanism to produce the optical power attenuation can be thermal-based (e.g. thermo-optic effects), the performance of the package module should be independent of the ambient temperature.

h. Robust, cost-efficient and packageable design

As in other designs, the equalizer design should be both simple and robust. The device should deliver the required performance with the minimal number of components, offering thus reliability and cost-efficiency. The design of the components should be easily assembled into a compact and reliable package.

The equalizer module would perform the following operations, schematically shown in Figure 1.3. From the transmission fiber, the optical signal must first be (de)multiplexed,

or separated in individual wavelength channel, either spatially in free-space or into individual fibers or waveguides. The power levels of each wavelength are then adjusted to the desired level and then recombined (multiplexed). It is then coupled into the outgoing fiber. The three separate operations form a complete equalization operation. Each sub-module can be implemented via a multitude of technologies (from fiber-based to free-space optics).

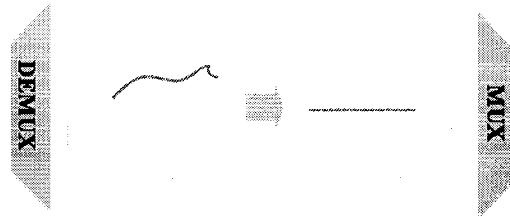

Figure 1.3: Equalizer – Block Diagram

The objective of this thesis is to present an equalizer module design that will meet the above requirements. A secondary objective is to show that a MEMS-based equalizer is an attractive solution and would offer an excellent performance.

1.2 Thesis Outline

The design method of the equalizer module, as presented in this thesis, is four-fold with each stage conveniently separated into a chapter. The first step consists of survey of existent VOA designs (Chapter 2). Design lessons and pointers are drawn from other researchers. More importantly, the review will offer a point of comparison for our equalizer module. Stemming from this study, specifications for the optimal attenuator design can be determined and major components of the equalizer are identified. This is done in chapter 3. Our design utilized MEMS micromirrors. As it will be shown, their performance is critical in the overall design of the equalizer. As such, chapter 4 is dedicated to a discussion of our MEMS micromirror designs and characterisations. The final step consists of evaluating the performance of the equalizer, both theoretically and experimentally (chapter 5). Chapter 6 summarizes future improvements and the main conclusions from this work.

1.3 Brief System Description

The concept of the compact optical power equalizer presented in this thesis stems from the design work done by Frédéric Thomas-Dupuis for his Master's degree in 2002 [5]. In the research project, F. Thomas-Dupuis et al. designed and implemented a novel two-dimensional formatting module for dense wavelength division multiplexing using multilevel multifacet diffractive optical gratings. The module was designed to spatially demultiplex 64 wavelength optical signals outputted from a single mode fiber to a 4 x 16 array format. This operation is reversible, i.e. 64 signals can be combined or multiplexed together, and coupled into the fiber. The implementation of the (de)multiplexing is additionally scalable to 128, 256 and higher channel counts, without significant impact on the size of the module. It was quickly realized that an attenuator can be easily implemented from (de)multiplexing module by integrating a MEMS micromirror array.

The principle of operation of the equalizer module is straight-forward: it is well illustrated by the following figure.

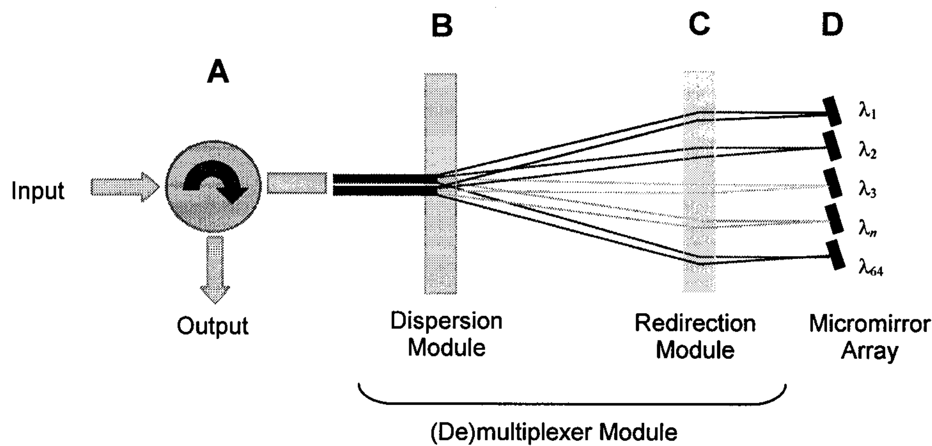

Figure 1.4: Operation Principles of the Equalizer

Optical signal from a fiber is first spatially dispersed (demultiplexed) at point B. The individual channels or wavelengths are redirected by module C on to the micromirrors at position D and reflected. Because of the small tilt of the micromirrors, the light beams return back in to the system on a slightly different path. As the signals traverse module C, B and then back to the fiber, the beam positions are laterally translated, which in turn affect how well light from each channel is coupled into the fiber. The tilt of the

micromirrors are independently controlled for the variable optical power attenuation of each channel.

The basic concept of the proposed equaliser is not novel. The use of micromirrors for attenuation has been proposed and implemented by many research groups, as shown in the following review of existent attenuator technologies. However, none of the alternatives proposed a solution that handles 64 wavelengths simultaneously in a compact and integrated package; this is the chief justification for undertaking of the present project. The novel approach here consists of spatially formatting the (de)multiplexed signals into two-dimensional arrays.

2 Literature Review

2.1 Survey of Optical Equalizer Research

The importance of variable optical power equalizers in modern optical networks has advanced the development of numerous and novel solutions. While some are still in the research and development stages, other are already commercialized. The current chapter will survey these various solutions and will examine their unique advantages and shortfalls.

The proposed devices are as varied as they are numbered. However, they can be classified in three broad categories based on their underline technology. These three groups are: waveguide-based, amplifier-based and MEM-based equalizers. Examples of each type of equalizers are presented in the following sections.

2.1.1 Waveguide-based and Thermo-optic-based Equalizers

The first group of equalizers, waveguide- and thermo-optic-based variable optical attenuators (VOA), work on the principal of controlling the propagation of the optical wave in a waveguide. Attenuation is obtained by decoupling light into and out to a waveguide. The amount of attenuation is controlled by adjusting the phase or the modal composition of the optical wave.

Polymeric Waveguide and Thermo-optic Effect [6]

One device developed by T.C. Kowalczyk et al. (*Gemfire Corporation*) consists of a resistive heater element that is fabricated on the top of the cladding layer polymer channel linear waveguide. The dimensions and parameters of the waveguides are chosen to minimise the insertion loss by mode matching the guided wave with the input and output to a single mode fiber (SMF28). The slab waveguide is built above a thick substrate. When the resistor heater is activated, a thermal gradient is established in the polymer slab. Because of the thermo-optic effect, a large refractive index gradient is also created through the polymer waveguide slack. As an optical wave propagates through the modified section of the waveguide, it undergoes modal evolution and is deflected into the

substrate. The amount of deflection is controlled by the thermal gradient and thus by the power of the resistive heater.

S. M. Garner and S. Caracci propose a device similar to the polymeric linear waveguide VOA where the waveguide is curved [7]. The index gradient established by the thermo-optic effect mode distorts the propagating made asymmetrically downward in the waveguide. However, the bend also distorts the mode horizontally. This further reduces the mode confinement in the waveguide and causes higher radiation losses. The degree of the bend of the waveguide can be used to tune or scale the dynamic range of the VOA. They were able demonstrated an attenuation of greater than 40 dB at 1550 nm.

The third example of waveguide-based attenuator is one presented by S.-S Lee et al. [8]. Here, the equalizer design is composed of an asymmetric Y-branch waveguide (Figure 2.1), where one of the arms serves as the main output port, while the second smaller arm guides the residual optical power from attenuation. One advantage of such a configuration is that there is no generation of undesirable radiation modes. To control the amount of power coupled into either arms, the thermo-optic effect is also employed. The thermal and index gradient is established laterally across the Y-branch waveguide, such that the modes are distorted asymmetrically between the two branches. Typically, with waveguide core of 5.5 x 1.5 μm^2 and $\Delta n = 0.05$, at a wavelength of 1550 nm, they reported a dynamic range of 20 dB with a heater power of approximately 200 mW. Response time for attenuation from 0 to 10 dB is predicted to be at around 1 ms due to the slow thermal response.

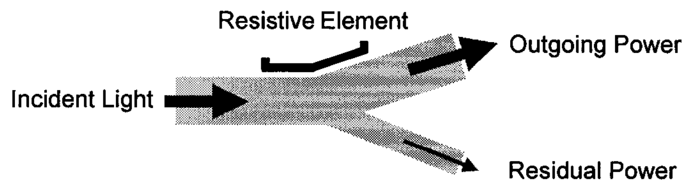

Figure 2.1: Y-branch Waveguide Attenuator [8]

With these devices, polarization and input power dependent losses are important. Typically, polarization dependent loss (PDL) is measured at 1.0 to 2.0 dB with total

insertion loss of 3 dB. Waveguide designs can be optimized to minimise the polarization effects. Performance can be further improved by introducing a continuous electronic feedback control. It requires the addition of Y-branch to the main output port. The additional branch is used as a monitoring tap for dynamic control of the power equalization. Note that these equalizers are for single channel/wavelength attenuation, while the following device is a multi-channel equalizer.

Mach-Zehnder Couplers and Phase Shifters [9]

The final example of a waveguide-based variable attenuator design consists of utilizing Mach-Zehnder couplers. Two waveguide couplers are connected together with programmable phase shifters (PPS) placed in between on one of the arms. A PPS is a device whose effective path length can be controlled externally.

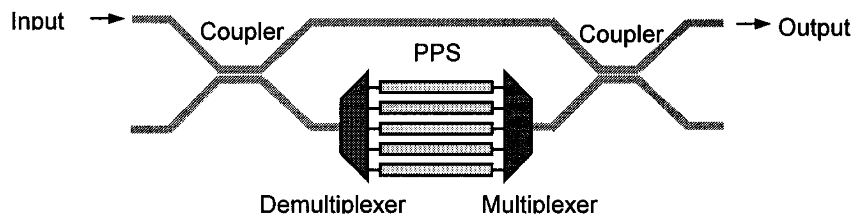

Figure 2.2: Mach-Zehnder-based Equalizer

As the light propagates and encounters the coupler, the optical power is divided into the two arms. While light propagates normally in the first arm, it is wavelength-demultiplexed in the second arm. The phase of each wavelength signal is then externally adjusted via the PPS and recombined by the multiplexer. Light from both arms are then recoupled. The coupling efficiency is controlled by the amount of phase added in each wavelength resulting in adjusted power levels at the output port. The various components, from the multiplexers, to the couplers can be etched Indium-Phosphate (InP), polymer or silica. N.S. Lagali et al. [10] implemented using such a VOA for 8-wavelength channels. The reported attenuation range is above 30 dB with 1.8 dB insertion loss. Polarization-independent and insertion losses remain a significant problem. A 7 to 8 ms response time is obtained. The device is highly integrated with the PPS and couplers built on the same wafer.

2.1.2 Amplifier-based Equalizers

In the second broad category of equalizers, power equalization is done through the use of optical amplifiers. As opposed the devices described previously, which attenuate the optical signals to a desirable level, amplifier-based equalizers inject optical power into the signal to attain and maintain a power level.

M. Zirngibl et al. constructed such a device [11] using arrayed-waveguides gratings (AWG) and semiconductor optical amplifiers. The basic configuration of the device is as follows:

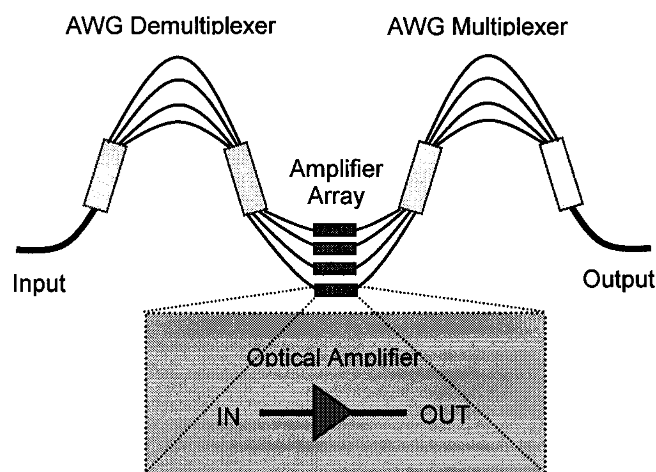

Figure 2.3: EDFA - AWG Equalizer

The input signals are demultiplexed by a first AWG into separate fibers. The signals are then amplified by the optical amplifiers, which can be configured to maintain a constant output level. A second AWG is used to recombine the wavelengths. The operation of the AWG is quite simple and will be discussed in greater details in section 3.3.2. The design and operation of the amplifiers is beyond the scope of this thesis, but interested readers are refer to [11] for more details. Alternatively, Er-Doped Fibre Amplifiers (EDFAs) can be used instead of the semiconductor optical amplifiers [12]. In their implementation, a 7-channel equalizer requires a total area of 6 x 18 mm^2. Good signal isolation of -19 dB and gain of 19 dB was measured. However, the device, as in other active components, would be susceptible to noise from the spontaneous emission power. However, this implementation does not scale particularly well to higher channel count. Since an

amplifier and a pump source are required for each wavelength, the equalizer's complexity and cost would increase significantly with additional channel count.

2.1.3 MEMS-based Equalizers

MEMS approaches for creating equalizers or VOAs have been focused on two simple techniques: a blocking vane or sliding-block mechanism [13] [14] or micromirror reflector method [16].

The first technique for creating attenuation consists of simply inserting an obstruction in the optical path (Figure 2.4 (a)). By partially inserting the vane or shutter into the light beam, part of the light is scattered and thus is not transmitted to the outgoing fiber or waveguide. The amount of attenuation is determined by the surface covered by the vane or shutter. The designs of the blocking mechanism are quite varied. Although the principle of the attenuator is simple, its realisation has only been recently possible with the development of MEMS, which offer both the micro-scale dimension and precision necessary. The MEMS devices are as simple as a capacitor plate that is levered through a pivot to elevate a vane [14] or as complex as a comb drive actuator pushing a blocking bar [13]. The packaging of the block mechanisms with the fiber or waveguide can also be facilitated with MEMS. The alignment of the ingoing and outgoing fibers can be done by placing V-grooves leading into and out of the block vane. In other designs, an expanded waveguide is sometimes inserted between the fibers and the vane. This is done to maintain single mode operation, to increase to attenuation accuracy and to lower the polarization-dependent loss [13]. The waveguide can be fabricated on the same wafer or chip as the block mechanism. In one design patented by Lucent Technology [15], the attenuator exhibits less than 1 dB insertion loss at 1550 nm and a greater than 50 dB dynamic range with output power variation within 0.26 dB. The device handles a single wavelength at the time. A feedback control circuit allows for a tight regulation of the output power. An impressive response time of 100 μs and a 0.5 dB polarization-dependent loss were measured.

The second approach to variable attenuation via MEMS is based on the principle of controlling the coupling of light between two fibers [16]. The deflection of a micromirror creates misalignments losses by steering the beam from the core of the outgoing fiber, as shown in Figure 2.4 (b).

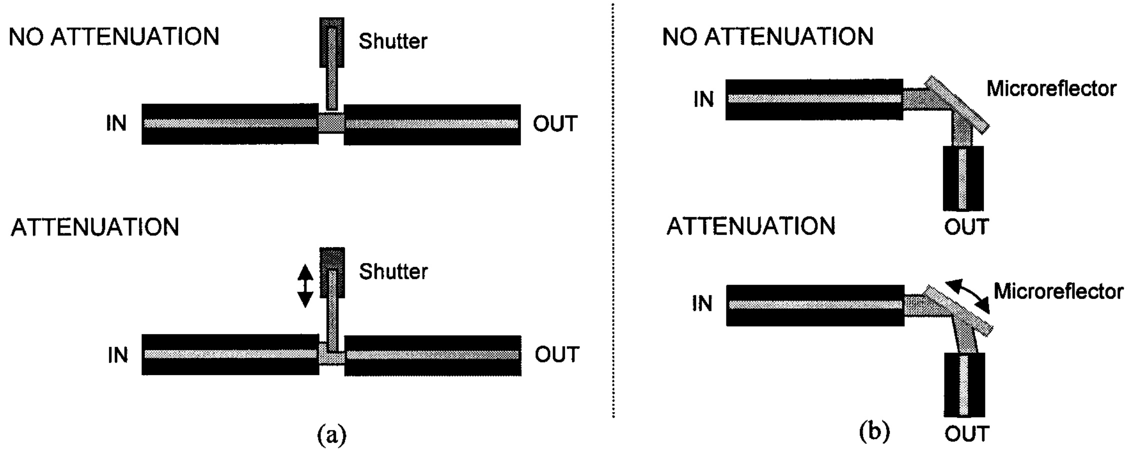

Figure 2.4: MEMS-based Attenuator Configurations
(a) Blocking Vane Mechanism
(b) Reflector Mechanism

High resolution can be obtained (0.2 dB). Repeatability and stability are often the main issues with this approach; however, proper design of the microreflectors/mirrors can alleviate these problems. The equalizer design presented in this thesis falls within this category of devices. The main issues of this approach include the micromirror designs, alignment tolerances, deflection control and reliability. In the many designs reported in literature, a discussion of the device integration and channel count is not included. (De)multiplexing operations are also required and add complexity to the overall equalizer design.

2.1.4 Another Equalizer: *Using* Acousto-optics

Other interesting equalizer designs exist. N.A. Riza et al. suggest a novel approach to variable optical attenuation exploiting an in-line one-to-one imaging optical architecture operating with two acousto-optic Bragg cells [19]. The key advantage of this technique is its sub-microsecond response time, at approximately 175 ns.

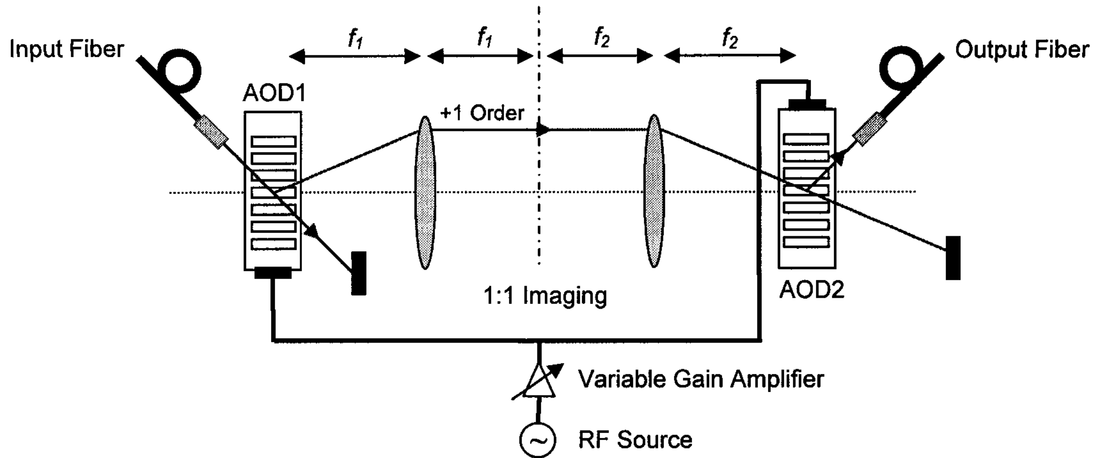

Figure 2.5: Acousto-optic-based Equalizer

The attenuator configuration is as shown in Figure 2.5. A 1:1 optical imaging system, consisting of two spherical lenses, is placed in between two acousto-optic Bragg cells acting as beam reflectors. The acousto-optic devices (AODs) exhibit a phase grating when a radio-frequency signal is fed into them, such that an incident beam is diffracted at its surface. The index of modulation Δn of the grating is directly proportional to the amplitude of the input RF signal, while the grating period is a function of the frequency of the RF signal. As the RF signal frequency and amplitude are varied, a dephasing effect is introduced that will alter the diffraction efficiency of the Bragg cell grating. This is the mechanism by which optical power is attenuated. The two AODs are arranged in reversed orientation to provide a cancellation of the Doppler shift introduced by the AODs. Experimental measurement of the AOD-based attenuator, operating in variable RF signal amplitude and frequency are as follows.

Table 2.1: Performance of AOD Attenuators (at λ = 638.8 nm, HeNe Laser)

	AMPLITUDE MOD.	FREQUENCY MOD.
Dynamic Range	38.3 dB	45.49 dB
Resolution	0.79 dB/V	0.22 dB/MHz
Insertion Loss (Excess Loss)	4.06 dB	3.55 dB

2.1.5 Evaluation of Designs

The operational and performance characteristics of the reviewed equalizers or attenuations are quite varied. As their underlying technologies are different, the equalizer

designs offer in some cases better attenuation range while in others, faster responses or superior reliability. A comparative performance evaluation, in terms of attenuation, power resolution, insertion and polarization loss, and response time of the various designs are summarized in Table 2.2.

Table 2.2: Equalizers' Comparison

	DYNAMIC RANGE	RESOLUTION (VARIABLE FROM CHANNEL TO CH.)	PDL †	INSERTION LOSS	RESPONSE TIME
Single Channel Device ††					
Thermo-optic Effect on Polymeric Waveguide [6] [7]	30 dB 40 dB	N/A	N/A.	< 1.0 dB	< 2.0 ms
Thermo-optic Effect on Y-branch Waveguide [8]	20 dB	1.2 dB	0.9 dB	3.0 dB	100 ms, but can be enhanced up to 1 ms
MEMS: Blocking Vane [13]	25 dB	N/A	0.05 dB	0.5 dB	N/A
MEMS: Blocking Vane [14]	30 dB	0.2-0.5-dB	0.5 dB	1.0 dB	< 100 μm
MEMS: Micromirror Reflector [16]	18 dB (Greater than 50 dB in other designs)	0.1 dB	0.06 dB	1.0 dB	N/A
Acousto-optic Attenuator [20]	38 dB	2.7 dB	1.6 dB	3.5 dB	0.175 μm
Multi-Channel Device (including (de)multiplexing operation)					
MZI and AWG Attenuator [10]	30 dB	1.0 dB	0.1 dB	1.4 -1.8 dB	7-8 ms
EDFA and AWG Attenuator [11]	19 dB	N/A	N/A	15 dB	N/A

† *Polarization-Dependent Loss*

†† *For signal channel device, insertion loss of the (de)multiplexing device should be added for fair comparison. Typically, they range from 0.7 to 2.0 dB. Section 3.3.3 discusses various (de)multiplexing devices including AWGs.*

Generally, thermo-optic waveguide attenuators have a low insertion loss with mid-range (30-40 dB) attenuation. The thermo-optic coefficient of waveguide material, mainly silica, is small and thus limits the mode confinement loss. The attenuation is also generally slow with reported response times in the millisecond range. Equalizers that incorporate amplifiers or EDFAs offer good attenuation resolution, but generally they have a limited dynamic range. The integration of the pump lasers and their associated control circuits becomes difficult as the channel count rises. The acousto-optic device offers fast response and large attenuation; however, like the amplifier-based designs, the numerous components (AODs, spherical lenses, RF generators) impede the integration in high channel count systems.

The integration problem remains the key obstacle to the development of many equalizer/attenuation designs. Large arrays of AODs, EDFAs, thermal resistive heaters and PPS are not easily realizable. Here is where MEMS-based equalizers have the advantage. Large arrays of MEMS device can be designed and fabricated; power adjustments for 64, 256 and higher channel count is possible. With the advent of integrated CMOS and MEMS fabrication processes, compact designs can be also realized. MEMS-based equalizers offers good dynamic ranges; however the mechanical parts do limit the speed of the response time in the tens to hundreds of microsecond range at best.

The approach presented in this thesis for power equalization exemplifies the advantage of MEMS-based designs for handle multiple channels. Combined with an efficiency and compact (de)multiplexing approach that allows for the 2-dimensional treatment of the wavelengths, an equalizer design that meets all the requirements laid out in the opening chapter can be realized with MEMS micromirrors.

At this point, a brief survey of MEMS micromirror research is warranted. These devices are an essential component to the equalizer design discussed in chapter 3. This review is presented in the next section; it demonstrates that MEMS micromirrors have significantly evolved since its debut, and today, can be reliable devices.

2.2 Survey of MEMS Micromirror Research

In December 1959, Richard P. Feynman, in a classic talk to the American Physical Society entitled "*There's Plenty of Room at the Bottom*", posed the following question: "*Why cannot we write the entire 24 volumes of the Encyclopedia Brittania on the head of a pin?*" What he was talking about is the incredible technological possibilities once we are able to fabricate, manipulate and control things on a small scale. The talk challenges researchers and scientists to think about and to explore these possibilities. However the trend toward miniaturization had started earlier with the invention of the silicon-based transistor in 1947 by W. Brittain and J. Bardeen, and continued with the first integrated circuits (ICs) in 1958 by Texas Instruments. Today, fabrication techniques have advanced such that soon device sizes will only be limited by quantum effects. Paralleling the development of integrated circuits, the fabrication of micro-electromechanical system also matured into a viable industry. As early as the invention of the transistor and ICs, researchers adapted the fabrication techniques to micromachine simple mechanical devices, such as pressure sensors and thin membranes. Silicon was shown to have good mechanical properties. Over the decades, more refined techniques, again borrowed from the IC industry, were introduced. Bulk micromachining, surface-micromachining, LIGA (*acronym for the German words: lithography, electroforming, and moulding)* and many more [21] were one by one introduced. In late 1980s, the acronym *MEMS* was coined to designate this growing field of micro-electro-mechanical systems.

2.2.1 A Brief history of MEMS Micromirrors

A variety of micro-mechanical systems or devices have been developed over the past four decades, some with more success than others. Accelerometers and pressure sensors were among the first devices proposed and today, they enjoy a great commercial success in the automotive industry. Micro-fluid nuzzles have also much success in printing and biomedical applications. Deformable or tiltable micromirrors have received much attention, with applications in field ranging from telecommunication to imaging. Micromirrors, also called spatial light modulators and deformable membranes, have been popular since the early days; in fact, one of the first MEMS devices were simple membranes.

One of the earliest devices, a deformable mirror device (DMD), was publicized by L. J. Hornbeck in 1983 in [22]. The design consists of a membrane of thin metallized polymer or silicon that is stretched over a supporting grid of anchor structures, as shown below.

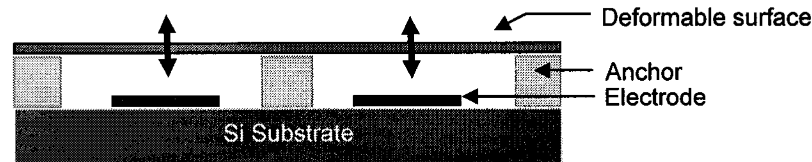

Figure 2.6: Deformable Membrane

The anchor structures suspend the membrane over address electrodes with an air gap in between. As a voltage is applied (approx. 50V) to the electrodes, an electrostatic force field causes the membrane to deform into the air gap. Large and dense arrays of DMD can be fabricated, and can be adapted for the equalizer application. In essence, a DMD is a curved mirror for which the radius of curvature or focusing power is controllable. However, the range of deformation is limited, and thus would only provide a small attenuation in the equalizer design (section 5.1).

An alternative micromirror design was proposed in 1975 by R.N. Thomas et al. [23], the cantilever mirror. In this design, mirror membrane or surface is raised above electrodes by a central micro-post or anchor, as shown in Figure 2.7. As an electric field is applied, the surface is deflected or tilted while remaining planar for efficient light steering.

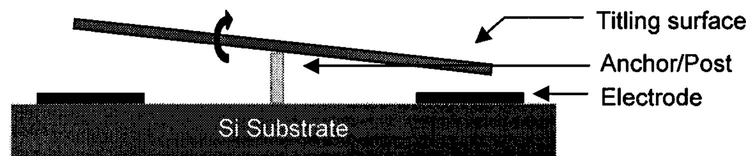

Figure 2.7: Cantilever Mirror

In their demonstration, a density of 500 elements per inch has been fabricated with a silicon-dioxide membrane measuring 46 x 46 μm. The cantilever design allows for larger surface tilt-angle that necessarily requires larger applied electrode voltages, in some cases above 100 V.

Many variations of this design were proposed later, among others by K. E. Petersen at IBM [24]. Instead of a central post that raises the micromirror surface above the substrate, torsion bars or hinges can be used to suspend the surface. The micromirror rotates about the axis set by the hinges. The torsion bars are replaced in some cases by spring hinges, or in other designs, by flexure beams. Two of the micromirror designs presented in this thesis fall within this category. They are more suitable for the equalizer module: the planar surface minimises aberrations; while the large tilt guarantee better attenuation range.

Today, micromirror designs are well varied with both simple and more complex designs. Multiple fabrication techniques are used often in combination to fabricate the micromirrors. In 1996, Texas Instruments (TI) Inc. introduced its digital micromirror devices (DMD) [25]. It has become one of the most successful, commercially and technically, MEMS devices. What TI was able to shown with its DMD and projection displays is that, from the simple cantilever design presented in 1975, today's micromirrors can offer the reliability, range of operations and quality yield required for field deployments. Challenges remain to design micromirrors with reduced surface stress, increased repeatability, and increased yield. Integration with existent CMOS technologies is also highly sought.

3 Micro-optics and Micromirror-based Equalizer

3.1 Overview

The advent of reliable and high performance MEMS micromirrors has made possible the realization of devices and integrated systems in which micromirrors can be exploited to provide superior performance to their current counterparts. MEMS-based variable attenuators and equalizers have been demonstrated with large attenuation range (section 2.1.3). These designs are highly attractive; however, research has hitherto not presented a means to expand the technique to multiple channel systems in a simple and elegant fashion. By this, we mean an equalizer or attenuation module in which the integration of the various wavelengths is done with a minimal number of components and compactly. The design also allows for large misalignment tolerances to ease assembly.

In chapter 1, we described the design and operational principals of the compact equalizer module. In this chapter, we restate the requirements for the equalizer module and detail the choices and functions of each component. More specifically, this chapter presents a discussion of how each component will affect the overall system performance and how they are designed to meet the desired system specifications.

3.2 System Requirements

In section 1.1, we outlined the desired specifications for the equalizer module. The following criteria were established:

- Dynamic power equalization
- High resolution (0.1 dB)
- 64 wavelengths with 100 GHz spacing on the ITU grid covering the C-band
- Scalable from 64 to 128, and 256 channels
- 0-50 dB attenuation range
- Low minimum insertion loss (1.0 dB or better)
- Low polarization-dependent loss
- Fast response and high sensitivity

- Off-power state stability
- Thermal stability
- Robust, cost efficient, and packageable design

In meeting these specifications, the various components of the system must be individually optimized. While the effective insertion loss of the equalizer system is the cumulative loss of all the components, other criteria are predominantly determined by the performance of key components. Attenuation range and equalization stability and sensitivity are mainly dictated by the tilt range of the polysilicon micromirrors. The polarization-dependent loss, scalability, channel spacing and channel count are primarily limited by the design of the (de)multiplexing system.

3.3 System Components

The principal concept of the equalizer module is based on the principle of controlled beam-to-fiber alignment or coupling efficiency using MEMS micromirrors as the active elements. This equalization can be done simultaneously for 64 wavelengths with the addition of a micro-optic-based (de)multiplexer module. Although, the micro-optics and micromirrors are the primary components, two other functions are also needed, mainly, an optical circulator and microlens telescope. The former device is required to collect the output optical signal; while the latter is needed to optimize the attenuation control curve. As such, the designed system has the following components:

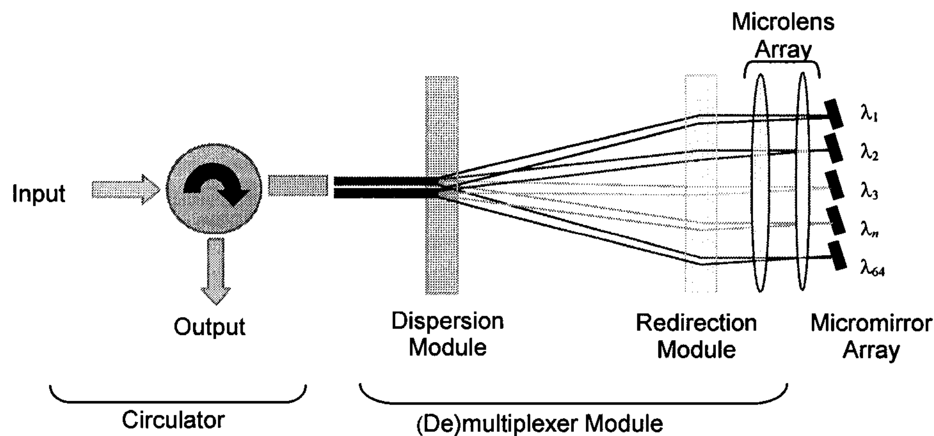

Figure 3.1: Equalizer Module's Components

a. optical circulator
b. dispersion module
c. redirection module
d. microlens telescope
e. polysilicon micromirror array

The following sections detail the design and performance of these components. These discussions are based on existent approaches for these operations.

3.3.1 Optical Circulator

The forward (input) and backward (output) propagating optical waves or signals of the equalizer module traverse the same fiber and must be separated via an optical circulator. The outgoing signal must be coupled out to a secondary port, as shown schematically in the figure below:

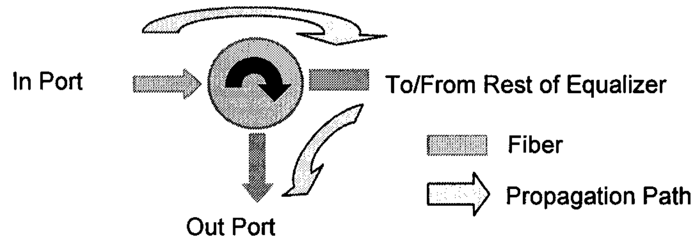

Figure 3.2: Optical Circulator

There exists a number of ways to implement this function. Table 3.1 lists three different circulator designs: some use faraday rotators while others, MEMS blazed gratings. Two features sought in a good circulator are a polarization insensitivity and high channel isolation.

Table 3.1: Optical Circulator Technologies

TYPE / COMPONENTS	DIMENSION W x L x T	ISOLATION	INSERTION LOSS	REFERENCES
non-reciprocal Mach-Zehnder Interf., Faraday rotators, and thin-film half-waveplates.	4 x 47 x 3 mm^3	14.0-23.7 dB at λ=1.55 μm	3.0-3.3 dB at λ=1.55 μm	NTT Opto-electronics Laboratories. [26]
Birefringent crystal, Optically active rotators, Faraday rotators	5 x 57 x 5 mm^3	Over 60 dB at λ=1.55 μm	1.5 ± 0.2 dB at λ=1.55 μm	NTT Transmission Systems Laboratories [27] [30]
MEMS-based blazed diffractive gratings, shifting light (bending effect) in waveguide	Before Packaging 47 x 12 x 195 μm^3	12 dB (Theo. 18.5) at λ=1.55 μm	6 dB (Theo. 3.6) at λ=1.55 μm	U. of Tokyo [29]

Polarization independence can be designed into the circulator devices [26], [27]. Channel isolation varies significantly from designs to designs, and ranges anywhere from 14 dB to over 60 dB. Today, commercially available fibre optical circulators are highly efficient with loss that is less than 1.0 dB and PDL, less than 0.05 dB [28].

The optical circulator device is in itself separated from the rest of equalizer module, interconnected with a SMF fiber and packaged separately. Their overall dimensions are small. However, the need for a circulator can be designed out of the equalizer system. The proposed system is in essence a folded optical path, where the returning optical beam is only slightly displaced from the originating fiber source to cause a coupling loss. However, the system could also be unfolded as shown in Figure 3.3. In such a configuration, the need of an optical-circulator, along with its corresponding efficiency loss are eliminated. However, the setup would require a second dispersion module, redirection module and microlenses. The increased component number would result in increased assembly cost and time, higher misalignment losses and overall decrease of the system's reliability.

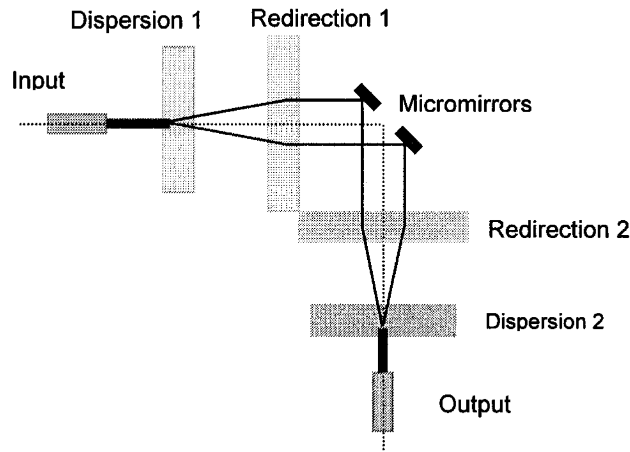

Figure 3.3: Unfolded Equalizer System

3.3.2 Dispersion Module

The dispersion module takes the optical from the fibre and separates the individual wavelengths. The wavelengths are formatted into a linear array with elements pitched at 62.5 μm, matching the input array of the redirection module. This demultiplexing

operation can be done simply with free-space grating technologies [5]. However, a more favoured method consists of using arrayed-waveguide gratings. These devices are well developed and commercially available. They offer many advantages over their free-space counterparts. They are generally more compact and easier to integrate into larger systems. The following paragraphs describe the operating principles of these two technologies.

Free-Space Grating Dispersion Module

A simple and low cost approach to performing spatial (de)multiplexing is to use a blazed grating, with lenses for formatting the input and output beam to the desired beam size and spatial separation (Figure 3.4). With an ideal blazed grating, a grating period can be chosen to obtain the required refraction angle for the different wavelength. However, since the grating equation is non-linear, the angular separation will be different for the different wavelengths, resulting in lower efficiency.

$$a(\sin\theta_m - \sin\theta_i) = m\lambda \qquad \text{Eq. 3.1}$$

θ_m: Refraction angle of mth degree
θ_i: Incident angle
a: Grating period

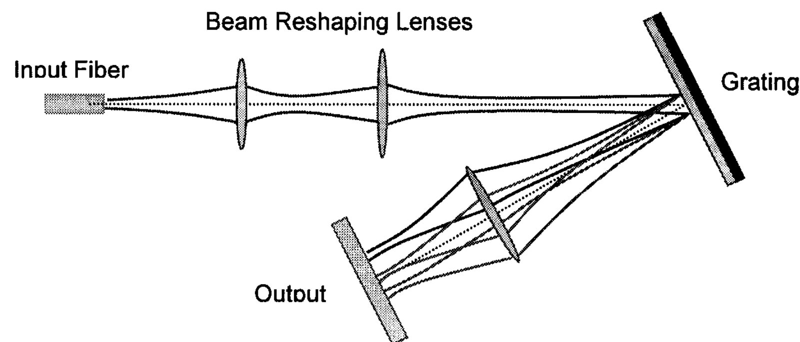

Figure 3.4: Free-Space Dispersion Module

Furthermore, the efficiency of the grating (first order) is limited to the number of steps used in the lithographical fabrication the grating periodical wedge, unless more expensive ruled gratings are used. This efficiency ranges from 50-80 %, depending on the vendors.

Coating the grating with a highly reflective material, such as gold, would raise the efficiency.

To convert the angular separation, $\Delta\theta$, into a lateral separation at the output, a simple spherical lens is required. Simply, the lateral separation, p, is given by

$$p = f\tan(\Delta\theta) \quad \text{Eq. 3.2}$$

where, f is the focal length of the lens.

In a device implemented for F. Thomas-Dupuis [5], the following performance was obtained at 1550 nm. The reader is referred to chapter 5 of [5] for design details.

Table 3.2: Free-Space Grating Demultiplexer Performance

OUTPUT WAIST	LOSS (dB)
21.2 ± 0.5 μm	1.93

Arrayed-Waveguide Gratings (AWG)

First proposed by Smit in 1988 [31] the U.S, and later by other in Japan [31], arrayed-waveguides gratings are increasingly popular devices as they have been proven to be capable of precise (de)multiplexing of large number of channels with a low insertion loss. Furthermore, recent developments in high index-contract planar lightwave circuits (PLC) have allowed significant reduction of the device's footprint, making them highly practical [33] and particularly well suited for the equalizer design.

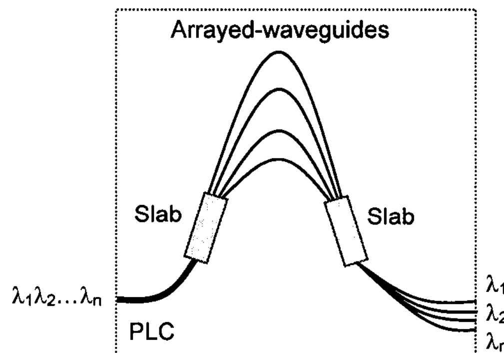

Figure 3.5: AWG on a PLC

An arrayed-waveguide grating (AWG), also know as an optical phased-array, consists of two focusing slab waveguides, or star couplers, connected by an arrayed-waveguide. The input light is initially coupled into the arrayed-waveguide by the first star coupler (Figure 3.5). The waveguides are designed such that the optical path difference between neighbouring wavelengths/waveguides is an integer multiple of the central wavelength of the AWG multiplexer. As the light propagates through the waveguides, and reaches the second star coupler, the central wavelength beam is focused at the center of the image plane, while adjacent wavelengths' focal point will be shifted away from the center on the image plane. The location of the focal point is both a function of the wavelength and phase delay of the light beam in each branch. As the light is coupled into individual waveguides or ports, one obtains a spatial separation of the different wavelengths.

Recent AWGs have the star couplers and the arrayed-waveguide that are integrated on to a single planar lightwave circuits (PLC). The waveguides are fabricated on a silicon substrate by a combination of flame hydrolysis deposition and reactive ion etching. Reference [33] has a detailed description of the fabrication process. Recent developments in PLC material and construct have made possible the high-density integration of the AWG, creating devices that are 1/5 the size of conventional AWGs.

In one particular design by Y. Hibino at NTT Photonic Laboratories [33], a highly compact AWG was demonstrated. They fabricated a 100 GHz-spacing, centered at a wavelength of 1.552 μm, 16-channel AWG on a PLC using waveguides with a 4.5 x 4.5 μm^2 core. Table 3.3 shows the overall AWG performance.

Table 3.3: Compact AWG Specifications

PARAMETERS	
Wavelengths	1.552 μm, spacing of 100 GHz
Insertion Loss Input fibre to output fibre	0.7-2.2 dB
Crosstalk	under -20 dB
Package Dimensions	84 x 32 x 11 mm^3

Both the crosstalk level and overall dimensions are particular interesting for our application; however the key issue remain the integration of the AWG into the equalizer.

At the input end, since the numerical aperture of the fiber and of the AWG input waveguide are mismatched, considerable loss will be incurred if there is no compensation. In their experiment, Y. Hibino used an intermediate fan-out PLC (Figure 3.6) where the AWG waveguide core size is gradually increased to match the size and shape of the fiber. This allows for better beam mode match. Coupling loss from the AWG with a core size of 4 x 4 μm^2 to a standard SMF fiber is measured at 0.3 dB.

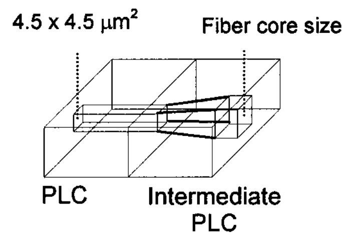

Figure 3.6: Fiber-AWG Input Connections via Intermediate PLC

At the output end of the AWG, light is coupled out/in to the core to/from free-space. A lensing scheme can be used to maximise the optical power launch toward the redirection module and maximise the optical power received into the core from the backward propagating beam. Typically a spherical or microsphere lens is used. The pitch of the waveguide can be designed to match that of the diffractive element array.

3.3.3 Redirection Module

The (de)multiplexing operations are accomplished by two components: the dispersion module and the redirection module. As described previously, the dispersion module carries out the primary function of spatially separating the wavelength channels. A second component is needed to reshape or reformat the linearly separated wavelengths into, in the present design, a 4x16 array format. The design of such a module was initially studied by F. Thomas Dupuis in [5]. That research was motivated by the need for a connectivity or interface solution in a multi-wavelength system that integrates MEMS, VCSELs and/or detectors that are usually designed in 2-dimemsional arrays. The micromirror-based equalizer is precisely the type of application for which the redirection module is designed and is best suited for.

The optical reformatting of a linear array into a two-dimensional array is performed with diffractive optical elements (DOEs). It is done in two steps, each with its associated array of DOEs. Firstly, the incident light is redistributed from a linear array of 1 x 64 DOE array into a 4 x 16 format (DOE1). Secondly, the beams from 4 x 16 arrays are redirected such that they exit the module (DOE2) in a parallel matter. These two operations are schematically illustrated below for 4 wavelengths:

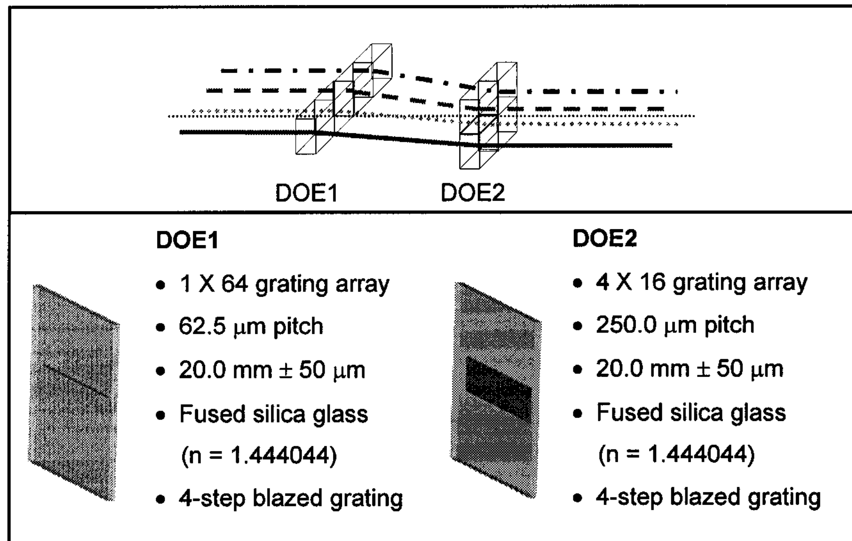

Figure 3.7: DOE1 and DOE2

The organization of the diffractive optical elements can be easily expanded for 128 or 256 wavelength channels. It requires the addition of DOE facets with only a minimal effect on the overall size of the DOE1 and DOE2 modules.

As noted in Figure 3.7, DOE1 and DOE2 are made of 4-step blazed gratings. Ideally, blazed gratings diffract an incident beam by transferring the incident energy from the zeroth order to the first order. The angular position of the outgoing beam is given by the grating equation shown here:

$$p\sin(\theta) = m\lambda \qquad m = 1 \qquad \text{Eq. 3.3}$$

Figure 3.8: Blazed Grating Equation

The two-dimensional treatment of the grating problem is straight forward, and can be found in [5]. Note that since a single wavelength traverses the grating element; there is no additional dispersion.

Multifacet blazed gratings are not easily realizable. Fabrication limitations and cost require that the gratings be approximated by finite step or level gratings, as shown in Figure 3.9. As a consequence of this discretization, the efficiency of the 1st order diffraction is reduced and incident power is shifted toward the zeroth and higher orders.

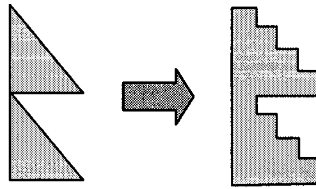

Figure 3.9: Blazed Grating vs. Step Grating

The efficiency of the step grating is given by Eq. 3.4, assuming a scalar approximation. This efficiency is a strong function of the number of steps or levels used. For example, a 4-step (N= 4) grating has an efficiency of 81%, but 95% with 8 steps.

$$n_1^N = \left[\frac{\sin(\pi / N)}{\pi / N}\right]^2 \qquad \text{Eq. 3.4}$$

In the fabricated DOEs, 4 steps are used leading to a total theoretical efficiency of 65% as two diffractive elements are traversed per channel.

The diffractive optical elements are fabricated by lithographically etching fused silica with a refractive index of n = 1.44044. Minimum feature sizes, dictated by the fabrication process, incur additional loss of efficiency in the redirection module, as only discrete and approximate grating period size can be realized. This deviation from the designed values of the periodicity of the grating causes the deviation angle, θ_m, to differ from the required value. A loss is incurred as light can fall outside the aperture of the DOE facets (beam clipping). Consequently, the aperture or size of the facet should be made sufficiently large to partially accommodate this fabrication limitation. DOE1 facets are 62.5 x 62.5

μm^2, and DOE2 facets are 250.0 x 250.0 μm^2. DOE2 output facets are pitched at 250.0 μm so as to match the standard separation of microlens arrays and MEMS array elements.

The assembled redirection module, Figure 3.10, is 20 x 20 x 5.05 mm^3 in size. DOE1 and DOE2 are separated by a small 3.05 mm glass spacer. Laboratory experiments have shown that the current design suffers from high polarization-dependent loss (-1.5dB), low efficiency (25.2%, average) and non-uniformity.

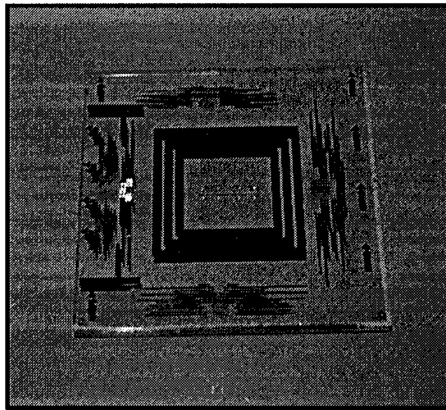

Figure 3.10: Redirection Module

The high losses can be mitigated by optimizing the diffractive optical gratings with the use of higher-step blazed gratings, while uniformity of the efficiency over the 64 wavelength channels can be increased by examining the etch depth and optimizing it for the wavelength, grating period and refraction angle θ. Alternatively, any non-uniformity in the power levels over the wavelengths can be corrected by the micromirrors. Because of the non-uniformity, a different attenuation at the outputs is obtained for a given electrode voltage for various channels. Hence, the variation can be removed by applying different electrode voltages on different micromirrors, such that more attenuation is introduced on stronger wavelength channel. Consequently, the equalizer will have a higher overall inversion loss equal to the worst case loss (the weaker wavelength) when the micromirrors are at rest.

3.3.4 Microlens Telescope

As noted in its evaluation [5], the redirection module suffers from high angular sensitivity. Small angular displacements of an incident light result in large output angle, resulting in

high attenuation-to-mirror-tilt sensitivity and a quick power drop off. A smooth attenuation drop over the entire tuneable tilt range of the micromirror is sought. As a means to compensate for the high angular sensitivity, a telescope lens system is included in the equalizer between the dispersion module and the micromirror array. The telescope lenses, shown schematically in Figure 3.12, magnify the rays or beam angles by Eq. 3.5 for object and image placed at the focus and in the paraxial region.

$$\frac{\theta_1}{\theta_2} = M \qquad \text{Eq. 3.5}$$

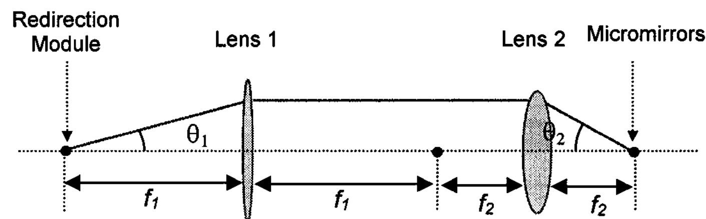

Figure 3.11: Telescoping Lenses

A magnification of ½ was chosen for the system; for a tilt angle of θ at the micromirror, the angle arriving at the dispersion module is θ/2.

In the implementation of the telescoping lenses, two options are available. The first alternative consists of using bulk macrolenses that handle all the channels as an aggregate beam. The second alternative is to use arrays of microlenses so that each channel has a dedicated set of lenses, as shown in Figure 3.13.

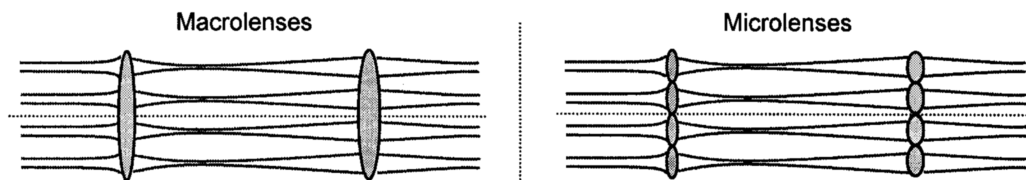

Figure 3.12: Bulk vs. Microlenses

Each of these approaches offers advantages and disadvantages in terms of costs, aberrations and alignment tolerances. The macrolens approach is easily implemented with off-the-shelf components. Furthermore, the system is more tolerant to axial misalignment of the lenses. However, a large aperture size is required to ensure that the wavelength channels are within the paraxial region of the lens. Channels far off the lens

center axis experience greater aberrations, and magnification deviating from Eq. 3.1. A more uniform performance across the channels is obtained with the uses of a microlens telescope system. It is our chosen system despite its poorer tolerance to misalignments. The uniformity was preferred as it simplifies the attenuation to tilt-voltage control calibration. Reference [34] discusses in greater details these two approaches along with a third alternative called clustered-lens.

3.3.5 Polysilicon Micromirror Arrays

The micromirrors are the active elements in the equalizer, in that they directly control the attenuation by steering the propagating light. A highly reflective planar mirror surface is desired to minimise insertion losses and aberrations; a large tilt range is desired to maximise the overall attenuation range; a fast response time is desired to increase the response time of attenuation adjustments; and a simple design is desired to ensure a high system reliably and performance repeatability.

Numerous MEMS micromirror designs exist (as outlined in section 2.2). MEMS beam steering in an equalizer application is not novel as shown in section 2.1.3. However, design decision must be made for their implementation. The fabrication technology is dictated by foundry services that are made available to us. In this matter, MUMPS (**M**ulti-**U**ser **M**ems **P**rocesses) surface-micromachining is our only option.

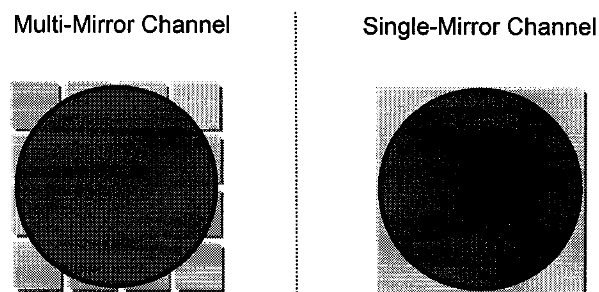

Figure 3.13: Micromirror Configuration

Given this limitation, two approaches can be chosen: 1) a single micromirror per wavelength channel; or 2) an array of micromirrors per wavelength channel, also known as a macro-pixel element [35]. In the first configuration, the incident light beam is completely redirected by the micromirror. It is a simple system design that requires a minimal number of control signals. The second configuration utilizes a large number of

micromirrors to partially reflect or redirect the incident beam. Such an equalizer would offer a better controlled attenuation and power level resolution. However, the micromirror count is significantly increased, along with the complexity of the controlling circuits. As it will be shown by our analysis, a single mirror configuration is sufficient to meet the equalizer module performance requirements and thus was chosen for this project.

As many performance requirements of the equalizers (section 1.1) are determined by the quality and electromechanical characteristics of the micromirrors. The next chapter is devoted to the design and evaluation of this vital component.

4 MEMS Micromirrors

As previously mentioned, the MEMS micromirrors play a critical role in determining the overall performance of the equalizer system. In particular, they establish the dynamic range of the attenuation, the response time, the attenuation resolution, and the system reliability. This chapter is devoted to the discussion of their design and fabrication (section 4.1), their modelling (section 4.2) and their characterisation (section 4.3).

4.1 Design

The design of MEMS micromirrors is guided primarily by the limitations of the fabrication techniques employed. Although the fabrication process imposes many restrictions, it offers the designers great flexibility in determining the exact geometry and configuration of the micromirror structures. This allows for the customisation and optimisation of the devices for a given application. For the purpose of this project, three general micromirror design types are investigated. Of the three designs, two are electrostatically actuated; while the third uses thermal expansion to create a tilting surface. Of the two electrostatic micromirrors, one is designed to exhibit a large range of tilt requiring large electrode voltages, and the other is intended for a small tilt range but with a low voltage requirement.

Prior to the description of the three designs, a discussion of the MEMS fabrication technologies available for this project is warranted. Micromachining techniques are examined with an emphasis on the MUMPS process. General design guidelines are also explained.

4.1.1 Fabrication: Bulk vs. Surface-Micromachining

Many novel techniques exist for fabrication MEMS micromirrors [36]. Generally, they are fabricated by etching or depositing layers of material onto a silicon wafer. Since these devices are micromechanical structures, the fabrication process is commonly referred to as micromachining. Two main silicon micromachining technologies exist: bulk and surface-micromachining.

Bulk micromachining consists of fabricating structures in silicon or polysilicon by anisotropic etching through the wafer. These etchants have etch rates that are dependent upon the silicon crystal orientation. For example, KOH (40%) etches the (100) wafer plane at rate of 0.6 μm/min, while the (111) plane etches at 0.009 μm/min at 70°C. The proper use of the differential rates, wafer orientation and etch stop (highly doped silicon) allow the designer to create cavities, membranes and cantilevers [36].

In surface-micromachining, instead of forming the MEMS structures in the silicon substrates, one fabricates devices by depositing thin films on the silicon surface. Two structural thin film materials are available: metal (aluminium) or polycrystalline silicon (polysilicon). While metal structure offers better conductivity and optical properties, polysilicon has become a more popular choice among designers because of its good mechanical properties. Some surface-micromachining foundry services, such as MUMPs, offer the possibility of depositing metal layer onto polysilicon surface, thus combining the advantages of both technologies. Other important materials used are silicon nitrate and silicon oxide for electrical isolation and sacrificial material, respectively. The basic surface-micromachining process, shown in Figure 4.1, starts with a silicon substrate (wafer), upon which a thin layer of silicon nitrate is deposited to isolate the substrate from the eventual device. A sacrificial layer is formed and patterned using photoresists and etchants (usually reactive ion etch). A structural layer is then deposited and similarly patterned. The two steps are repeated until the device is completely formed. Finally, the sacrificial layers are etched away leaving a free-standing structure. A drying process is then performed.

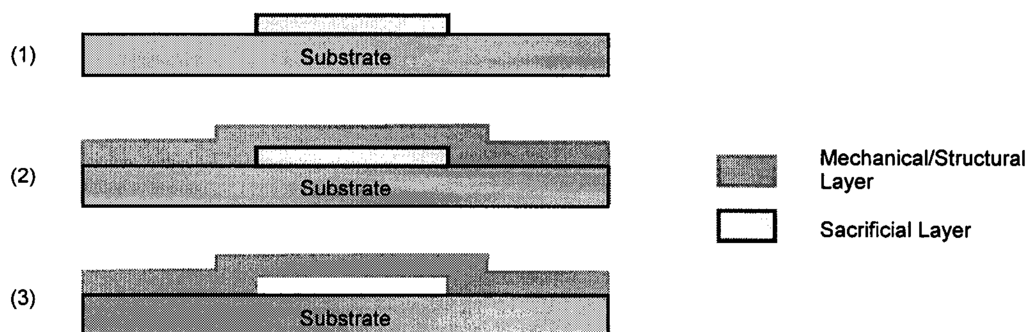

Figure 4.1: Basic Surface-micromachining Process

The advantage of surface-micromachining vis-à-vis bulk micromachining is that the structures can be usually smaller and more complex (due to the laying process). However, control of the physical characteristics of the thin film is difficult. More importantly for micromirror design, the thin film tends to lack rigidity and often adhere to the substrate (stiction) during the drying process. Consequently, surface-micromachined micromirrors are restricted to a smaller size and range of operation. Nonetheless, numerous mirrors exist that are fabricated with either or both techniques [38]-[48]. In this thesis, all three designs are polysilicon surface-micromachined using a process named MUMPS, as it is readily available to us.

4.1.2 MUMPs: Multi-User MEMS Processes

The Multi-User MEMS Processes, or MUMPs, is a three-layer polysilicon surface micromachining process made available from Cronos Integrated Microsystems to industrial and academic communities as a cost-effective, proof-of-concept and prototyping fabrication tool. The process is designed to offer simultaneously flexibility for the researchers and versatility for the multi-user environment. Of the three polysilicon layers, the top two are releasable and can be used to construct independent mechanical structures. The process allows for eight masks that are used to pattern the polysilicon and four additional layers: nitride, metal and two sacrificial oxides.

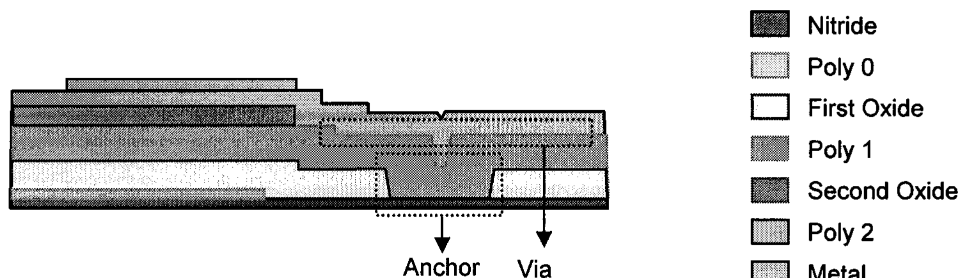

Figure 4.2: MUMPS Layers and Structures

The combination of the masks, structural and sacrificial layers offers the MUMPs' users the possibility to build a wide variety of devices. However, to permit multi-user designs on a single wafer, the 7 layers have fixed thickness. Table 4.1 summarizes the MUMPs process.

Table 4.1: MUMPs Layers

STEP	LAYER THICKNESS	DESCRIPTION
Substrate	100 mm	(100) Silicon wafer
Silicon Nitride	0.6 μm	Low pressure chemical vapour deposition (LPCVD) of silicon nitride layer on the wafer as an electrical isolation layer.
Poly 0	0.5 μm	LPCVD polysilicon layer is deposited and lithographically patterned. Poly 0 is typically used for electrical connections, and electrode structure in the micromirror design.
First Oxide *	2.0 μm	Phosphosilicate glass (PSG Oxide) is deposited. Areas in the oxide where anchor structures are formed are reactive ion etched away.
Poly 1 *	2.0 μm	LPCVD polysilicon is deposited and patterned. Poly 1 is the first releasable structural layer. Poly 1 fills the etched area of the first oxide to form anchor structures and to provide electric contacts.
Second Oxide *	0.75 μm	Phosphosilicate glass (PSG Oxide) is deposited. Areas in the oxide where via structures will be formed are reactive ion etched away. The via provides connectivity between Poly 1 and Poly 2.
Poly 2 *	1.5 μm	Polysilicon is deposited and patterned. Poly 2 is also releasable.
Metal	0.5 μm	A final Au layer is deposited, which provides contacts for probing, bonding and highly reflective mirror surfaces.

* Annealing is performed after the deposition of these layers.

For additional details on MUMPs, the reader is referred to [36]. All post-processing steps, including dicing, HF release and Supercritical CO_2 drying, are done by the Canadian Microelectronics Corporation (CMC).

4.1.3 Design Requirements

With the constraints of the MUMPS process, the design of the micromirror arrays must meet the following requirements:

- good optical surface quality
- fast and stable surface tilt control
- simplicity

Firstly and most importantly, a good optical surface quality is desired. Any scattered light at the micromirrors will increase the system's insertion loss. By a good optical surface qualify, we mean a micromirror surface with a large smooth and flat reflective area with minimum surface sag. There requirements are conflictual: larger flat surfaces are more susceptible to structural stress and surface sag as they require increased

thickness. Although a surface curvature will introduce aberrations into the reflective beam and thus will induce additional loss throughout the system, a larger reflective area is often desired. Assuming a Gaussian beam modelling, a large micromirror surface would allow for a larger beam waist size. Increased waist size would ease the alignment tolerances of the system components because the beam would diverge slower [50].

Well-designed, well behaved micromirrors are important. For fast power equalization and steady output power level, a rapid and stable surface tilt response is also required. High tilt-to-control signal sensitivity is also required for good power attenuation resolution. The dynamic range of the attenuation is limited by the maximum deflection of the micromirror surface amongst other factors. Multiple actuation techniques exist. Generally, electrostatic micromirrors can be large with faster response time; while thermally actuated mirrors tend to be slower but more stable because of the thermal deformation.

Simplicity, as in any designs, is highly desired, but it is particular important for MEMS devices. Since one and possibly more micromirrors are used for each wavelength channel in an attenuator design; large arrays are required, up to 1024 x 1024 mirrors. Simple designs will ensure a higher fabrication yield and thus will keep the MEMS approach cost effective. The reliability of MEMS devices has been pointed out by critics as their main weakness. However, MEMS micromirrors have been shown to be reliable, passing million-cycle switching tests [51] [52]. A small component count and simple structures would further add reliability of theses devices.

Other considerations guide the design of the three micromirror designs to be presented in the next section. These relate to the size and placement of the micromirror elements, which are dictated by the constraints of the MUMPS foundry service (minimum feature sizes and separation distances) and mainly by the 250 μm channel pitch of the redirection module. The three designs are layout on a single chip or die as shown on appendix A for prototype evaluation purposes. The micromirror elements are placed in a 4 x 4 array with a pitch of 250 μm.

4.1.4 Electrostatic rotational Micromirrors

As its name suggests, electrostatic rotational micromirrors work on the basis of electrostatic force attraction. A reflective surface area is suspended above electrodes by hinges attached to anchor structures. When a voltage differential is applied between the electrode and the reflective surface, an electrostatic force is set up that will reduce the gap. It is in effect a parallel plate capacitor, for which the capacitance will increased as a voltage is applied across the plates.

Numerous designs have been considered, of which two designs are presented in this section. The main difference between the two designs resides in the flexure and torsion hinges. Their size, position and geometry will determine the tilt-voltage characteristic of the micromirrors, as well as the curvature of the surface. The first micromirror was designed for a smaller operating voltage and has a small tilt range, while the second was intended for a large tilt range.

4.1.4.1 Design 1: *Electro_1*

The first electrostatic micromirror, named *Electro_1*, is a flexure beam mirror design. Two narrow and long beams suspend a reflective surface above the substrate. The free ends of the beams are anchored. An electrode is placed under the mirror surface and connected to a bond pad. As the electrostatic attraction flexes the beams toward the substrate, the long beam length minimises the strain on the polysilicon material and reduces the pull-in voltage.

Figure 4.3: SEM and Geometry of Electr_1 Micromirror

The implementation is done in three layers with POLY0, POLY1 and POLY2. The electrodes are patterned on POLY0; while the flexure beam and reflective surface are

formed with POLY1. POLY2 is deposited above the mirror surface to provide stiffness. The mirror surface is square-shaped with 175.0 μm sides. It is suspended at 2 μm above the substrate. The flexure beams are 6.0 x 84.0 μm large and 2.0 μm thick.

4.1.4.2 Design 2: *Electro_2*

In the second electrostatic micromirror design *Eletro_2*, torsion beams are implemented. The design, shown schematically shown in Figure 4.4, was intended for large tilt operation by creating larger gap between the electrode and the mirror.

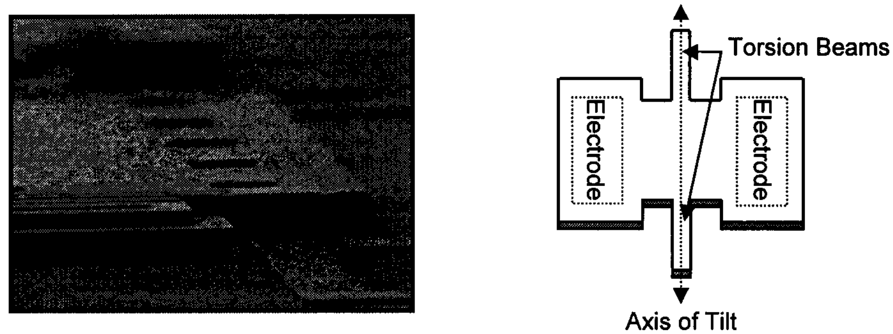

Figure 4.4: SEM and Geometry of *Electro_2* Micromirror

The following is realised by making use of the MUMPS POLY1 structural layer as sacrificial material in between the electrode (POLY0) and the mirror (POLY2). This sacrificial layer is manually removed in post-processing. The resulting micromirror has an effective reflective area of 180 x 180 μm^2, and a torsion beam size of 6 x 10 μm^2 and a separation gap of 4.75 μm. The larger gap is expected to allow for large tilt angle while the torsion beam allows for a better angle control at the cost of a higher electrode voltage.

4.1.5 Thermal Rotational Piston Micromirrors

A thermal micromirror uses the thermal expansion of polysilicon structures to actuate a reflective surface. The rotational piston micromirrors are based on designs developed by W.D. Cowan and V.M Bright at the Air Force Institute of Technology [51]. Polysilicon does not exhibit a piezoelectric behaviour, which is normally used in other crystalline material for actuations. However, polysilicon and silicon, generally, does have a good thermal expansion coefficient (α). This coefficient can vary with manufacturing condition and temperature, but it is typically about 2.69 x 10^{-6} K^{-1} at room temperature.

4.1.5.1 *Thermo_1*

To create a rotation piston mirror, a circular reflective surface is suspended above a substrate by two thin and two thicker arms, as shown below.

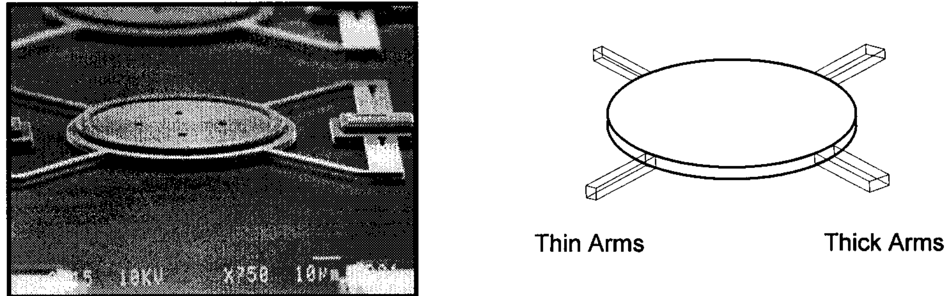

Figure 4.5 SEM and Geometry of *Thermo_1* Micromirror

As a voltage is applied across the mirror structure, a current flow is generated in the arms. The current flows cause the polysilicon to heat up and expand, causing the central surface to drop. A tilted surface is obtained because of the asymmetry of the arm sizes. The higher current density causes the smaller arms to expand faster than the larger ones. Setting the current flow (or voltage potential across the arms) allows one to control the tilt angle.

The implementation of the design in MUMPS, called *Thermo_1*, is done with 3 layers: POLY0, POLY1, and POLY2. POLY0 is used as a based layer above which the circular surface is suspended. The circular mirror and the two pairs of suspending arms are formed with POLY1. POLY2 is deposited atop of the central surface to provide rigidity to the thermal mirror. Anchors placed at the free end of the suspending arms provide structural support and electrical connectivity to the bonding pads. The effective mirror surface has a diameter of 150 μm; the arms are 4 and 7 μm wide and 60 μm long. Like the previous designs, the thermal mirrors are arrayed with center-to-center separation of 250 μm.

In all three designs, the releasable surfaces must include etch holes placed at every 30 μm over the entire surface area. For POLY1, POLY2 and Metal layers, the holes are 2 x 2 μm^2, 4 x 4 μm^2, and 6 x 6 μm^2, respectively.

4.2 Micromirror Numerical Models

With the designs of the three micromirrors described, the numerical modelling of the devices is presented in this section. Despite the many constraints imposed by the fabrication process for the structures' material and dimensions, flexibility exists for customizations as exemplified by the three designs. To ensure that they perform as intended, numerical models are created. These models can determine the electro-mechanical behaviours of the mirrors and ensure that the proper electrode to surface gap size, mirror dimensions, and hinges/flexure beam designs are chosen. Two types of modelling are used to this purpose: an electrostatic parallel-plate capacitor model and finite element model. The former method is used to characterise the two electrostatic micromirrors, *Electro_1* and *Electro_2*; while the latter analysis is used to model both the structural and thermal-mechanical behaviours of all three micromirror types.

4.2.1 Simplified Models: Electrostatic Capacitor Models

For electrostatic micro-actuators, the electrostatic capacitor model is a rapid and accurate method for performing a pull-in analysis. For these structures, the actuation is the result of a balance between an electrostatic force and a mechanical or structural force. In static equilibrium, these two forces are equal resulting in a stable actuation condition and a constant mirror position. As the voltage differential between the *capacitor plates* (between electrode and mirror surface) is increased, the electrostatic force increases and eventually overcome the mechanical force. The plates become unstable and usually collapse to cause a surface contact. This point is referred to as the *pull-in* condition and the corresponding voltage as the pull-in voltage. The tilt angle of the mirror surface at *pull-in* is designated as the pull-in angle or the maximum tilt angle. This angle does not necessary correspond to the maximum physical tilt allow by the micromirror's structure, but is the point up to which the operation of the micromirror is stable. In rotational capacitor modelling, the electric potential difference is applied to a portion of the plate or mirror surface, such that an electrostatic torque is created about the beam axis. The flexure beams or hinge structures provide the restoring mechanical torque to counterbalance the electrostatic torque.

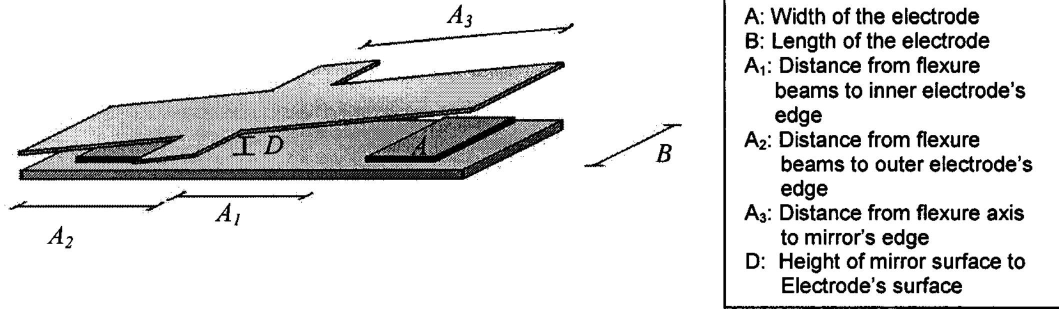

Figure 4.6: Generalized Torsional Micromirror Design

Figure 4.6 illustrates a general torsion micromirror design with all relevant parameters for determining the electrostatic torque. If one assumes that the mirror surface or plate is infinitely wide but of length A_3, the electrostatic torque generated by a voltage V applied on a rectangular A x B electrode at a distance D and angle α is given by the following equation [53]:

$$M_{elect}(\alpha)=\frac{\varepsilon_0 V^2 B}{2\alpha^2}\left[\frac{D}{D-A_2\alpha}-\frac{D}{D-A_1\alpha}+\ln\left(\frac{D-A_2\alpha}{D-A1\alpha}\right)\right] \qquad \text{Eq. 4.1}$$

The equation assumes small angle approximations. ε_0 is the permittivity of the air separating the electrode and the micromirror surface. Note that since the surface is assumed to be infinitely wide, fringing field effects are ignored. As the electrostatic torque pulls the upper surface toward the electrode, the flexure beam or hinges produce a restoring mechanical torque. This physical response can be modelled as a spring and the torque can be expressed as:

$$M_{mech}=K_\alpha \alpha \qquad \text{Eq. 4.2}$$

K_α is the spring constant of the beam structures and is dependent on the type, material and the dimensions of the beam. For a flexure beam micromirror, *Electro_1*, the spring constant is as shown in Figure 4.7/Eq. 4.6 on the next page.

E is the Young's modulus. It gauges the elasticity of the material. Its value is dependent on the manufacturing process with typical values in the range of 130-180 GPa for MUMPs polysilicon [54] [55].

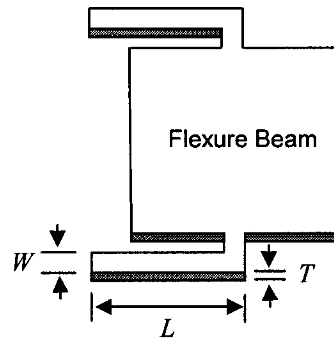

$$K_{\alpha} = \frac{EWT^2}{6L}$$ Eq. 4.3

Figure 4.7: Flexure Beam Micromirror

For torsion spring hinges (*Electro_2*) the expression for the spring constant, Eq. 4.4, involves the shear modulus of polysilicon, G, which is related to Poisson ratio, v, by Eq. 4.5. Typically, G and v is 65 GPa and 0.28 respectively for polysilicon [53].

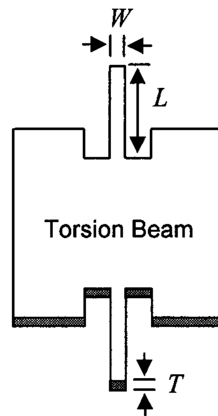

$$K_{\alpha} = 2\frac{GWT^3}{3L}\left[1 - \frac{192}{\pi^2}\cdot\frac{T}{W}\tanh\left(\frac{\pi W}{2T}\right)\right]$$ Eq. 4.4

$$G = \frac{E}{2(1+v)}$$ Eq. 4.5

Figure 4.8: Torsion Beam Micromirror

Assuming that the applied voltage V is constant, the solution to the equation equating the electrostatic torque (Eq. 4.1) and the restoring torque (Eq. 4.2) will yield the angle of the micromirror under the applied voltage [53].

$$K_{\alpha}\alpha = M_{elect}(\alpha)$$ Eq. 4.6

For low voltages, Eq. 4.6 produces two solutions, where only one is stable and corresponds to the physical solution. At one voltage, the two solutions coincide. This voltage and the corresponding angle α are to the pull-in voltage and angle. Specifically, for the two electrostatic micromirror designs, *Electro_1* and *Electro_2*, the following tilt vs. voltage relationships are obtained.

Table 4.2: Capacitor Plate Model Specifications and Results

SPECIFICATIONS		
	Electro_1	*Electro_2*
A_1	21.20 μm	21.00 μm
A_2	76.20 μm	76.00 μm
A_3	87.20 μm	84.00 μm
B	152.00 μm	152.00 μm
D	2.00 μm	4.75 μm
W	6.00 μm	6.00 μm
L	95.00 μm	10.00 μm
T	2.00 μm	1.50 μm
E (Young's)	169.00 GPa	169.00 GPa
G (Shear)	na	69.26 GPa
RESULTS		
Pull-in Voltage	8.35 V	85.89 V
Pull-in Angle	11.30 mrad	26.90 mrad

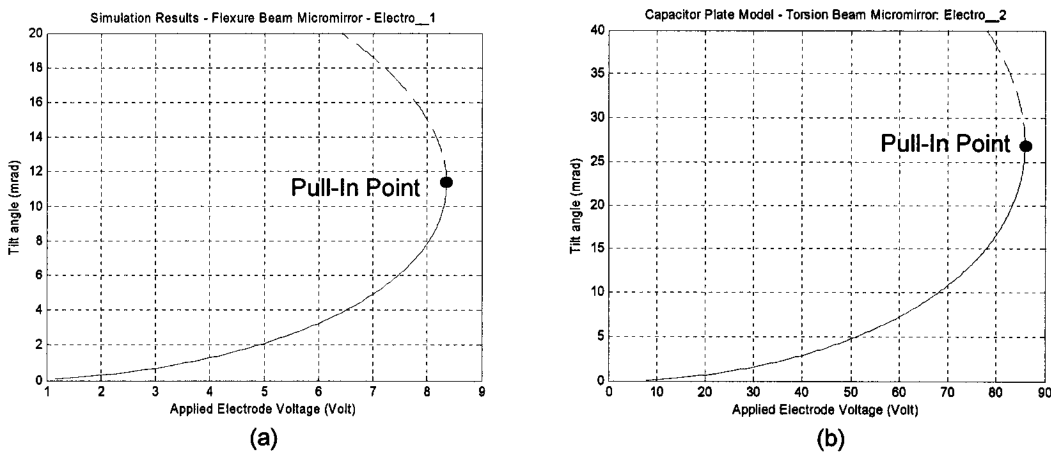

Figure 4.9: Small-angle Solutions. The markers denote the pull-in point
(a) Small tilt (Electrod_1) (b) Large tilt (*Electro_2*)

The capacitor plate modelling of the two micromirrors demonstrates that both devices will perform as they were designed for. *Electro_2* exhibits maximum controlled tilt (pull-in angle) that is more than twice that of *Electro_1*. However, the required voltage to obtain this tilt is over 85 V. Both designs are appropriate for the equalizer design; the choice would be determined by the tilt range required to meet the attenuation range requirements. Furthermore, surface quality including the sag and curvature of the micromirrors would be an additional factor to be considered (section 4.3.2.1).

4.2.2 Finite Element Model (FEM)

The presence of surface sag and curvature that are inherent to the device structures can be predicted using a finite element model (FEM) of the micromirror designs.

FEM or finite element analysis (FEA) is a piecewise approximation to the solution of the partial differential equations describing the stress, electrostatic/magnetic or heat transfer problems. The exact geometries of the micromirrors are considered in FEM, as opposed to in the capacitor plate model. In the analysis presented this section, the presence of any significant initial structural stress of the three micromirror devices will be examined with FEM. For the thermally-actuated micromirror, FEM can extract the thermal expansion of the polysilicon structures and thus provide detail characterisation of the device, including the surface-tilt vs. voltage behaviour.

The specific of FEM theory can be found in [56] [57], its discussion is beyond the scope of this thesis; however, the basic steps of a finite element analysis are:

Step 1: *Creating and discretizing the solution domain. This includes the studied structure and the surrounding area such as the surrounding air volume for an electrostatic field distribution analysis. In creating a physical model, one must balance simplicity and accuracy. Symmetries should be exploited and extraneous structural details ignored. This minimise computations and ensures fast solution convergence.*

Step 2: *Applying boundary conditions (fixed anchors, non-movable elements), initial conditions (stress loads) and loadings (force, voltages, current).*

Step 3: *Solving the matrix equations, representing the physical behaviour of the discretized elements. This can take several iterations for converging solution. Unstable solutions are flagged.*

The finite element analysis of the three micromirror designs are performed via a commercially available software package called *ANSYS* [58]. *ANSYS* automates these various FEA/FEM steps. FEM results of *Electro_1*, *Electro_2* and *Thermo_1* follows.

4.2.2.1 *Electro_1*

In the earlier sections, we demonstrate that *Electro_1* exhibit a small tilt range and a small pull-in voltage. However, it remains to be determined by FEM if the configuration of flexure beams causes any surface deformation, sag or structural stress. In the meshed-model of the design (Figure 4.10), note that only necessary structures are created, while features such as etch holes that do not significantly affect the structural solution are neglected. Material properties, namely those of polysilicon, are listed on Table 4.3. These values are obtained from literature and are generally accepted. The Young's Modulus is taken as the average of several published values and matched the value used in the parallel capacitor plate model.

Table 4.3: Polysilicon Material Model

Young's Modulus	169e3 $\mu N/\mu m^3$
Poisson's Ratio	0.22
Mass Density	2.3e-15 $kg/\mu m^3$
Damping Coefficient	9.3e-8 $kg*\mu m^2/s*rad$

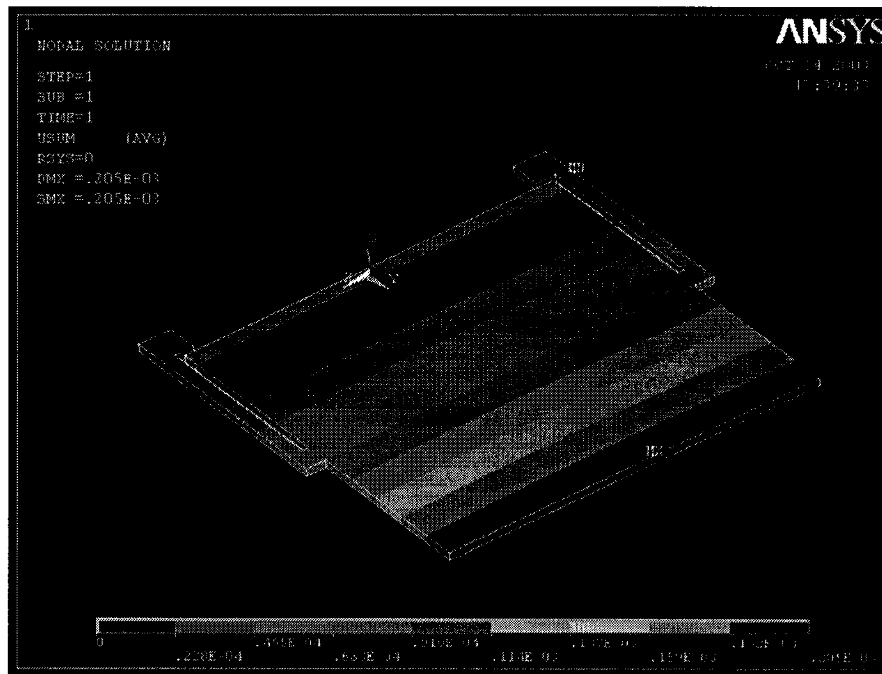

Figure 4.10: *Electro_1* Surface Sag

By applying a gravitational inertia, one would obtain the surface sag or position with no applied electrode voltage. The residual stress that is introduced during the release process during fabrication is not included (see section 4.1.2). This stress amplifies the

deformations. As shown in Figure 4.10, the micromirror is sagged forward due to its own mass, with no apparent curvature. The displacement is in the order of tenths of nanometres with a maximum of 0.20 nm at the edge of surface. This initial sag is negligible; the two supporting flexure beams provide sufficient stiffness to suspend parallelly the surface above the electrode.

4.2.2.2 *Electro_2*

Figure 4.11 shows the similar finite element analysis for the electrostatic micromirror *Electro_2*. At rest, the micromirror is sagged toward the center of the surface. Again, the deformation is negligible, in the scale of hundredth of nanometers, as shown in Figure 4.11. *Electro_2* mirror structure is thinner that that of *Electro_1*, although the total mass is reduced, the surface stiffness is also reduced. Overall, the surface sag is smaller than that of former design. The torsion hinges seem to provide significantly more support in maintaining a top surface in parallel with the substrate; however, as it has been shown, a higher pull-in point is obtained.

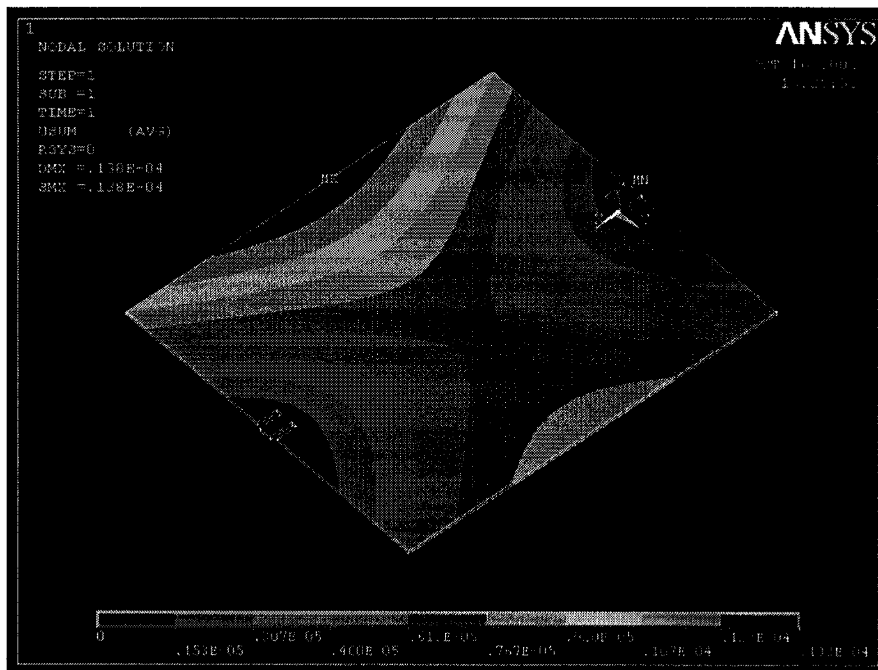

Figure 4.11: *Electro_2* Surface Sag

4.2.2.3 *Thermo_1*

In section 4.2.1, no simplified model of the thermally actuated micromirror was provided, although it can be done [59]. The method consists of representing the thermal mirror by an array of resistors and thermal conductors. The mirror model is subdivided into segments (elements) on which electrical and thermal analyses are sequentially applied. An FEM simulation fundamentally performs the same analysis.

An ANSYS FEM characterisation of the thermal micromirrors is accomplished in two stages. Initially, the temperature distribution over the mirror structure with an applied voltage is determined. Currents and heat flows in the structure are obtained. Secondly, a thermal stress analysis is performed to obtain the expansion of the arms and reflective surface. Figure 4.12 depicts the discretized model, on which an initial gravitational stress analysis was performed (Figure 4.13). A small surface sag is observed. However, because of the asymmetry in the arm design, the surface is tilted toward the one end. The larger thickness of the central (4 μm) provides sufficient rigidity to maintain a planar surface.

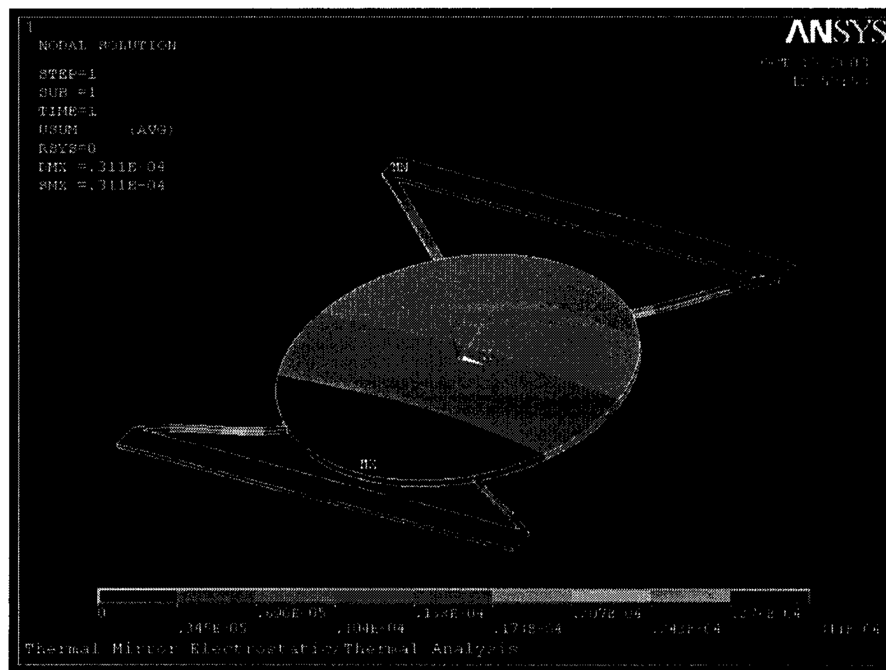

Figure 4.12 *Thermo_1* Surface Tilt at Rest

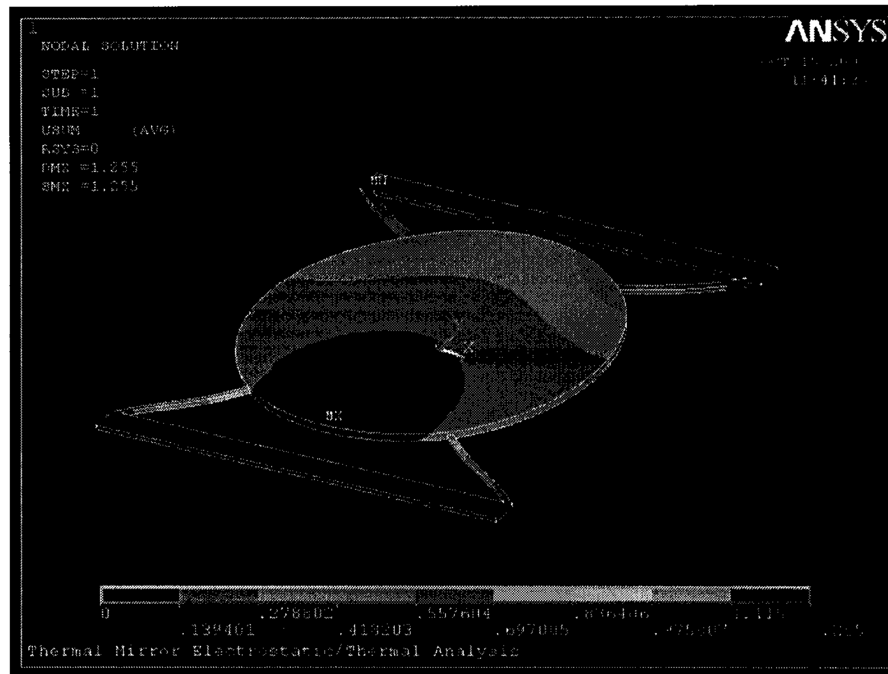

Figure 4.13: *Thermo_1* Surface Tilt at 17V

Under an applied voltage, the deformation occurs mainly in the arms where the heat flow densities are highest. As the arms deform and bulge, they exert a force on the central disk at the contact points. The surface deforms under the stress resulting in non-uniformities as shown in Figure 4.13.

As opposed to the electrostatic actuated micromirror, the *thermo_1* type mirror does not have a pull-in point. The tilt of the surface is controlled and stable up to the physical limits of the mirror design. Neglecting the deformation, a small tilt is obtained with a small applied voltage. As seen in Figure 4.14, the behaviour is surprisingly linear, offering the same tilt-voltage sensitivity throughout the micromirror range of operation. Maximum tilt, at 2.1 mrad, is significantly smaller than that of the electrostatic devices. This is due in part to the limited thermal expansion of polysilicon.

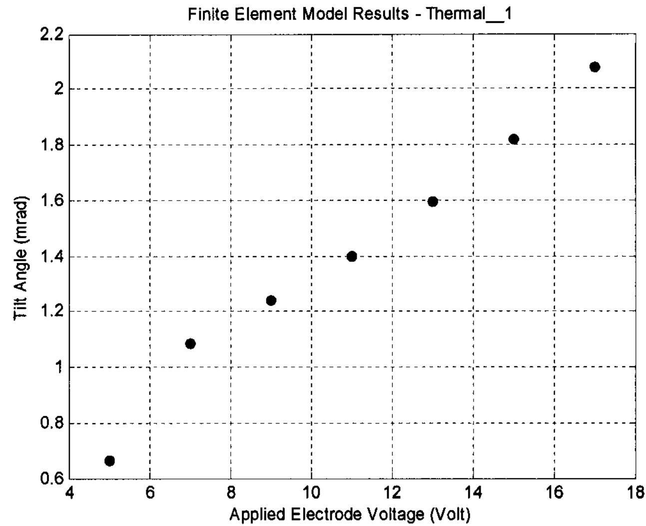

Figure 4.14: Thermo_2 Tilt-Voltage Characteristic for FEM

4.3 Micromirror Experimental Characterisation

The simulation results confirm that the micromirror design would perform as desired; however they only predict their electro-mechanical performance. No information on their optical property has been inferred. Furthermore, the fabrication introduces variations on the structures and materials that would cause deviations from the simulation results. Particularly, the Young's modulus of elasticity of polysilicon can significantly vary from fabrication runs to another. Its numerical value is critical to the simulation results. A full experimental characterisation is required.

The measurements of interest include the surface profiles of the devices at rest and during active operations (actuation), and the optical reflectivity measurements. Scanning electron microscopy (SEM) is used to image the surface of the micromirrors; unfortunately, SEM does not provide any quantitative information about the profiled surface. Vertical scanning interferometry (VSI) and phase shifting interferometry (PSI) are useful for obtaining accurate height information and for measuring surface deformations. Seidel and Zernike aberration coefficients can also be fitted to any curved surfaces, from which tilt angle can be inferred [62] [63]. VSI and PSI is based on the creation of interferograms on the surface of the observed object. These are then analysed to extract topographical information. The optical setup is similar to that of a folded Michelson interferometer. A piezo-electric element translates the interference objective

vertically, while a charge-coupled-device (CCD) camera captures the changing interferogram patterns. The correlations between the patterns and the positions of the piezo-electric element provide accurate, sub-nanometres relative height information. This extraction is explained in greater details in [61]; here, the surface profiles are done with a method that combines both the VSI and PSI techniques.

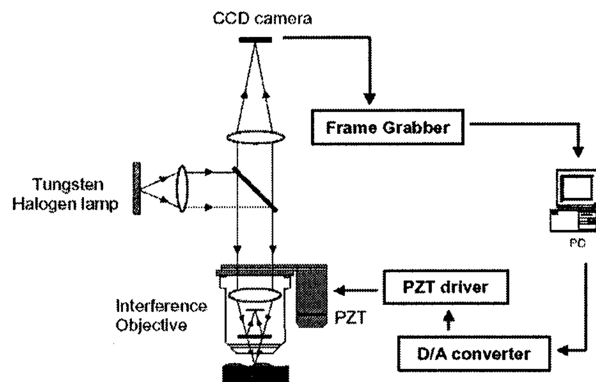

Figure 39: VSI/PSI Setup [61]

4.3.1 Electromechanical Characteristics

The experimental results for *Electro_1* and *Electro_2* are presented in the following sections. The observed actuation of the thermal micromirror, *thermo_1*, will also be discussed. Here, the tilt of the mirror surface at a given actuation point or electrode voltage is determined by extracting the first order tilt coefficient of the Seidel aberration polynomial fitted to the profiled surface.

4.3.1.1 *Electro_1*

Electro_1 exhibits a better than expected performance in the laboratory. The measured voltage for pull-in is lower than predicted by the capacitor plate model. Figure 4.16 shows the results obtained from the simulations and the interferometric measurements. A pull-in voltage of 6 V is obtained at an angle of 8 mrad. The results suggest that the flexure beam is less rigid than predicted by the earlier simulations. Despite this discrepancy, the micromirror's tilt vs. voltage trends are as expected; a smooth exponential curve is obtained.

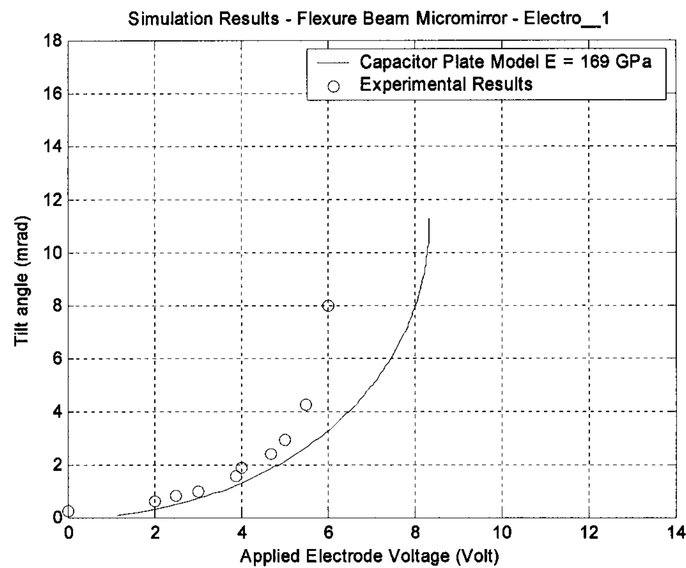

Figure 4.16: *Electro_1*- Comparative Results

Inaccuracies in the results are necessarily incurred in laboratory experiments due to noises and instrument limitations. The differences suggest that the model simplifications and parameters, inherent to the capacitor plate modelling, may need some adjustments to properly account for the device physical and electrical properties. However, this discussion is beyond the scope of the thesis. Here, the purpose of the simulations is to guide the designs of the micromirror and offer an estimate characterisation of the physical devices. Interferometric measurements on multiple samples yielded similar tilt-voltage values, and thus provide the confidence we required in the experimental results. Fundamentally, *Electro_1* behaves as intended, small tilt range with small required electrode voltage.

4.3.1.2 *Electro_2*

The same discrepancies between the simulation and experimental results are observed for the *Electro_2* micromirror. And like *Electro_1*, *Electro2* performs as it was designed for: large tilt range requiring large voltage differentials. The various results are aggregated on Figure 4.17. A pull-in voltage of 71.0 V is obtained at an angle of 20.0 mrad.

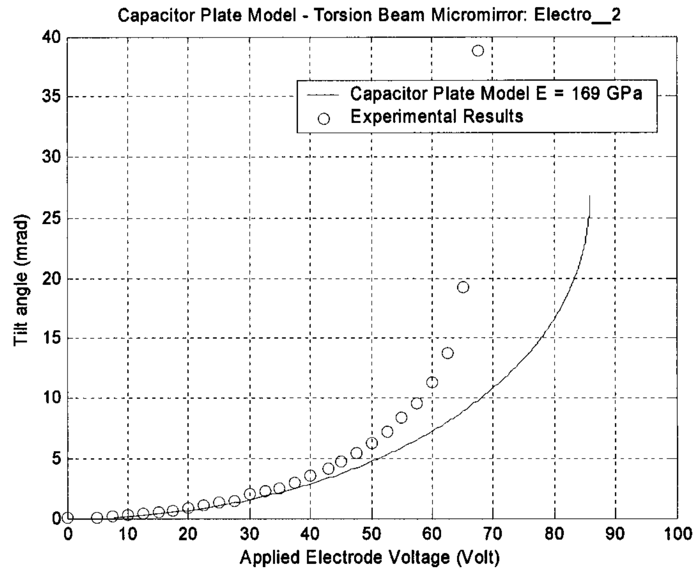

Figure 4.17: *Electro_2* - Comparative Results

4.3.1.3 *Thermo_1*

The FEA model of the thermally actuated micromirror, *thermo_1*, indicates that the expansion of the supporting arms would result in a small tilt of the circular mirror surface. However, in the laboratory, the samples did not properly actuate, hence no data is available for comparison. It is believed that residual stress introduced in the release step in the MUMPS process may have caused significant surface stiction, resulting in a short-circuit with the substrate. The four supporting arms didn't not provide sufficient rigidity to suspend the mirror mass.

4.3.2 Optical and Surface Characteristics

The surface sag that is caused by the structural mass, residual stress that is introduced during structural release and surface stiction between polysilicon layers are best measured by observing the 3-dimensional profile of the micromirror surface at rest (section 4.3.2.1). Reflectivity of the micromirror polysilicon/metal surfaces was also measured using a simple optical bench setup. The wavelengths of interest, 1.527 μm to 1.578 μm, are covered (section 4.3.2.2).

4.3.2.1 Surface Curvature

Ideally, a flat planar surface is desired for the micromirrors. Any surface sag and curvature introduces a loss in the equalizer system affecting the insertion loss and the obtainable attenuation levels. The design of the equalizer requires that the optical beam returns through the system following the reverse path once it is reflected off the micromirror. It is essentially a folded symmetric optical system with the micromirror as the point of inflection. A curved mirror surface would focus the incident light, thus introducing unwanted wave front curvature in the returning beam and the system loses its symmetry. Each component is designed or chosen such that their aperture would be optimized for a given beam size. An asymmetric system would cause the beam size to diverge from its designed value and cause clipping and power loss across the components.

The simulation results presented in section 4.2.2 show that for the three possible micromirror designs, the surface sag is not significant as the flexure and torsion support beams, and the thickness of the surface provide sufficient rigidity. However, under laboratory observations (only for *Electro_1* and *Electro_2*), the thinner micromirror design, *Electro_2*, exhibits considerably more deformation at rest than suggested by the finite element model (Figure 4.18). The simulations do not take into account the surface stresses introduced during the fabrication process. The measurements show that they are the dominant causes of surface sag/curvature.

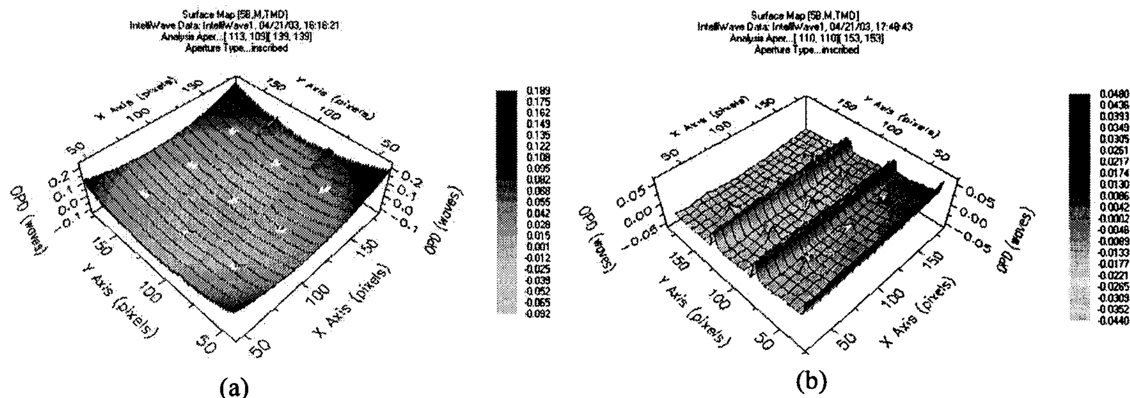

Figure 4.18: Surface Profile/Curvature (a) *Electro_2*: Surface at rest shows significant curvature (b) *Electro_1*: Surface at rest shows only an initial tilt

Electro_1 exhibits sag with a measured optical path difference (OPD) of 0.046λ (crest to trough); while *Electro_2* has an OPD of 0.281λ with λ, the wavelength of the profiler, at

640 nm. The surface of *Electro_1* is considerably more planar than that of *Electro_2*, where the measured radius of curvature surface is 18.8 mm corresponding to a focusing power of F/44.8. As the applied electrode voltage is increased, and the mirror surface is deflected, the curvature diminishes. As shown in Figure 4.19, the F-number of the curved mirror grows exponentially with increasing electrode voltage. Thus, its converging power is reduced. Although the curvature becomes negligible, the voltage dependence of the curvature renders the optimisation of the attenuation-voltage characterisation difficult.

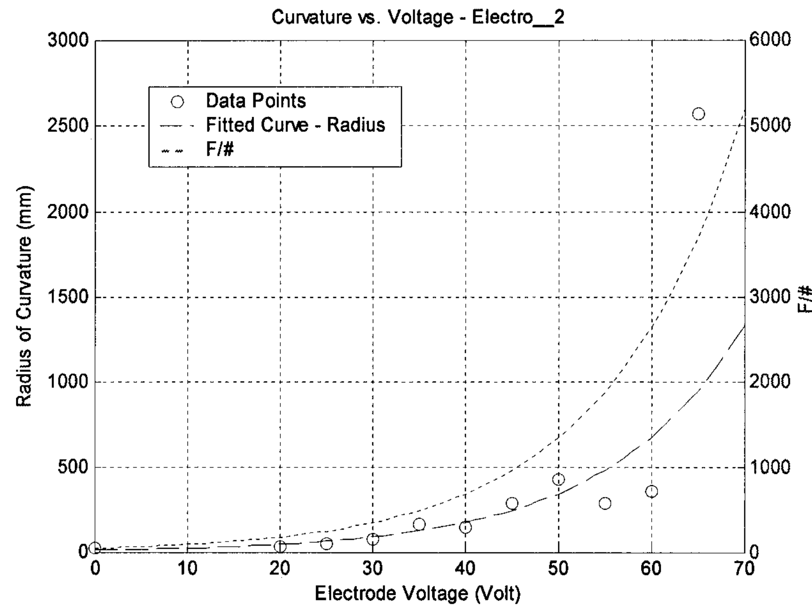

Figure 4.19: Curvature of *Electro_2*

Accounting for the curvature consists of ensuring that the beam size remains sufficiently small for all the clear apertures of the micro-optics and microlens for the worst curvature (F/#). The problem will be treated in the discussion of the system design using Code V (Chapter 5). However, it is important to note that, although surface sag is present, their effects are small, and that compensating for it in the system by reducing the beam size will engender other problems, mainly decreased component alignment tolerances.

4.3.2.2 Reflectivity

An assessment of the optical reflectivity of the micromirrors is important for the characterisation of the equalizer insertion loss and attenuation levels. Surface irregularities and etch holes cause the scattering and diffraction of the incident light.

Figure 4.44 shows the surface quality of the polysilicon material with 0.200 nm peak-to-valley roughness. Etch holes, placed regularly at 30 μm over the area of the mirror surface to facilitate structural release, are sized 4 x 4 μm^2 for polysilicon and 6 x 6 μm^2 for metallized surface. The edges diffract light; while the holes themselves cause power to be absorbed.

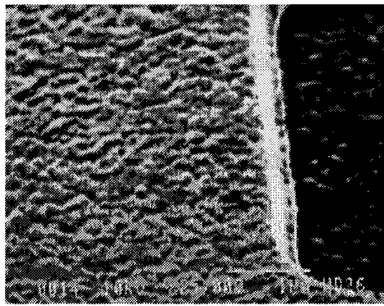

(a)

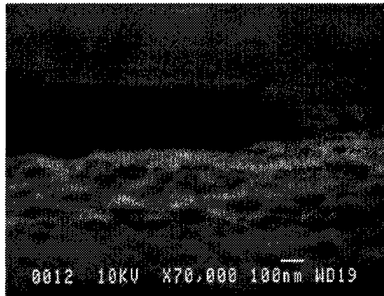

(b)

Figure 4.44: Surface Close-up
(a) x25,000 (b) x70,000

A thorough investigation of these effects on the reflectivity of surface-micromachined polycrystalline silicon was undertaken by J. Zou et al. The results are presented in [64]. The measurements presented here are based on that research, but are adapted for our system specifications. The optical bench setup, schematically depicted in Figure 4.21, utilizes an optical power meter and detector to collect light reflected from the polysilicon samples via a 50:50 optical beam splitter. The source is an ECL tuneable laser operating at 1.527 μm to 1.578 μm.

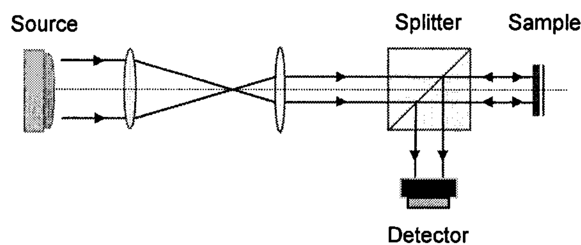

Figure 4.21: Reflectivity Measurement Setup

Measurements were made for both the MUMPS POLY1 and POLY2 structural layers and for the metallized (Au) surfaces.

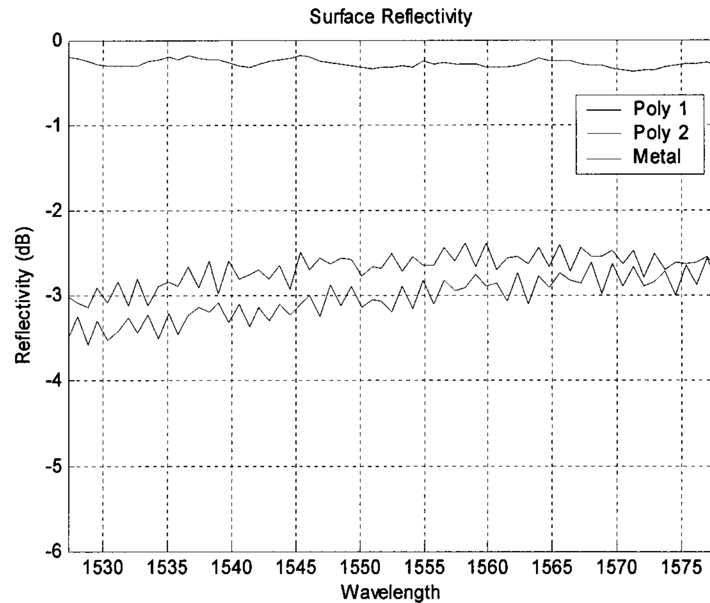

Figure 4.22: Surface Reflectivity of MUMPS Materials

The median reflectivity of the three materials are, respectively, 2.66 dB (54.2%), 3.08 dB (49.2%) and 0.29 dB (93.5%). Metallized surfaces are significantly more reflective; despite the presence of larger etch holes. However, the deposition of metal in the MUMPS process comes at a cost: increased surface curvature. The MUMPS fabrication lacks an annealing step after the deposition of the metal layer resulting in increased residual stresses on the surface [49]. For the purpose of our evaluation, both electrostatic mirrors were not metallized. With a loss above 2.66 dB, they are not suitable for the equalizer for which an insertion loss of 1 dB is desired. Metallization is required, particularly with the inefficiencies of the DOEs. The surface curvature would have to be dealt with accordingly (section 4.3.2.1). Other fabrication processes should be also considered.

The electrostatic micromirrors are both good candidates for the equalizer design for their electro-mechanical characteristics: good tilt range, low surface sag and surface curvature. In the next chapter, the attenuation and insertion losses of the system are examined with respect to the micromirror tilts, surface quality. In these analyses, the other components are considered for their impact on the propagating signals.

5 Equalizer Modelling and Characterisation

This chapter presents a characterisation of the equalizer module through numerical modelling. Previous sections described the various subcomponents of the system: the circulator, the (de)multiplexer modules, and microlenses, and with greater details, the micromirror arrays. In this present section, the integrated system is investigated; in particular, the quality and the position of the optical beam are examined at the interface between the various components. From the results of these analyses, attenuation characteristics of the equalizer can be retrieved.

5.1 Equalizer Attenuation Modeling

The modelling of the integrated system simplifies the design problem by neglecting two components: the circulator and the dispersion modules. The optical circulator can be omitted as it does not play a part in the two primary operations of the equalizer module, namely the (de)multiplexing and the reflection of the light beam. The circulator does not affect the attenuation performance of the system.

The operation of the dispersion module, for simplicity, was neglected in the numerical modelling. The design and implementation of a dispersion module was not done for this thesis, and thus will not be included in the experimental setup of the equalizer. Instead, the 64 input wavelengths are assumed to be formatted in a linear array with each channel properly pitched. The numerical model will focus on the principal components of the equalizer: the redirection module and the micromirrors. The importance of the dispersion module in the system is limited to the additional insertion loss that it incurs and the transformation of the beam shape/size from its output ports. To account for these effects in the model, the dispersion operation can be replaced by a set of transforming lenses and a fiber coupler (Figure 5.1). The coupling loss (or attenuation) that occurred at the fiber coupler is similar to the loss that occurred at the output port of the AWG. The removal the dispersion module greatly simplifies the numerical modelling of the system, yet providing the critical results.

5.1.1 Modelling Considerations

With the two design simplifications considered, the modelled system looks as follows:

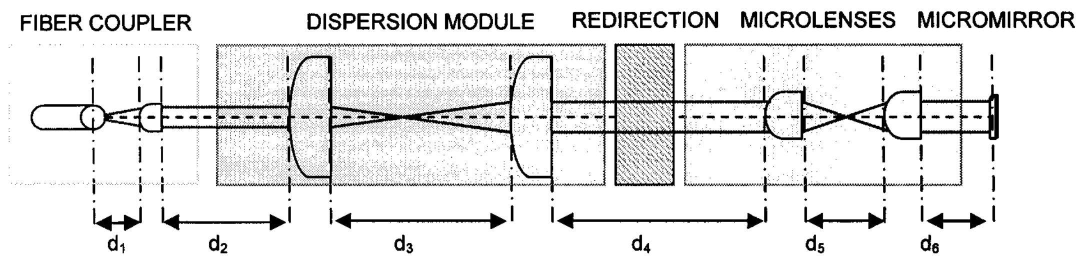

Figure 5.1: Modelled System

The optical signal enters the system though a fiber coupler. The fiber coupler allows for a better optical power transfer in and out of the optical fiber. Typically, it consists of a simple lens placed at that focal length from the fiber facet. The lens magnifies the angle of acceptance of the fiber core. In our simulations, an aspherical lens with 5 mm aperture and 6.2 mm focal length is used, corresponding to an OZ Optics coupler [65] that is used in our laboratory setup.

The redirection module was design with input grating facets (DOE1) that are 62.5 μm x 62.5 μm in dimensions. Assuming a Gaussian intensity profile, the incident signal requires a beam waist of 20.8 μm to guarantee that 99% of the power would be transferred at DOE1 before it is diffracted by the gratings. Two lenses in a telescope Gaussian expander (compressor) configuration are used to reshape the light beam outputted from the optical coupler to the required beam size. A magnification of x 0.033 is required as the Gaussian beam waist after the coupler is 690.0 μm.

The redirection module can be properly modelled. Diffraction angles can be obtained from the specified grating period. An important consideration in the simulation of the redirection module is that for the 64 wavelengths the light beams do not traverse the same path length because of the two-dimensional formatting. The differences are small (less than 1%); however, they can result in noticeable changes of the output Gaussian beam waist.

The microlens system consists of two f/28 and f/14 planar convex microlenses. The focal length ratio provides a magnification factor of x½, thus reducing the sensitivity of the beam tilt at the DOEs by half of the micromirror tilt (see section 3.3.4). The aperture of the microlens is 250 μm corresponding to the pitch of the output array of the redirection module. The final elements of the system, the micromirrors, are modelled as simple, slightly curved reflective surfaces with an aperture corresponding to the micromirror designs discussed in section 4.1.

Table 5.1 summarises that the lens specifications used in the modelling of the simplified equalizer module.

Table 5.1: Lens Specifications

LABEL	APERTURE (radius)	RADIUS OF CURVATURE	FOCAL LENGTH	f-NUMBER	THICKNESS
FIBER COUPLER					
LENS1	2.5 mm	2.754 mm	6.2 mm	f/3.1	1 mm
DISPERSION MODULE					
LENS2	6.5 mm	225.158 mm	500 mm	f/77	3 mm
LENS3	5.0 mm	8.212 mm	15 mm	f/3	3 mm
MICROLENSES TELESCOPE					
LENS4	125.0 μm	1.555 mm	3.5 mm	f/28	1 mm
LENS5	125.0 μm	0.778 mm	1.75 mm	f/14	1 mm

The distances between the lenses (Figure 5.1) are key considerations in the both the design of the equalizer and in the simulations. A fully symmetric system is desired, such that the forward and backward propagating light beams traverse similar paths that only differ by the slight tilt introduced by the micromirrors. To realize such a optical system, one must ensure that the distances separating the lenses, microlenses and micromirrors are such that the waist position of the Gaussian beam coincides with the effective focal length.

In this configuration, the image Gaussian waist of one lens is located at the effective focus of the subsequent lens (as its object waist) to ensure symmetry. A relay configuration is obtained, as shown on the next page (Figure 5.2).

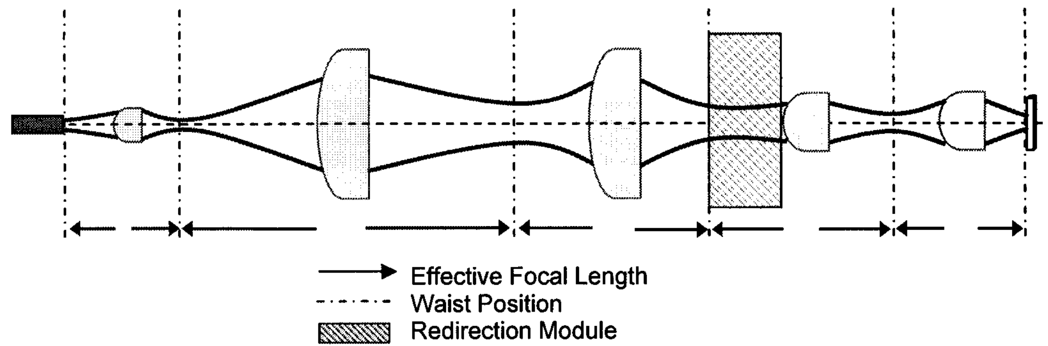

Figure 5.2: Focus-to-Focus Configuration

The exact distances between the vertices of the lenses are tabulated below. The lenses and microlenses are plano-convex with a glass index of 1.44413 at λ = 1.527 μm, and with thickness from 1 to 3 μm. Simple thin lens equations are not sufficiently accurate to compute these distances. The dispersion of the beam limits and has an impact on the lens separation. A matrix formulation is used; the propagation of light is thus handled from surface to surface.

Table 5.2: Lens Separation Distances

d_1	6.20 mm
d_2	505.49 mm
d_3	516.42 mm
d_4	21.45 mm
d_5	4.56 mm
d_6	1.06 mm

When determining these values and the power of the lenses, the Gaussian beam sizes must be carefully examined. The matrix method allows us to considerer this via the bilinear transform of the Gaussian beam parameters. Appendix C details this analysis. The results are analysed using optical design software (Section 5.1.2.1).

Since the lenses are arranged confocally (relay configuration), it is important that the optical system contains an odd number of lenses to ensure that a large coupling loss can be obtained at the position of the fiber when the reflected beam angle is changed. An optical fiber is designed with a large numerical aperture (NA) in order to maximise their light-gathering power. Typically, a single mode fiber (SMF) has a NA of 0.1 to 0.4, resulting in an acceptance angle in the range of 90 mrad.

If an even number of lenses is used in the relay configuration, a tilt ($\Delta\theta_2$) introduced by the micromirror would simply result into a change of angle, $\Delta\theta_1$, at the output. Given the large NA of the fiber, only minimal coupling loss would be incurred, resulting in limited attenuation range. Large deflection angles would otherwise be required by the micromirrors for large attenuations.

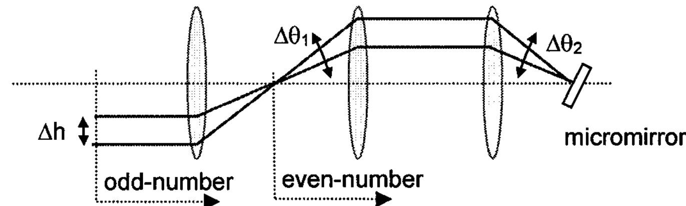

Figure 5.3: Odd vs. Even Number of Lens System

However, when an odd number of lenses are used in the configuration, the deflection angle at the micromirror will result in a lateral displacement of the beam at the output, as shown in Figure 5.3. Since a fiber core is typically 4 to 10 μm in diameter, small lateral misalignment between the beam and the core can result in large coupling loss, thus larger dynamic range is obtained for the same deflection range of the micromirrors.

5.1.2 Code V Modelling

Although the matrix optic approach allows one to quickly determine the parameters of the optical components of the equalizer system, more robust evaluation and diagnostic tools are required to properly characterize its performance. Code V, commercially available from Optical Research Associates [66], was used to this end.

Code V provides an array of analytical tools for the characterisation, optimization and evaluation of optical systems, ranging from simple first order analyses (paraxial ray tracing) to diffractive beam propagation.

The software tool provides significantly more insight into the behaviour of the optical system as the following factors are considered and simulated:

- **Ray diffraction at the redirection module:** Code V can model the behaviour of light as it is transformed and diffracted by grating elements. Grating

periodicity, spacing, and orientation are considered in the Code V simulations. Diffraction-based propagation techniques in conjunction with geometrical ray tracing are used to trace beam across the elements. Proper simulations and characterisations of the diffractive optical elements (DOEs) in the redirection module are important to ensure that the reformatting/redirection function of the equalizer is correctly designed and that the individual wavelength channels are properly spaced. Furthermore, the mapping from a linear array to a two-dimensional format causes small optical path length differences between the 64 channels. Consequently, variations in the attenuation-to-micromirror tilt response are observed between wavelengths. The modelling of the DOEs in Code V takes these differences into account.

- **Element Aperture and Transmittivity:** In the previous treatment of the optical elements of the equalizer module via geometrical ray tracing (Matrix Optics), an infinite aperture size is always assumed and the lens surfaces are considered perfectly transmissive. An evaluation of the efficiency of the equalizer system with these simplifications would underestimate the insertion loss. A finite aperture causes energy loss as the incident Gaussian beam is partially clipped. Although the lenses and the grating facets were designed such that 99% of the energy would be transmitted, small deviations in the optical path can significantly reduce this percentage if the Gaussian waists at the lenses are not within their designed values. A Code V simulation would take in to account these additional losses.

In Appendix C, the complete equalizer module, as illustrated in Figure 5.1, is described in Code V. The components' parameters: surface radius curvatures, refraction indexes, lens thickness, apertures, and lateral displacements are tabulated in the lens data manager. A quick visualization, Figure 5.4, provides a confirmation of the specified model. Here, only LENS3, DOE1, DOE2, LENS4, LENS5 and the micromirror are depicted for one wavelength (1.527 μm). Each channel is treated independently. Arrayed elements are

laterally displaced or decentered accordingly for each channel wavelength. The coordinates of the element (pitch) are obtained from the designed specifications.

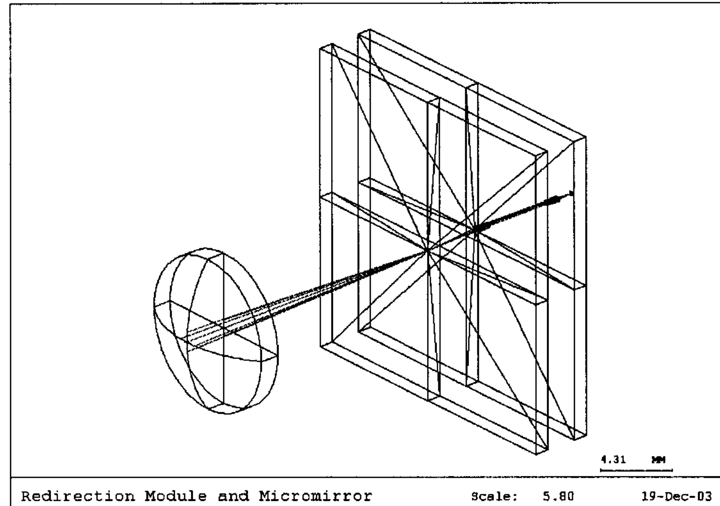

Figure 5.4: Code V System Model. LENS3, the redirection module, the microlenses and the micromirror are depicted.

5.1.2.1 Gaussian Beam Analysis

In the design of the equalizer module, the clear apertures and element separation distances are carefully chosen to guarantee that a Gaussian beam would propagate through the idealized system with beam clipped, in the worst case, at the 99% power waist radius. A beam waist analysis is thus first performed for the Code V model to ensure that the proper apertures and distances have been chosen.

Appendix C.3 tabulates the beam radius at the main surfaces of the equalizer system for an initial beam waist of 5.6 μm at the 1.527 μm wavelength. These parameters correspond to the beam originating from a signal mode fiber with a NA of 0.86. The beam radius is defined as the radius at which the beam carries 86 % of its energy. To ensure 99% power is transferred in ideal conditions, one must guarantee that the beam radius at a given surface is more than a 1/3 of the diameter of the clear aperture. Appendix C.3 confirms this for the $\lambda = 1.527$ μm channel; it is also so for the remaining 63 wavelengths. It is important to note that since a small optical path length difference exists between the 64 wavelengths, the waist positions and sizes throughout the system also varies slightly as the system was optimized for one center wavelength. The most

significant deviations are observed at the output surface (image plane). Figure 5.5 shows the output beam waist plotted against the starting waist size. Not shown are the corresponding variations of the waist position for all wavelengths.

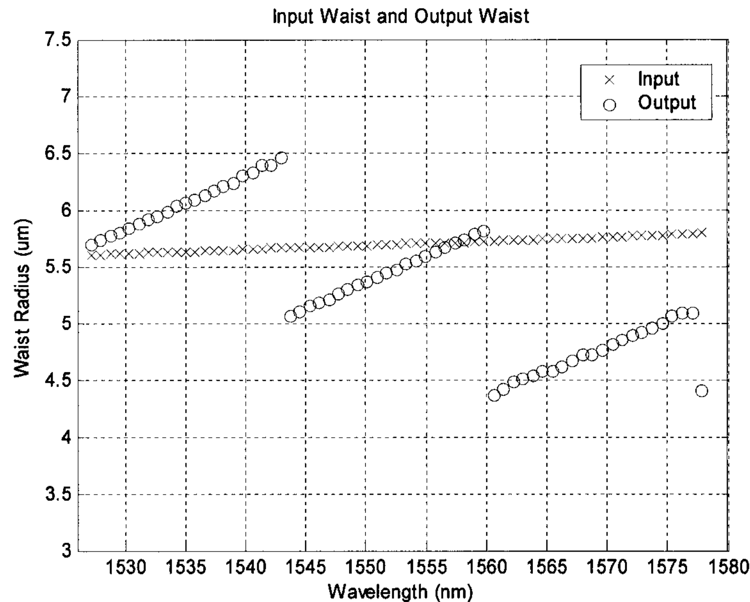

Figure 5.5: Beam Waist at Output Surface (SMF)

The variations in beam size increase the coupling loss such that the minimal insertion loss of the system is also increased. A more important impact of these variations is an observed increase in the wavelength dependence of the system. Although the change in waist size is significant, the overall impact on the calculation of the coupling at the fiber across of the wavelength is not as great at lower attenuation levels.

So far, the simulation assumed an ideal micromirror surface, although actual MEMS micromirror designs exhibit surface sag and curvature that will affect the propagation of the beam by focusing the incident light. However, results from the Gaussian beam analysis demonstrate that in the worst case scenario (radius of curvature R = 18.8 mm), the additional losses are not significant with beam waist changes of less than 2 %. The 99 % power transmission conditions are still met. These results also suggest that deformable membrane micromirrors (section 2.2.1) are not suited for our equalizer design. Cantilever or tiltable surface mirrors are required.

The Gaussian beam analysis has demonstrated that the optical parameters of the equalizer (focal length, aperture size, thickness and lens separation) were designed with sufficient flexibility such that throughput can be maximized and leeway is allowed for variations in the optical path lengths and the deformations of the MEMS micromirrors.

5.1.2.2 Coupling Loss vs. Tilt

As discussed, the variations in beam waist and position introduce a coupling loss at the fiber core; however it is the displacement of the reflected beam caused by the tilt of the micromirrors that is the primary mechanism for the dynamic control of the optical power attenuation. Lateral displacements of the beam centroid and, to a lesser extent, the angular displacements of the propagating axis reduce the coupling efficiency at the fiber by introducing mode mismatch between the Gaussian beam and the fiber core. Code V Real Ray Tracing option allows to measure these changes with respect to various micromirror tilts. Results are shown below, Figure 5.6, for the 64 wavelengths.

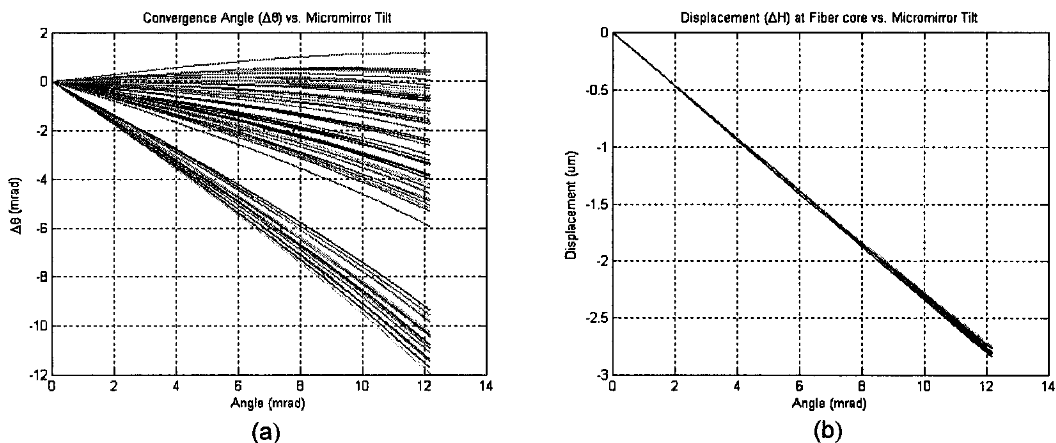

Figure 5.6: Lateral and Angular Displacements for Micromirror Tilt from 0 to 12 mrad

Note that linear angular and lateral displacements were obtained for the micromirror tilt range. From these results, an attenuation loss plot can be obtained by using an approach outlined by W.B. Joyce and B.C. DeLoach (Figure 5.7). Appendix D details the expressions used. In these calculations, the beam waist sizes and positions are included. These accentuate the wavelength dependence of the equalizer system. In the worst case scenario (at a high attenuation level, say -50 dB), the maximum difference in attenuation level between wavelength is 3.28 dB.

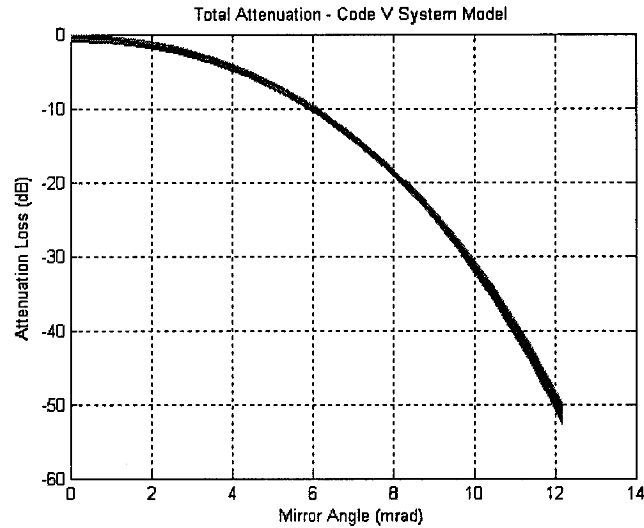

Figure 5.7: Attenuation Loss for Micromirror Tilt of 0 to 12 mrad

A few interesting observations should be noted here. Firstly, a large attenuation range (greater than 50 dB) is obtained for the small range of micromirror tilt of 12 mrad. Higher attenuation level can be obtained, at the cost of lower resolution. The system is very highly sensitive to the behaviour of the MEMS micromirrors. This sensitivity is due to the angular sensitivity of the diffractive optical elements and the relatively large number of optical elements in the systems. It also suggests that the alignment of the components is a greater concern to be dealt with. The inclusion of the telescoping lens system (LENS4 and LENS5) was purposely done to correct this sensitivity by reducing by a half the tilt of the micromirrors. Secondly, the loss is non-linear over the tilt range, but it is logarithmic with the wavelength dependence becoming more pronounced at higher attenuation levels. A constant attenuation resolution is not observed over the full range of operation. Thirdly, the equalizer system does not exhibit zero loss at zero tilt. Although a beam displacement is not observed, losses are incurred due to the Gaussian beam mode mismatch.

Table 5.3: Coupling Loss at Fiber (over all wavelengths)

Max Coupling Loss @ 0 mrad	0.8828 dB
Min Coupling Loss @ 0 mrad	0.000025 dB
Mean Coupling Loss @ 0 mrad	0.2744 dB

5.1.2.3 Efficiency

Generally, optical systems will have diffraction-based losses because of the finite aperture of the successive optical elements. The propagation of a clipped and aberrated Gaussian beam through the equalizer module can only be adequately characterized using diffraction-based propagation techniques, in conjunction with geometric ray tracing. In code V, this is done with the Beam Propagation (BPR) option.

The BPR option uses propagators that operate on the complex amplitude of the field distribution and produce the complex amplitude of the field distribution at different positions in the system. The propagators are the Fraunhofer (far field), the Fresnel (near field) and the sphere-to-sphere. Reference [67] contrasts their differences. Exact geometrical ray tracing is used to transfer the field intensity across optical interfaces (lenses, gratings, mirrors); while the appropriate propagator calculates the fields distribution in the distances between the interfaces. It is important to note that the Code V BPR option only propagates scalar field distributions. Therefore, polarization-dependent losses are not taken into account in the efficiency analysis.

Diffraction losses (beam clipping losses) are expected to be greatest at the grating elements (DOEs). Limitations imposed by the fabrication process of the diffraction optical gratings limit the accuracy of the grating periods, and consequently also limit the locations of the diffracted beam. Since the clear apertures of the elements are optimized to the 99% power Gaussian beam size requirements, the deviated beams cause larger than expected clipping losses.

Table 5.4 shows the percentage of power transferred at the various components in the system for a typical wavelength (1.527 μm).

Table 5.4: Loss Incurred at Various Equalizer Components at Zero Tilt

Source (SO)	100 % (0dB)
After LENS2 (S6)	97.9% (0.09dB)
After DOE1 (S8)	90.2% (0.44dB)
After DOE2 (S13)	63.4% (1.98dB)
After LENS3 (S16)	62.5% (2.04dB)
After LENS4 (S18)	58.5% (2.33dB)
At Micromirror (S19)	58.4% (2.34dB)
After LENS4 return (S21)	57.6% (2.40dB)
After LENS3 return (S23)	56.0% (2.52dB)
After DOE2 return (S25)	56.0% (2.52dB)
After DOE1 return (S30)	52.1% (2.83dB)
Image (SI)	52.0% (2.84dB)

As one would expect, the energy transfer efficiency from input fiber to the micromirror and back to the output fiber varies with both wavelength and micromirror tilt. Figure 5.8 shows the trends. The efficiency decreases with increased micromirror tilt, as the deflection of the light beam causes increased beam clipping at the optical element's limited aperture.

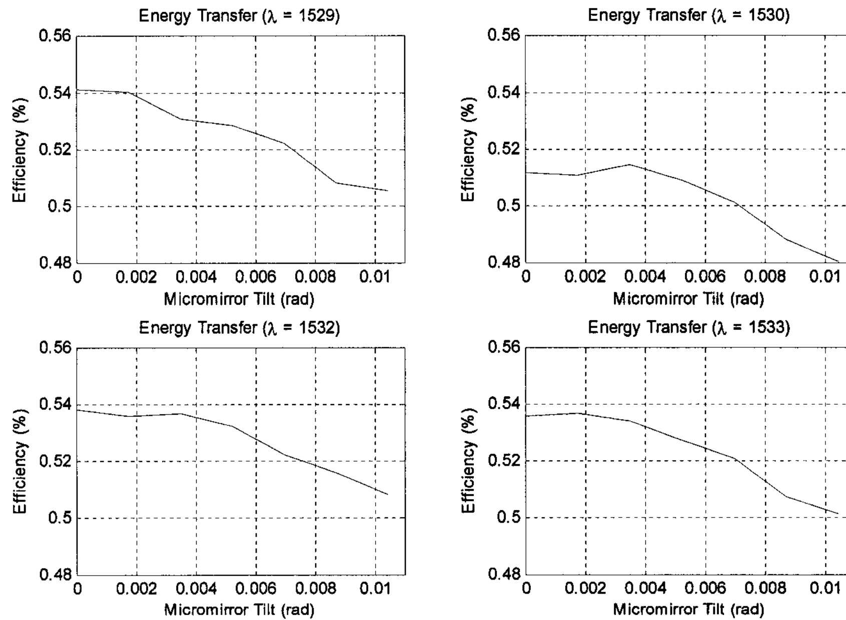

Figure 5.8: Energy Transfer for 4 Wavelengths and for micromirror tilt from 0 to 11 mrad

A periodicity in the efficiency over the channels is also observed. It is due that the periodicity in the arrangement of the wavelength on the diffractive element array (DOES2). Wavelengths are divided into four groups of 16 wavelengths, with each group

mapped onto a 4 x 4 array. The mapping results in periodicity in the optical path lengths and diffraction angles, which in turn affects the efficiency. Overall, peak energy transfer is calculated at 2.71dB with a mean value of 2.81 dB.

Table 5.5: Maximum and Minimum Energy Transfer

Peak Energy Transfer	53.6% (2.71dB)
Minimum Energy Transfer	50.2% (2.99dB)
Means Energy Transfer	52.3% (2.81dB)

Note that the efficiency of the grating is not accounted in these results. The simulation assumed 100% efficient grating.

5.1.3 Simulation Conclusions

The Gaussian beam trace, real ray trace and the diffractive beam propagation analyses have demonstrated that the numerical model of the equalizer module 1) exhibits a large attenuation range beyond the 50 dB requirement; 2) accommodates for the optical path differences between wavelength channels and the deformation of the micromirrors; 3) has a larger than required insertion loss and 4) exhibits a significant wavelength-dependent loss.

Improving the fabrication of the diffractive optical elements is the key factor in reducing the insertion loss of the equalizer system. The diffractive grating elements are traversed 4 times in the equalizer system by the incident light beam. Any efficiency improvements of the gratings will significantly impact the overall performance of the system. Better etching processes allowing for more precise diffractive grating parameters will minimise beam clipping.

5.2 Equalizer Experimental Characterisation

The numerical simulations of the system suggest that the equalizer would provide a good dynamic attenuation, although with significant losses. The losses are mainly attributed to the limitations in the fabrication process of the multifacet diffractive gratings and to a lesser extent to the micromirrors. However, the results indicate that the overall approach is appropriate, as a large attenuation range is obtained for small micromirror deflections. An assessment of the operations of the equalizer via experimental measurements was

attempted. In particular, measurements of the beam shape, beam lateral displacements and coupling loss (attenuation) were of interest. The measurement setup, shown in Figure 5.9, includes the components of the equalizers: the formatting lenses, the redirection module, and the micromirrors. The AWG is again replaced by two plano-aspherical lenses; while translation stages are used to displace the input fiber to the position of a given wavelength channel. Two beam splitter cubes are included, as shown, for component alignments and optical measurements. The alignment of the components is critical given the high sensitivity of diffractive optical elements to angular displacements. The positioning the beam on the facets of the DOEs and the micromirrors is done visually.

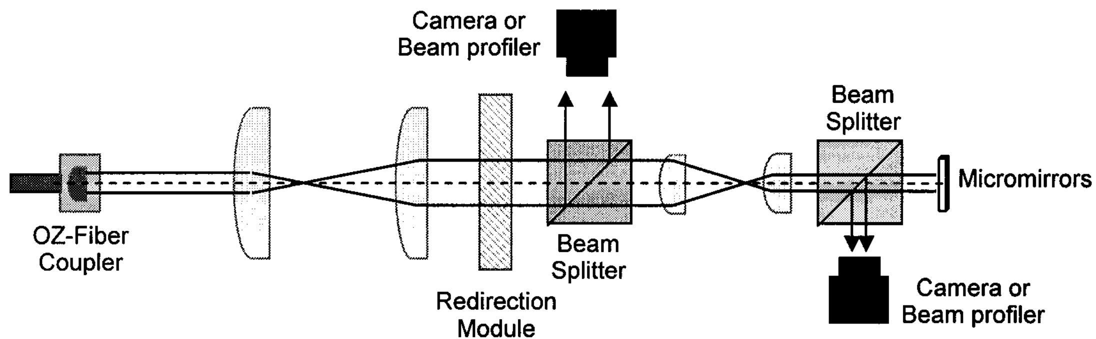

Figure 5.9: Experimental Setup

Two important limitations of the setup should be noted here. Firstly, the low efficiency of the 4-step grating causes a noticeable amount of incident optical power to remain in the 0th order diffraction beam, with limited power to the 1st order (order of interest). The 0th order beam propagates through the system and intervenes in the measurements. In earlier

experimental measurements, the efficiency of the redirection module was reported at only approximately 25% [5]. Secondly, due to the absence of a final annealing step in the fabrication of the micromirrors, the reflective surfaces are not metallized in order to maintain a more planar surface. Consequently, the reflectivity of the micromirrors is situated at about 2.66 dB, limiting the amount of power propagating back to the fiber. These two factors were proven to be critical.

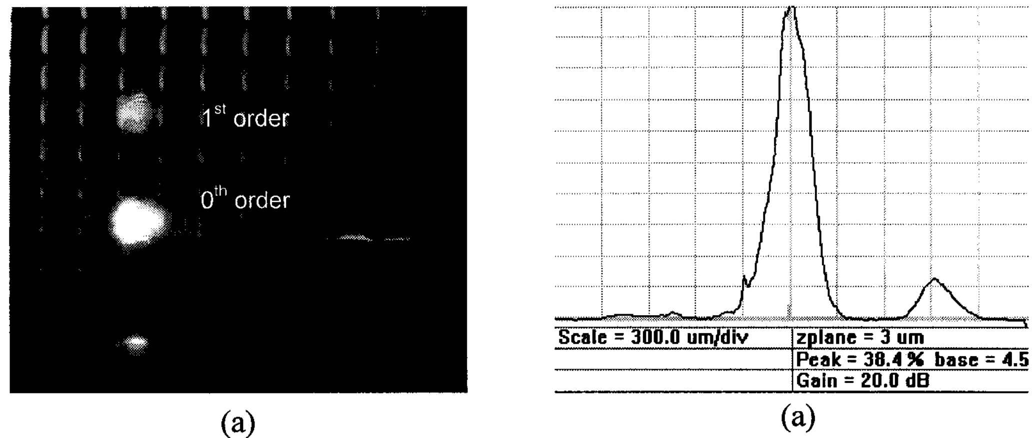

Figure 5.10: (a) Beam at DOE2's Position (b) Beam Profile at the Micromirror's Position

In Figure 5.10 (a), the placement of the beam on the facet of the diffractive optical element array is shown. Both the 0th and 1st order can be seen. The quality of the beam is also observed at various points in the system. Figure 5.10 (b) shows the profile of the beam at the micromirror's position. The 1st order beam exhibits a good Gaussian shape.

Unfortunately, no measurement of the lateral displacement introduced by the micromirror tilt or data for the coupling losses was obtained. With an input power of 15 mW, a clear signal could not be measured in the backward propagating direction at fiber position. Angular misalignments and the inefficiency of the redirection module and micromirrors were proven to be excessive. However, despite the lack of results, various areas of improvements of the components have been identified. These are discussed in the chapter to follow.

6 Conclusion

So far, we have presented the design of the equalizer module with characterisation results from the system numerical model. The suitability and performance of its components have been examined, with particular emphasis placed on the diffractive optical elements and the micromirrors. Experimental tests on these components indicate that their compactness and their flexibility are appropriate for the equalizer design. However, they also suggest that significant improvements can be realized by furthering the analysis and characterisation of the system in future works.

The evaluation of the micro-optic/micromirror approach to power equalization shows, so far, that the requirements outlined for an ideal equalizer module in section 1.1 are or can be met.

- **Dynamic power equalization**
  Inherent to the design of the equalizer, the real-time adjustment of the micromirror tilt allows for dynamic power equalization. However, further works are required to implement a feedback system.
- **High sensitivity/high resolution**
  Future work are required to precisely determine the resolution of the equalizer, however, similar designs [16] reported in the literature are capable of high resolution (0.1 dB). A similar sensitivity is expected for this design.
- **Scalable from 64 to 128, and 256 channels**
  The use of diffractive optical element array allows for easy integration of 64, 128 and 256 channels in an efficient 2-dimensional format. Similarly, micromirror array can be easily designed for large channel counts.
- **0-50 dB attenuation range**
  With current design, an attenuation of over 50 dB is obtained for micromirror tilt of 12 mrad (or at 8V).
- **Low minimum insertion loss and low polarization-dependent loss**
  Major losses in the system occur at the redirection module due to the inefficiency of the gratings and limitation of the fabrication process. However, micromirrors

are efficient reflectors (0.29 dB). Polarization-dependent loss is measured at 1.5 dB [5] for the dispersion/redirection module. PDL for the micromirrors are negligible. Many of these losses are due to the quality of the manufactured components. Access to optimized fabrication process would allow the design to meet the requirements.

- **Fast response and attenuation stability**

  The response time and sensitivity of the equalizer design have not yet been studied. The response time of equalization will be determined by how fast the micromirrors can adjust to the changing power levels. This can usually be done in the microsecond range of MEMS micromirrors reported in the literature. Note that the micromirrors are not switched in digital fashion from on/off positions, which can be slow, but in an analog fashion. Stability is determined by how well the micromirror responds to the analog control signal.

- **Off-power state stability**

  The current design does not incorporate off-power state stability. A different design for the micromirrors, in which the tilt angle is maintained after the removal of power, can be incorporated.

- **Robust, cost efficient, thermally stable and packageable design**

  The module design is suitable for efficient packaging. The AWG can be integrated onto a single PLC. The redirection module can be moulded as a single component and integrated with the microlenses and micromirrors arrays. The MEMS components can be reliable with past designs passing million-cycle switching tests [68].

6.1 Future Work

Future work for this project should focus on three areas: 1) further characterisation, in particular cross-talk and tolerance analysis of the equalizer model and of the realized system, 2) improvements in the design of the diffractive optical elements and the micromirrors and 3) packaging of the system and the integration of a feedback control system. These three areas are described in greater details in the next sections.

6.1.1 Cross-Talk Analysis and Tolerancing

In section 5.1, the path of light as it traverses the equalizer module, from the formatting lenses, through the DOEs to the micromirrors (and visa versa) is examined to determine the final displacement of the beam position at the input/output fiber core. Stray rays have not yet been considered. Due to finite apertures, particularly at the DOEs, light from one channel can leak into neighbouring channels. In an ideal system, i.e. in which all components are perfectly aligned, the power leakage is designed to be at most 1 % at each aperture (section 5.1.2.1). The overall effect of the cross-talk is a reduction in the efficiency and dynamic range of the system. It would be important to measure this power loss and more critically to minimise it. Necessarily, this leads to the issue of alignment or assembly tolerances. In [5], a discussion of the tolerances and alignment features included in the design of the DOEs to facilitate assembly is presented. An extension of this discussion to include the alignment requirements between the AWG, DOEs, microlenses, and micromirrors should be done. Future designs should also include alignment features on all components to simplify assembly.

One key issue to be examined in these future analyses is the uniformity of loss attributed to cross-talk and misalignment across the 64 wavelengths. Angular displacements of the components affect differently the wavelengths that are spatially arrayed. Any wavelength-dependent losses in the system require additional feedback control circuitry to compensate for the non-uniformity.

6.1.2 Improved Diffractive Optical Elements and Micromirror Designs

Significant portions of this thesis were dedicated to the discussion of the diffractive optical elements (redirection module) and the micromirrors. Cross-talk, efficiency, PDL, and uniformity are primarily determined by the characteristics of the DOES, while the micromirrors determine the response time, the sensitivity, and attenuation range of the equalizer. Because of their predominant roles, an optimization of these components would be highly sought. Considerable improvements have been identified for future works.

Improved redirection modules can be implemented via off-axis Fresnel lenses, increased phase or step levels and optimized grating etch depth. Reference [5] offers further discussions of these improvements. Future micromirror designs should be optimized for the range of operation (tilt) by extending the pull-in condition, increasing the thickness of the reflective surface to minimise surface sag and curvature, and lowering the operating voltage. Silicon-on-insulator fabrication technology may offer the means to achieve these improvements [69] [70] [71]. Future works should focus on determining the resonance frequency and response time of the micromirrors. It is important to note that designing fast micromirrors would necessarily limit the former improvements. Large, thick micromirrors with large electrode-surface gap are slower. A balance must be struck.

6.1.3 Dynamic Feedback Control and Integration

Wavelength dependencies in the equalizer module are non-negligible. Losses between the 64 channels can differ as much as 3.0 dB (at high attenuation level). That is, to equalize the 64 wavelengths, the micromirrors are individually adjusted to the lowest optical power level of the 64 channels. This approach decreases the overall insertion loss of the system. A feedback control system is evidently needed to set and maintain the output power level for all wavelength channels, as illustrated in Figure 6.1.

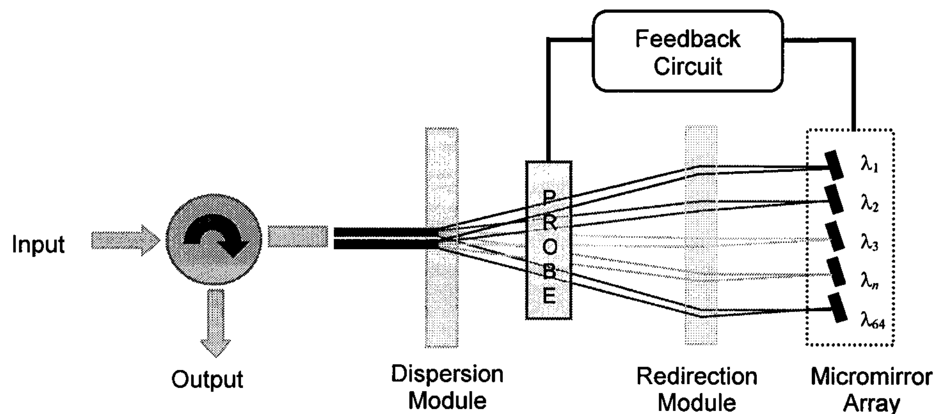

Figure 6.1: Feedback System

With such a control system, the optical power level of each wavelength is measured, compared to a reference or desired level and the required micromirror electrode voltages are determined. Future works are required to investigate the technologies and techniques

for implementing the power meter probe, to design the control electronic circuitry, and to solve the problem of their integration.

A packageable equalizer design was sought in this project: the 2-D formatting and the use of micromirror arrays allow for a compact module design. However, the device assembly and packaging remain an issue to be dealt with in future work. In particular, and pertaining to the tolerancing, alignment features would be needed on all components (AWG, DOES, microlens and micromirror array) to facilitate assembly. Alternatively, plastic injection moulding technologies can be considered for commercial fabrication of aligned redirection and microlens modules. The packaging must provides thermal stability and reliability at a reduced cost.

6.2 SUMMARY

In the present thesis, the design of a compact optical power equalizer is presented. The need for power equalization is warranted by the wavelength dependencies of the many operations (amplification, switching, channel add/drop) that a signal undergoes in an optical network. EDFA gain spectrums are non-uniform over the signals' bandwidth, losses during multiplexing and switching vary from one wavelength to another, and the performance of the optical receiver is sensitive to the signal power levels. The control and regulation the optical power alleviate these problems and can optimize the performance of an optical interconnection to meet the increasing demand for bandwidth.

The survey of existent and proposed equalizer technologies has been presented. The approach to power equalization presented in this work is best suited to meet the requirements for telecommunication applications:

- large dynamic power attenuation range
- high resolution
- large (64) channel number and scalable channel count
- low insertion loss and low polarization loss
- fast, sensitive, and stable response
- robust design that provides thermal stability, cost efficiency and easy packaging

The approach taken utilizes arrayed-waveguide gratings and diffractive optical elements to (de)multiplexed the incoming signal, and more importantly also to spatially format the 64 wavelengths into a compact two-dimensional array. Micromirrors are then used to redirect the individual wavelength to cause small changes in the optical path that result in power attenuation at the input/output fiber. An optical fiber circulator and telescope microlenses are added to allow for the retrieval of the back propagating output signal and to increase the stability and sensitivity of the power attenuation, respectively. The 2-D implementation offers many advantages: compactness, ease of integration of the micro-optics and micromirrors, and efficient packaging.

The implementation technologies for the primary components of the equalizer were investigated; however, the micromirror design and analysis have been emphasized because of their importance in the overall performance of the equalizer module. MUMPs surface-micromachined rotational micromirrors were shown to exhibit the necessary characteristics for the equalizer application: 0.29 dB means surface reflectivity at λ = 1.527 μm to 1.578 μm, small surface curvature and low operating voltage (less than 15V). The maximum tilt of the best performing micromirror is limited to 16 mrad; however, system simulations indicated that this is sufficient for an attenuation range of over 50 dB.

Code V numerical simulations were performed on a simplified model of the equalizer module to study the loss mechanism and the optical efficiency of the system components. Gaussian beam analysis confirmed that the lens parameters were correctly chosen, while ray tracing analyses tracked the propagation path of the beam as it traverses the system. From these results, the attenuation at the fiber core can be plotted against the micromirror tilt (or electrode voltage). Diffraction analyses indicated that the efficiency of the diffractive optical elements is low and requires improvements. Overall, the mean efficiency (assuming 100% efficient grating) is 2.81 dB with minimum variation of 0.28 dB over the C-band wavelengths. At high attenuation levels, this variation grows to 3 dB. To these values, one needs to add the loss of the optical circulator (1.7 dB), the AWG (0.7 dB) and the micromirrors (0.29 dB). Improvements are possible in various areas to minimise losses. 1-3 dB insertion loss would be realisable.

The results suggest that the compact equalizer implemented via the 2-dimensional arrayed micro-optics and micromirrors is advantageous. Large attenuation can be obtained from a small and compact module. Areas requiring continued analyses and improvements have been identified for future works. Assembly, tolerance and packaging require further studies, while efficiency can be improved in new designs for the micro-optics and micromirrors.

Appendix A Micromirror Chip Layout

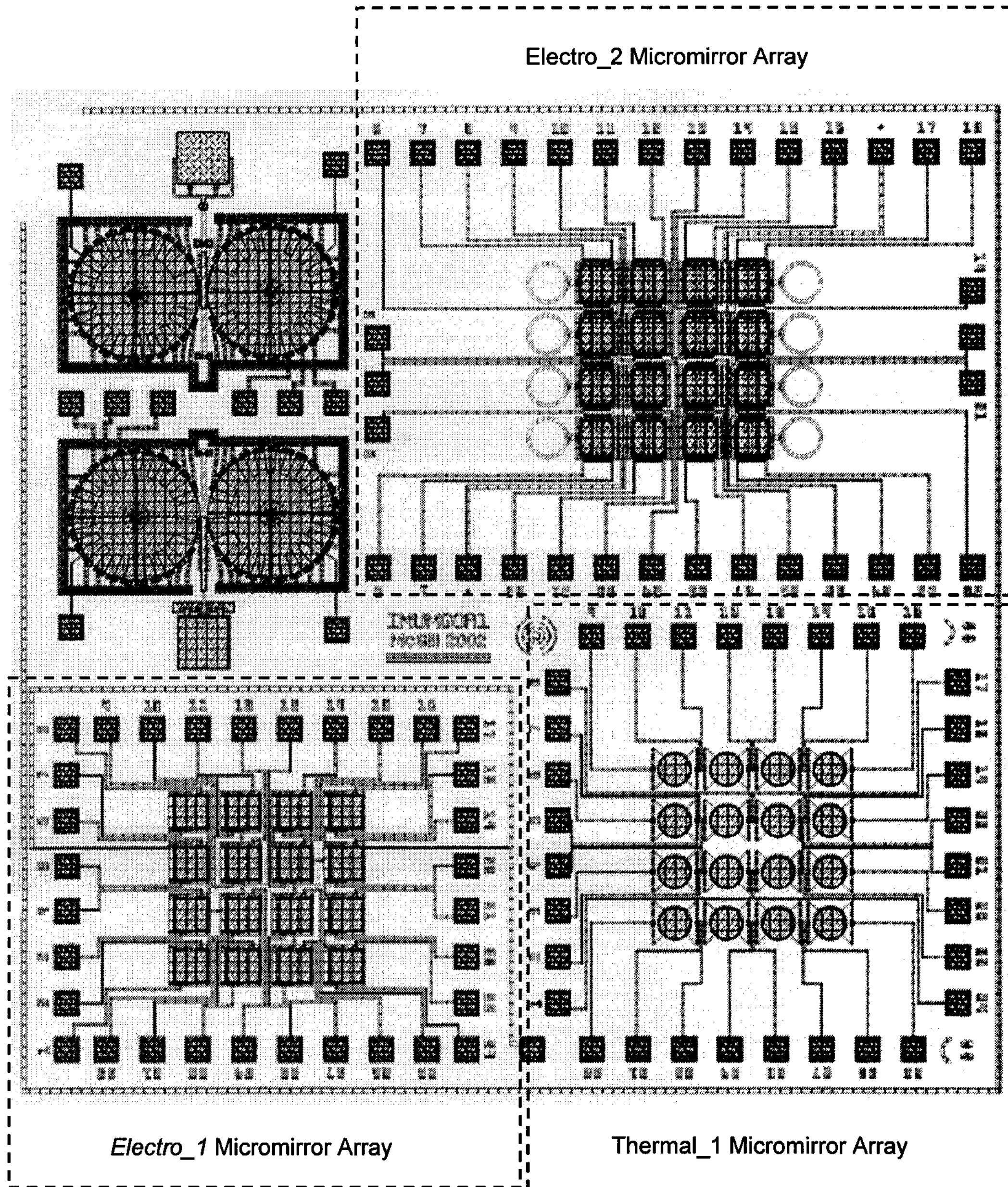

Figure A.1: MEMS Micromirror Layout

Appendix B Matrix Analysis

For a given optical system, such as that of the optical equalizer system (Figure B.1) composed of multiple thick lenses, the propagation of a light ray can be treated as a ray traversing a series of successive surface separated by a medium with a reflection index n.

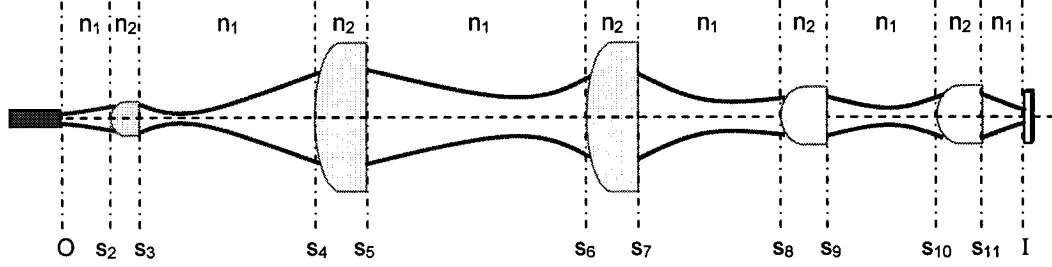

Figure B.1: Lens System

It is convenient to represent these optical interfaces or elements as matrices. The technique, referred to as matrix optics [72], is both flexible and powerful. With this approach, a light ray is described by its position h and its angle u with respect to the optical axis. These parameters are altered as the ray travels through the system. They are represented as:

$$Input\ Ray = \begin{bmatrix} h_i \\ u_i \end{bmatrix} \qquad \text{Eq. B.1}$$

The optical system is represented by a transfer matrix $M = \begin{bmatrix} A & B \\ C & D \end{bmatrix}$, and the output ray is given by $\begin{bmatrix} h_o \\ u_o \end{bmatrix} = \begin{bmatrix} A & B \\ C & D \end{bmatrix} \cdot \begin{bmatrix} h_i \\ u_i \end{bmatrix}$.

The matrix M for a spherical boundary surface between two media with indexes n_1, n_2 and a radius of curvature R is given by $s = \begin{bmatrix} 1 & 0 \\ -(n_2 - n_1)/n_2 R & n_2/n_1 \end{bmatrix}$, while that of a propagation thickness d is $t = \begin{bmatrix} 1 & d_1 \\ 0 & 1 \end{bmatrix}$.

In a system where deflection occurs, the matrix approach requires that the deflection angle be added to the angle of the ray.

$$deflection = +\begin{bmatrix} 0 \\ 2\alpha \end{bmatrix} \qquad \text{Eq. B.2}$$

For a complex system, the cascade components are successively multiplied to obtain the overall system matrix.

→ M_1 → M_2 → ... → M_n $\qquad M = M_n \ldots M_2 M_1$

For the equalizer optical system, the matrix formulation is given as follows, where the subscript r refers to the return (reversed) optical path. A micromirror tilt of α is assumed.

$$\begin{bmatrix} h_o \\ u_o \end{bmatrix} = \begin{bmatrix} a_r & b_r \\ c_r & d_r \end{bmatrix} \cdot \left(\begin{bmatrix} 1 & 0 \\ -(n_2 - n_1)/n_2 R & n_2/n_1 \end{bmatrix} \cdot \begin{bmatrix} 1 & d_1 \\ 0 & 1 \end{bmatrix} \cdot \{\ldots\} \cdot \begin{bmatrix} 1 & d_1 \\ 0 & 1 \end{bmatrix} \cdot \begin{bmatrix} h_i \\ u_i \end{bmatrix} + \begin{bmatrix} 0 \\ 2\alpha \end{bmatrix} \right)$$

This equation can be readily coded in Matlab. In order to determine the distances d, the propagation of a Gaussian beam through the system is considered. Minimum waist positions are found, corresponding to the required values of d.

A Gaussian beam is defined by two parameters: its waist size and its radius of curvature, both varying with distance x.

$$\varpi^2(x) = \varpi_0^2 \left[1 + \left(\frac{\lambda x}{\pi \varpi_0^2} \right)^2 \right] \qquad \text{Eq. B.3}$$

$$R(x) = x \left[1 + \left(\frac{\pi \varpi_0^2}{\lambda x} \right)^2 \right] \qquad \text{Eq. B.4}$$

It is possible to use the ABCD matrix approach to compute changes in these two parameters as the beam traverses an optical system. However, $\omega(x)$ and $R(x)$ do not transform as h and u do for simple rays; rather they are transformed via a complex bi-linear transformation given by

$$q_{out} = \frac{[q_{in} A + B]}{[q_{in} C + D]} \qquad \text{Eq. B.5}$$

where the new parameter q is given by

$$\frac{1}{q(x)} = \frac{1}{R(x)} - \frac{j\lambda}{\pi\varpi^2(x)} \qquad \text{Eq. B.6}$$

With this method, the waist positions in the optical system can be determined. The distances d are then adjusted to coincide with the minimal points.

Appendix C   Code V

C.1 Lens Data Manager

Surface #	Surface Name	Surface Type	Y Radius	Thickness	Glass	Refract Mode	Y Semi-Aperture	X Semi-Aperture
Object		Sphere	Infinity	6.2000		Refract		
Stop	Collimator	Sphere	2.7548	1.0000	FSV CORNING	Refract	2.0000	2.0000
2		Sphere	Infinity	505.4900		Refract	2.0000	2.0000
3	LENS1	Sphere	222.1580	3.0000	FSV CORNING	Refract	6.2500	6.2500
4		Sphere	Infinity	516.4229		Refract	6.2500	6.2500
5	LENS2	Sphere	8.2198	3.0000	FSV CORNING	Refract	5.0000	5.0000
6		Sphere	Infinity	16.4200		Refract	5.0000	5.0000
7	DOE1a	Grating	Infinity	0.0000		Refract	0.0313	0.0313
8	DOE1b	Grating	Infinity	0.0000		Refract	0.0313	0.0313
9		Sphere	Infinity	1.0000	FSV CORNING	Refract	10.0000	10.0000
10	Spacer	Sphere	Infinity	2.0947		Refract	10.0000	10.0000
11		Sphere	Infinity	1.0000	FSV CORNING	Refract	10.0000	10.0000
12	DOE2a	Grating	Infinity	0.0000		Refract	0.1250	0.1250
13	DOE2b	Grating	Infinity	0.0000		Refract	0.1250	0.1250
14		Sphere	Infinity	0.0000		Refract	4.2835	4.2835
15	LENS3	Sphere	1.5551	1.0000	FSV CORNING	Refract	0.1250	0.1250
16		Sphere	Infinity	4.5576		Refract	0.1250	0.1250
17	LENS4	Sphere	0.7775	1.0000	FSV CORNING	Refract	0.1250	0.1250
18		Sphere	Infinity	1.0600		Refract	0.1250	0.1250
19	mems	Sphere	Infinity	-1.0600		Reflect	0.1250	0.1250
20		Sphere	Infinity	-1.0000	FSV CORNING	Refract	0.1250	0.1250
21	LENS4 r	Sphere	0.7775	-4.5576		Refract	0.1250	0.1250
22		Sphere	Infinity	-1.0000	FSV CORNING	Refract	0.1250	0.1250
23	LENS3 r	Sphere	1.5551	0.0000		Refract	0.1250	0.1250
24	DOE2b r	Grating	Infinity	0.0000		Refract	0.1250	0.1250
25	DOE2a r	Grating	Infinity	0.0000		Refract	0.1250	0.1250
26		Sphere	Infinity	-1.0000	FSV CORNING	Refract	10.0000	10.0000
27	Spacer r	Sphere	Infinity	-2.0947		Refract	10.0000	10.0000
28		Sphere	Infinity	-1.0000	FSV CORNING	Refract	10.0000	10.0000
29	DOE1b r	Grating	Infinity	0.0000		Refract	0.0313	0.0313
30	DOE1a r	Grating	Infinity	0.0000		Refract	0.0313	0.0313
31		Sphere	Infinity	-16.4200		Refract	4.0893	4.0893
32		Sphere	Infinity	-3.0000	FSV CORNING	Refract	5.0000	5.0000
33	LENS2 r	Sphere	8.2198	-516.4229		Refract	5.0000	5.0000
34		Sphere	Infinity	-3.0000	FSV CORNING	Refract	6.2500	6.2500
35	LENS1 r	Sphere	222.1580	-505.4900		Refract	6.2500	6.2500
36		Sphere	Infinity	-1.0000	FSV CORNING	Refract	2.0000	2.0000
37	Collimator r	Sphere	2.7548	-6.2000		Refract	2.0000	2.0000
Image		Sphere	Infinity	0.0000		Refract	5.0000	5.0000

End Of Data

C.2 System Visualization

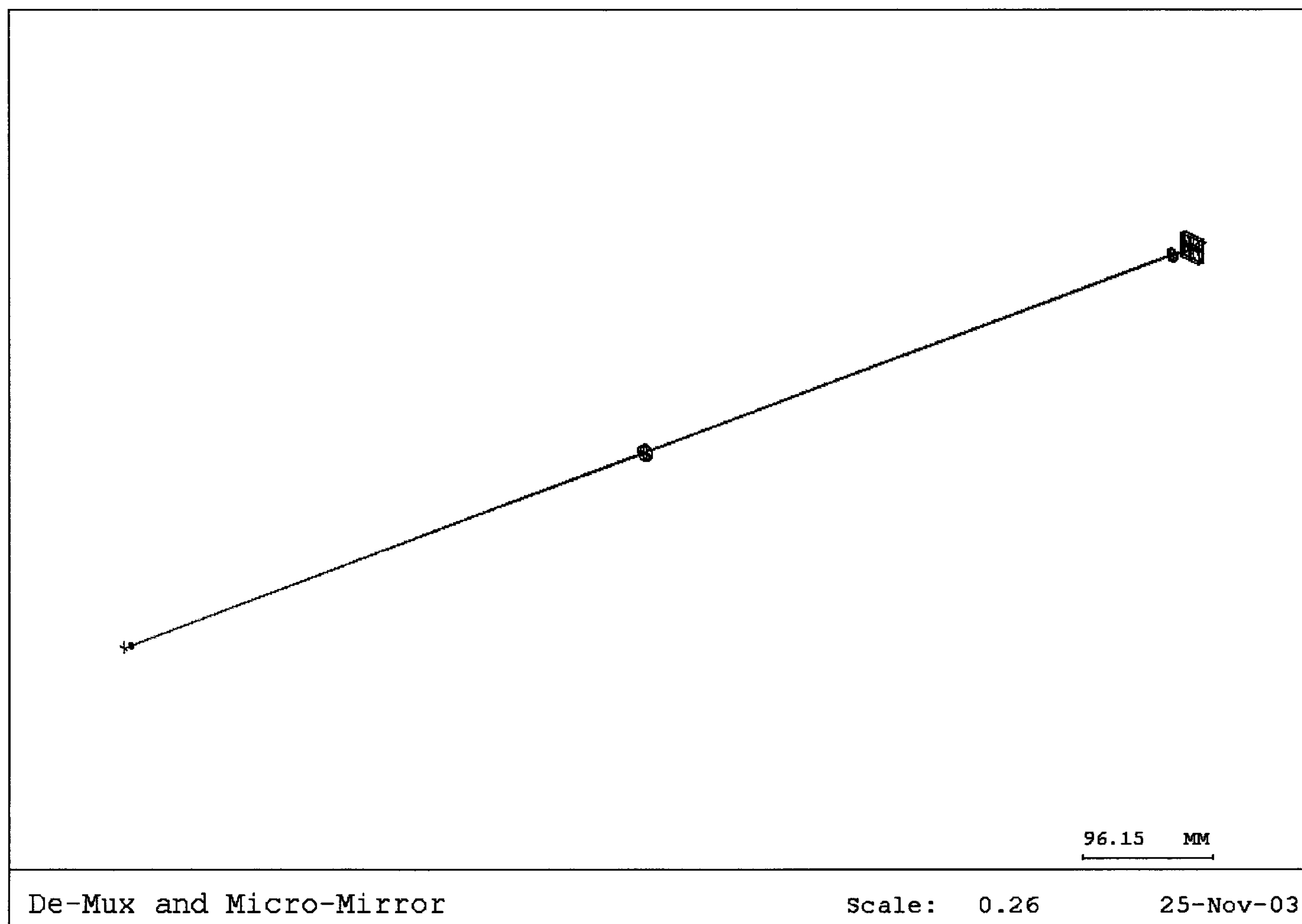

Figure C.1: Code V Visualisation of Equalizer System

C.3 Waist Analysis

C.3.1 Waist Size in System (with no Micromirror Curvature)

SURFACE	DESCRIPTION	APERTURE (mm)	X BEAM WAIST (mm)	Y BEAM WAIST (mm)
Object	Fiber core	NA	0.0056	0.0056
S1	Collimator (Front)	2.5 (radius)	0.5382	0.5382
S2	Collimator (Back)	2.5 (radius)	0.5382	0.5382
S3	Lens1 (Front)	6.25 (radius)	0.7029	0.7029
S4	Lens1 (Back)	6.25 (radius)	0.7012	0.7012
S5	Lens2 (Front)	5.0 (radius)	0.4520	0.4520
S6	Lens2 (Back)	5.0 (radius)	0.4014	0.4014
S7	DOE1a	0.03125 (semi-edge)	0.0199	0.0199
S8	DOE1b	0.03125 (semi-edge)	0.0199	0.0199
S9	Substrate of DOE1	10.0 (semi-edge)	0.0199	0.0199
S10	Spacer	NA	0.0262	0.0261
S11	Substrate of DOE2	10.0 (semi-edge)	0.0717	0.0711
S12	DOE2a	0.125 (semi-edge)	0.0882	0.0875
S13	DOE2b	0.125 (semi-edge)	0.0882	0.0875
S14 *	Separation (dummy)	NA	0.0882	0.0875
S15	Lens3 (Front)	0.125 (semi-edge)	0.0882	0.0875
S16	Lens3 (Back)	0.125 (semi-edge)	0.0873	0.0868
S17	Lens4 (Front)	0.125 (semi-edge)	0.0858	0.0861
S18	Lens4 (Back)	0.125 (semi-edge)	0.0523	0.0527
S19	Micromirror	0.125 (semi-edge)	0.0100	0.0100
S20	Lens4 (Back)	0.125 (semi-edge)	0.0531	0.0527
S21	Lens4 (Front)	0.125 (semi-edge)	0.0865	0.0861
S22	Lens3 (Back)	0.125 (semi-edge)	0.0862	0.0867
S23	Lens3 (Front)	0.125 (semi-edge)	0.0868	0.0875
S24	DOE2b	0.125 (semi-edge)	0.0868	0.0875
S25	DOE2a	0.125 (semi-edge)	0.0868	0.0875
S26	Substrate of DOE2	10.0 (semi-edge)	0.0868	0.0875
S27	Spacer	NA	0.0703	0.0711
S28	Substrate of DOE1	10.0 (semi-edge)	0.0253	0.0261
S29	DOE1b	0.03125 (semi-edge)	0.0200	0.0199
S30	DOE1a	0.03125 (semi-edge)	0.0200	0.0199
S31*	Separation (Dummy)	NA	0.0200	0.0199
S32	Lens2 (Back)	5.0 (radius)	0.4028	0.4014
S33	Lens2 (Front)	5.0 (radius)	0.4535	0.4521
S34	Lens1 (Back)	6.25 (radius)	0.6769	0.7006
S35	Lens1 (Front)	6.25 (radius)	0.6786	0.7023
S36	Collimator (Back)	2.5 (radius)	0.5400	0.5382
S37	Collimator (Front)	2.5 (radius)	0.5400	0.5383
Image	Fiber core	NA	0.0056	0.0056

N.B. *"radius" refers to the radius of a circular aperture and "semi-edge", to the semi-length of a square aperture.*
** These surfaces are construct surfaces and do not represent real interfaces in the system*

C.3.2 Waist Size in System (Micromirror Curvature R = 18.8mm)

SURFACE	DESCRIPTION	APERTURE (mm)	X BEAM WAIST (mm)	Y BEAM WAIST (mm)
Object	Fiber core	NA	0.0056	0.0056
S1	Collimator (Front)	2.5 (radius)	0.5382	0.5382
S2	Collimator (Back)	2.5 (radius)	0.5382	0.5382
S3	Lens1 (Front)	6.25 (radius)	0.7029	0.7029
S4	Lens1 (Back)	6.25 (radius)	0.7012	0.7012
S5	Lens2 (Front)	5.0 (radius)	0.4520	0.4520
S6	Lens2 (Back)	5.0 (radius)	0.4014	0.4014
S7	DOE1a	0.03125 (semi-edge)	0.0199	0.0199
S8	DOE1b	0.03125 (semi-edge)	0.0199	0.0199
S9	Substrate of DOE1	10.0 (semi-edge)	0.0199	0.0199
S10	Spacer	NA	0.0262	0.0261
S11	Substrate of DOE2	10.0 (semi-edge)	0.0717	0.0711
S12	DOE2a	0.125 (semi-edge)	0.0882	0.0875
S13	DOE2b	0.125 (semi-edge)	0.0882	0.0875
S14 *	Separation (Dummy)	NA	0.0882	0.0875
S15	Lens3 (Front)	0.125 (semi-edge)	0.0882	0.0875
S16	Lens3 (Back)	0.125 (semi-edge)	0.0873	0.0868
S17	Lens4 (Front)	0.125 (semi-edge)	0.0858	0.0861
S18	Lens4 (Back)	0.125 (semi-edge)	0.0523	0.0527
S19	Micromirror	0.125 (semi-edge)	0.0100	0.0100
S20	Lens4 (Back)	0.125 (semi-edge)	0.0533	0.0529
S21	Lens4 (Front)	0.125 (semi-edge)	0.0868	0.0864
S22	Lens3 (Back)	0.125 (semi-edge)	0.0859	0.0864
S23	Lens3 (Front)	0.125 (semi-edge)	0.065	0.0871
S24	DOE2b	0.125 (semi-edge)	0.0865	0.0871
S25	DOE2a	0.125 (semi-edge)	0.0865	0.0871
S26	Substrate of DOE2	10.0 (semi-edge)	0.0865	0.0871
S27	Spacer	NA	0.0700	0.0707
S28	Substrate of DOE1	10.0 (semi-edge)	0.0250	0.0258
S29	DOE1b	0.03125 (semi-edge)	0.0200	0.0199
S30	DOE1a	0.03125 (semi-edge)	0.0200	0.0199
S31*	Separation (Dummy)	NA	0.0200	0.0199
S32	Lens2 (Back)	5.0 (radius)	0.4037	0.4020
S33	Lens2 (Front)	5.0 (radius)	0.4544	0.4526
S34	Lens1 (Back)	6.25 (radius)	0.6697	0.6931
S35	Lens1 (Front)	6.25 (radius)	0.9714	0.6948
S36	Collimator (Back)	2.5 (radius)	0.5405	0.53284
S37	Collimator (Front)	2.5 (radius)	0.5405	0.5384
Image	Fiber core	NA	0.0056	0.0056

N.B. "radius" refers to the radius of a circular aperture and "semi-edge", to the semi-length of a square aperture.
** These surfaces are construct surfaces and do not represent real interfaces in the system*

C.3.3 Comparison of Waist (% Change)

SURFACE	DESCRIPTION	APERTURE (mm)	X-WAIST % CHANGE	Y-WAIST % CHANGE
Object	Fiber core	NA	0.00	0.00
S1	Collimator (Front)	2.5 (radius)	0.00	0.00
S2	Collimator (Back)	2.5 (radius)	0.00	0.00
S3	Lens1 (Front)	6.25 (radius)	0.00	0.00
S4	Lens1 (Back)	6.25 (radius)	0.00	0.00
S5	Lens2 (Front)	5.0 (radius)	0.00	0.00
S6	Lens2 (Back)	5.0 (radius)	0.00	0.00
S7	DOE1a	0.03125 (semi-edge)	0.00	0.00
S8	DOE1b	0.03125 (semi-edge)	0.00	0.00
S9	Substrate of DOE1	10.0 (semi-edge)	0.00	0.00
S10	Spacer	NA	0.00	0.00
S11	Substrate of DOE2	10.0 (semi-edge)	0.00	0.00
S12	DOE2a	0.125 (semi-edge)	0.00	0.00
S13	DOE2b	0.125 (semi-edge)	0.00	0.00
S14 *	Separation (dummy)	NA	0.00	0.00
S15	Lens3 (Front)	0.125 (semi-edge)	0.00	0.00
S16	Lens3 (Back)	0.125 (semi-edge)	0.00	0.00
S17	Lens4 (Front)	0.125 (semi-edge)	0.00	0.00
S18	Lens4 (Back)	0.125 (semi-edge)	0.00	0.00
S19	Micromirror	0.125 (semi-edge)	0.00	0.00
S20	Lens4 (Back)	0.125 (semi-edge)	0.38	0.38
S21	Lens4 (Front)	0.125 (semi-edge)	0.35	0.35
S22	Lens3 (Back)	0.125 (semi-edge)	0.35	0.35
S23	Lens3 (Front)	0.125 (semi-edge)	0.35	0.46
S24	DOE2b	0.125 (semi-edge)	0.35	0.46
S25	DOE2a	0.125 (semi-edge)	0.35	0.46
S26	Substrate of DOE2	10.0 (semi-edge)	0.35	0.46
S27	Spacer	NA	0.43	0.56
S28	Substrate of DOE1	10.0 (semi-edge)	1.19	1.15
S29	DOE1b	0.03125 (semi-edge)	0.00	0.00
S30	DOE1a	0.03125 (semi-edge)	0.00	0.00
S31*	Separation (dummy)	NA	0.00	0.00
S32	Lens2 (back)	5.0 (radius)	0.22	0.15
S33	Lens2 (Front)	5.0 (radius)	0.20	0.11
S34	Lens1 (Back)	6.25 (radius)	1.06	1.07
S35	Lens1 (Front)	6.25 (radius)	1.06	1.07
S36	Collimator (Back)	2.5 (radius)	0.09	1.00
S37	Collimator (Front)	2.5 (radius)	0.09	0.02
Image	Fiber core	NA	0.00	0.00

N.B. *"radius" refers to the radius of a circular aperture and "semi-edge", to the semi-length of a square aperture.*
** These surfaces are construct surfaces and do not represent real interfaces in the system*

Appendix D Gaussian Beam – Fiber Coupling

The efficiency of the optical transmission or the coupling of light into a single model fiber can be analysed as the coupling between two Gaussian beams. In [73], W. B. Joyce and B. C. DeLoach describe this analysis in details. In this section, the main ideas and equations of the approach are outlined and applied to the equalizer module design.

In the equalizer module, optical power loss or attenuation occurring at the fiber core is controlled by the degree of alignment between the Gaussian mode of the single mode fiber and that of the returning light beam, schematically shown in Figure D.1.

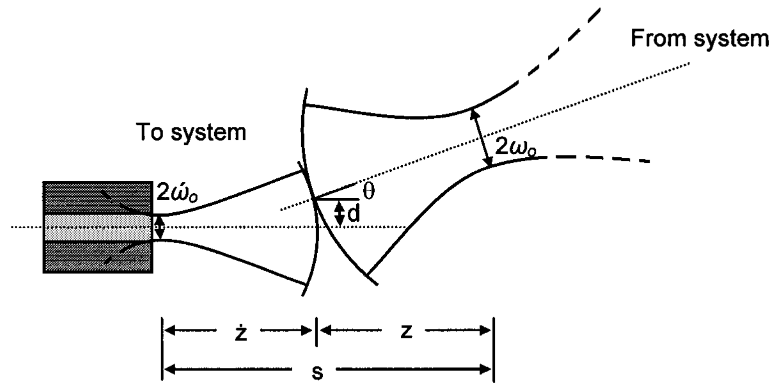

Figure D.1: Generalized Fiber Coupling with Lateral and Angular Misalignments

The coupling efficiency or the power transmissivity of the equalizer system at the minimum zero attenuation level, i.e. zero micromirror tilt (d = 0 and θ =0) is given as by Eq. D.1 and Eq. D.2, where T_α is the transmissivity. The loss incurred for this aligned case is caused by the mode mismatched between the Gaussian beams, and consequently the waist separation s. $\dot{\omega}$ and ω are the Gaussian waist sizes.

$$\tau_\alpha = \frac{2}{\left[(\dot{\omega}_o/\omega_o + \omega_o/\dot{\omega}_o)^2 + (2/k\dot{\omega}_o\,\omega_o)^2 s^2\right]^{1/2}} \qquad \text{Eq. D.1}$$

$$T_\alpha = \tau_\alpha^2 \qquad \text{Eq. D.2}$$

As the micromirrors are tilted, the returning Gaussian beam exhibits both an angular θ and lateral d displacement. The additional loss can be calculated from Eq. D.3 – Eq. D.6. Note that the loss from the mode mismatched is included in these expressions.

$$T_\theta = T_\alpha \exp[-\theta/\theta_e] \qquad \text{Eq. D.3}$$

$$\theta_e = \frac{2^{1/2}}{\pi\tau_\alpha\left[(\dot{\omega}/\lambda)^2 + (\omega/\lambda)^2\right]^{1/2}} \qquad \text{Eq. D.4}$$

$$T_d = T_\alpha \exp\left[-(d/d_e)^2\right] \qquad \text{Eq. D.5}$$

$$d_e = \frac{2^{1/2}}{\tau_\alpha\left(1/\dot{\omega}_o^2 + 1/\omega_o^2\right)^{1/2}} \qquad \text{Eq. D.6}$$

The transmittivity of the system with loss from the misalignment of the incident Gaussian beam is simply given as follow:

$$dB(T) = dB(T_d) + dB(T_\alpha). \qquad \text{Eq. D.7}$$

References

Chapter 1: Introduction

[1] A. M. Odlyzko, "Internet Traffic Growth: Sources and Implications," University of Minnesota, Minneapolis, MN, USA. 2003.

[2] D.V. Plant, "Agile all-photonic networks," *Lasers and Electro-Optics Society, 2003. LEOS 2003, The 16th Annual Meeting of the IEEE*, vol. 1, p. 227, October 2003.

[3] D. J. Farber, "Predicting the unpredictable: future directions in internetworking and their applications," *Communications Magazine, IEEE*, vol. 30, iss. 7, July 2002.

[4] G. P. Agrawal, "Optical Receivers" in *Fiber-Optic Communication Systems*, chapter 4, sec 4.5,Wiley-Interscience, New York, NY, 1997.

[5] F. Thomas-Dupuis, "Investigation of Two-Dimensional Optical Formatting for Dense Wavelength Division Multiplexing," *Master Thesis, McGill University*, November 2002.

Chapter 2: Literature Review

[6] T.C. Kowalczyk, I. Finkelshtein, M. Kouchmir, Y.C. Lee, A.-D. Nguyen, D.Vroom, and W.K. Dischel, "Variable Optical with Large Dynamic Range and Low Drive Power," *Optical Fiber Communication Conference and Exhibit, 2001.* OFC 2001, vol. 3, pp.WR5-1-WR5-4, 2001.

[7] S.M. Garner, and S. Caracci, "Variable Optical Attenuation for Large-Scale Integration," *IEEE Photonics Technology Letters*, vol. 14, no. 11, pp. 1560-1562, November 2002.

[8] S.-S. Lee, Y.-S. Jin, Y.-S. Son, and T.-K Yoo, "Polymeric Tunable Optical Attenuator with an Optical Monitoring Tap for WDM Transmission Network," *IEEE Photonics Technology Letters*, vol. 11, no. 5, pp. 590-592, May 1999.

[9] C. R. Doeer, C.H. Joyner, and L.W. Stulz, "Integrated WDM Dynamic Power Equalizer with Potentially Low Insertion Loss," *IEEE Photonics Technology Letters*, vol. 10, no. 10, pp. 1443-1445, October 1998.

[10] N.S. Lagali, J.F.P. van Nunen, D. Pant, and L. Eldada, "Ultra-Low Power and High Dynamic Range Variable Optical Attenuator Array," *Proc. 27th Conf. on Opt. Comm. ECOC'01- Amsterdam*, pp. 430-431, 2001.

[11] M. Zirngibl, C. H. Joyner, and B. Glance, "Digitally Tunable Channel Dropping Filter/Equalizer Based on Waveguide Grating Router and Optical Amplifier Integration," *IEEE Photonics Technology Letters*, vol. 6, no. 4, pp. 513-515, April 1994.

[12] M. Zirngibl, "An Optical Power Equalizer Based on One Er-Doped Fiber Amplifier," *IEEE Photonics Technology Letters*, vol. 4, no. 4, pp. 357-359, April 1992.

[13] S. Kim, and S. Nam, "Novel MEMS Variable Optical Attenuator with Expanded Core Waveguides," *2002 IEEE/LEOS International Conference on Optical MEMS*, pp. 65-66, August 2002.

[14] B. Barber, C.R. Giles, V. Askyuk, R.Ruel, L. Stulz, and D. Bishop, "A Fiber Connectorized MEMS Variable Optical Attenuator," *IEEE Photonics Technology Letters,* vol. 10, no.9, pp. 1262-1264, September 1998.

[15] Aksyuk et al. (Lucent Technology), "Optical Attenuator," *United States Patent,* Patent No. US6173105B1, January 2001.

[16] B. M. Anderson, S. Fairchild, and N. Thorsten, "MEMS Variable Optical Attenuator for DWDM Optical Amplifiers," *Optical Fiber Communication Conference 2000*, vol. 2, pp. 7-10, March 2000.

[17] S. Sumriddetchkajorn, and N. "Micromachine-based Fault-Tolerant High Resolution High-Speed Programmable Fiber-Optic Attenuator," *Optical Fiber Communication Conference 2000*, vol. 3, pp. 240-242, March 2000.

[18] C. Marxer, B. de Jong, and N. de Rooif, "Comparison of MEMS Variable Optical Attenuator Designs," *2002 IEEE/LEOS International Conference on Optical MEMS*, pp.189-190, August 2002.

[19] N.A. Riza, and Z. Yaqoob, "Submicrosecond Speed Variable Optical Attenuator Using Acousto-optics," *IEEE Photonics Technology Letters*, vol. 13, no. 7, pp. 693-695, July 2001.

[20] M.J. Mughal and N. A. Riza, "65 dB Dynamic Range 2.8 Microseconds Switching Speed Variable Fiber-Optic Attenuator," *27th European Conference on Optical Communication*, vol. 6, September 2001.

[21] MEMS and MOEMS Technology and Applications, P. Rai-Chaoudhury, ed., SPIE Press, Bellingham, WA, 2000.

[22] L.J. Hornbeck, "128x128 Deformable Mirror Devices," *Trans. IEEE Electron Devices,* vol. ED-30, pp. 539-545, May 1983.

[23] R.N. Thomas, J. Guldberg, H.C. Nathanson, P. R. Malmberg, "The Mirror-Matrix Tube: A Novel Light Valve for Projection Display," *Trans. IEEE Electron Devices*, vol. ED-22, pp. 765-775, September 1975.

[24] K.E. Petersen, "Silicon Torsional Scanning Mirror," *IBM J. Res. Develop.*, vol. 24, pp. 631-637, September 1980.

[25] P.F. Van Kessel, L. J. Hornbeck, R.E. Meier, and M. R. Douglass, "A MEMS-Based Projection Display," *Proc. of the IEEE*, vol. 86, pp. 1687-1704, August 1998.

Chapter 3: Micro-optics and Micromirror-based Equalizer

Optical Circulators

[26] N. Sugimoto, T. Shintaku, A. Tate, H. Terui, M. Shinmokozono, E. Kubota, M. Ishii, and Y. Inoue, "Waveguide Polarization-Independent Optical Circulator," *IEEE Photonics Technology Letters*, vol. 11, no. 3, pp. 355-357, March 1999.

[27] M. Koga and T. Matsumoto, "High-Isolation Polarization-Insensitive Optical Circulator for Advanced Optical Communication Systems," *Journal of Lightwave Technology*, vol. 10, no. 9, pp. 1210-1217, September 1992.

[28] http://fiber-optics.globalspec.com/Industrial-Directory/optic_circulator.

[29] T. Sonobe and H. Fujita, "PLC-Optical Circulattor and Isolator Based on Blazed Diffractive Grating," *in Proc. Conf. on Solid State Sensors, Actuators and Microsystems, Boston,* pp. 583-586, June 2003.

[30] Y. Fujii, "High-Isolation Polarization-Independent Quasi-Optical Circulator," *Journal of Lightwave Technology,* vol. 10, no. 9, pp. 1226-1229, September 1992.

Arrayed-Waveguide Gratings

[31] M.K. Smit, and C.V. Dam, "PHASAR-based WDM: Principals, Design and Applications," *IEEE Journal of Selected Topics in Quantum Electronics*, vol. 2, no2, pp.236-241, June 1996.

[32] H. Takahashi, S. Suzuki, K. Kato and I. Nishi, "Arrayed-Waveguide Grating for Wavelength Division Mult/Demultiplexer with Nanometer Resolution," *Electronics Letters*, vol. 26, no. 2, pp. 87-88, January 1990.

[33] Y. Hibino, "Recent Advances in High-Density and Large-Scale AWG Multi/Demultiplexers With Higher Index-Contrast Silica-Based PLCs," *IEEE Journal of Selected Topics in Quantum Electronics*, vol. 8, no. 6, pp. 1090-1101, November 2002.

[34] D. V. Plant, and A. G. Kirk, "Optical Interconnects at the Chip and Boar Level: Challenges and Solutions," *Proc. of the IEEE*, vol. 88, no.6, pp. 806-818, June 2000.

[35] N. A Riza, and S. Sumriddetchkajorn, "Two Dimensional Digital Micromirror Device-based 2 x 2 Fiber-Optics Switch Array," *Lasers and Electro-Optics Society Annual Meeting, IEEE*, vol. 2 , pp.413-414, December 1998.

Chapter 4: MEMS Micromirrors

[36] P. J. French, "Basic Micromachining Fabrication Processes," *in MEMS and MOEMS Technology and Applications*, pp.14-19, SPIE Press, Washington, 2000.

[37] M.R. Dokmeci, S. Bakshi, M. Waeli, A. Pareek, C. Fung, and C. H. Mastrangelo, "Bulk micromachined electrostatic beam steering micromirror array," *Optical MEMS, 2002. Conference Digest. 2002 IEEE/LEOS International Conference on*, pp. 15-16, August 2002.

[38] J. Yun-Ho, and K. Yong-Kweon, "Design and fabrication of a micromirror using silicon bulk micromachining for out-of-plane right angle reflection," *Optical MEMS, 2002. Conference Digest. 2002 IEEE/LEOS International Conference on*, pp. 79-80, August 2002.

[39] W. Sun, J. Mugha, F. Perez, W. Noell, N.A. Riza, and N.F. de Rooij, "A bulk micromachined tiltable mirror array digital variable optical attenuator," *TRANSDUCERS, Solid-State Sensors, Actuators and Microsystems, 12th International Conference on*, vol. 2 , pp. 1772-1775, June 2003.

[40] S. Kyoung, C. Young-Ho, Y, Sung-Kie, "A bulk-micromachined silicon micromirror for tunable optical switch applications," *Emerging Technologies and Factory Automation, 1996. EFTA '96. Proceedings., 1996 IEEE Conference on*, vol.2 , pp. 404-407, November 1996.

[41] T. G. Bifano, P.A. Bierden, S.A. Cornelissen, C.E. Dimas, H. Lee, M.H. Miller, and J. Perreault, J. A., "Large-scale metal MEMS mirror arrays with integrated electronics," *Proc. SPIE Vol. 4755, Design, Test, Integration, and Packaging of MEMS/MOEMS 2002*, Bernard Courtois, Jean Michel Karam, Karen W. Markus, Bernd Michel, Tamal Mukherjee, James A. Walker; Eds., pp. 467-476, April 2002.

[42] J.-H. Lee, Y.-C. Ko, B.-S. Choi, J.-M. Kim, and D. Y Jeon, "SOI-fabrication of scanning mirror for laser display," *Optical MEMS, 2002. Conference Digest. 2002 IEEE/LEOS International Conference on*, pp. 153-154, August. 2002.

[43] D.S. Greywall, P.A. Busch, F. Pardo, D.W. Carr, G. Bogart, and H.T. Soh, "Crystalline silicon tilting mirrors for optical cross-connect switches,", *Journal of Micro-electromechanical Systems*, vol. 12, pp.708-714, October 2003.

[44] H. Yi-Ping, W. Mingching, L. Hung-Yi, and Fang, W., "A robust and reliable stress-induced self-assembly mechanism for optical devices," *Optical MEMS, 2002. Conference Digest. 2002 IEEE/LEOS International Conference on*, pp. 131-132, August 2002.

[45] M. A. Michalicek, and V.M. Bright, "Flip-chip fabrication of advanced micromirror arrays," *Micro Electro Mechanical Systems, 2001. MEMS 2001. The 14th IEEE International Conference on*, pp. 313-316, January 2001.

[46] J.H. Comtois, M.A. Michalicek, N. Clark, W. Cowan, "MOEMS for adaptive optics," *Broadband Optical Networks and Technologies: An Emerging Reality/Optical MEMS/Smart Pixels/Organic Optics and Optoelectronics. 1998 IEEE/LEOS Summer Topical Meetings*, pp. II/95 - II/96, July 1998.

[47] M.A. Michalicek, and J.H. Comtois, and C.C. Barren, "Design and characterisation of next-generation micromirrors fabricated in a four-level, planarized surface-micromachined polycrystalline silicon process," *in Proceedings of the Second Annual IEEE International Conference on Innovative Systems in Silicon, 1997,* pp. 144-154, October 1997.

[48] H. Dooyoung, S. Huang, H. Nguyen, H. Chang, M.C Wu, H. Toshiyoshi, "A low voltage, large scan angle MEMS micromirror array with hidden vertical comb-drive actuators for WDM routers," *Optical Fiber Communication Conference and Exhibit, 2002. OFC 2002*, pp.92-93, March 2002.

[49] D.A. Koester, R. Mahadevan, B. Hardy and K. W. Markus, "MUMPs Design Handbook," Revision 7, Cronos Integrated Microsystems, 3026 Cornwallis Rd, Research Triangle Park, NC 27709, 2001.

[50] B. E. A. Saleh, and M. C. Teich, "Chapter 2: Beam Optics," in *Fundamentals of Photonics*, Wiley, New York, 1991.

[51] W. D. Cowan, and V.M. Bright, "Thermally Actuated Piston Micromirror Arrays," *Proc. SPIE*, vol. 3131, pp. 260-271, 1997.

[52] J. Ford, "Telecommunications with MEMS devices: an overview," *Lasers and Electro-Optics Society, 2001. LEOS 2001. The 14th Annual Meeting of the IEEE*, vol. 2, pp. 415-416, November 2001.

[53] O. Degani, E. Socher. A. Lipson, T. Leitner, D. J. Setter, S. Kaldor, and Y. Nemirosky, "Pull-In Study of an Electrostatic Torsion Micro-actuator," *Journal of Micro-electromechanical Systems*, vol. 7, pp. 373-379, December 1998.

[54] W. N. Sharpe, B. Yuan, R. Vaidyanathan, and R. L. Edwards, "Measurements of Young's Modulus, Poisson's Ratio, and Tensile Strength of Polysilicon," *IEEE Proceeding of the Annual International Workshop on Micro Electro Mechanical Systems MEMS '97*, pp. 424-429, January 1997.

[55] W. N. Sharpe, Kamili. M. Jackson, K. J. Hemker, and Z. Xie, "Effect of Specimen Size on Young's Modulus and Fracture Strength of Polysilicon," *Journal of Micro-electromechanical System*, vol. 10, pp. 317-325, September 2001.

[56] S. Moaveni, "Finite Element Analysis: Theory and Application with ANSYS," Prentice Hall, New Jersey, 1999.

[57] P. P. Silvester, and R. L. Ferrari, "Finite Elements for Electrical Engineers," Third Edition, Cambridge University Press, Great Britain, 1996.

[58] ANSYS, Inc. 275 Technology Drive, Canonsburg, PA 15317.

[59] W. D. Cowan and V. M. Bright, "Thermally Actuated Piston Micromirror Arrays," *Proc. SPIE*, vol. 3131, pp. 260, 1997.

[60] "Chapter 5.9 Electromechanical Transducers," ANSYS 7.1 Documentation, Theory Reference, ANSYS Inc., Southpointe, Canonsburg, PA 15317, 2003.

[61] V. Sharma, "Enhanced Vertical Scanning Interferometry," Honours Thesis, McGill University, Montreal, April 2002.

[62] "Technical Discussions: Aberrations," IntelliWave™ User Manual, Engineering Synthesis Design, Inc., pp. 188-190, 2000.

[63] Y.-A. Peter, F. Gonte, H.P. Herzig, and R. Dandliker, "Micro-optical fiber switch for a large number of interconnects using a deformable mirror," *Photonics Technology Letters, IEEE*, vol. 14, pp. 301-303, March 2002.

[64] J. Zou, M. Balberg, C. Byrne, C. Liu, and D. J. Brady, "Optical Properties of Surface-micromachined Mirrors with Etch Holes," *IEEE Journal of Micro-electromechanical Systems*, vol. 8, pp. 506-513, December 1999.

Chapter 5: Equalizer Modelling and Characterisation

[65] OZ Optics – HPUC-23-1500-S6.2AS, http://www.ozoptics.com/dSheeets/noncontact_style.pdf

[66] Optical Research Associates, 3280 East Foothill Boulevard, Suite 300, Pasadena, California 91107-3103.

[67] Optical Research Associates, "*BPR - Diffraction-Based Beam Propagation,*" Code V Help, 2002.

Chapter 6: Conclusion

[68] A. Jazairy, J.H. Smith, S.S. Nasiri, J. Bryzek, A.F. Flannery, M.J Novack, R. Sprague, and D. Skurnik, " Design for reliability of high voltage, high density interconnects for MOEMS mirror drive electrodes," *Optical MEMS, 2002. Conference Digest. 2002 IEEE/LEOS International Conference on*, pp. 19-20 August 2002.

[69] D.S. Greywall, P.A. Busch, F. Fardo, D.W. Carr, G. Bogart, and H. T. Soh, "Crystalline Silicon Tilting Mirror for Optical Cross-Connect Switches," *Journal of Microelectromechanical Systems,* vol. 12, pp.708-712, October 2003.

[70] V. Milonović, G.A. Matus, T. Cheng, and B. Cagdaser, "Monolithic High Aspect Ratio Two-Axis Optical Scanners in SOI," *16th IEEE Int. Micro-electromechanical Systems Conf. Kyoto* Japan, January 2002.

[71] P. R. Patterson, D. Hah, H. Nguyuen, H. Toshiyoshi, R. Chao, and M.C. Wu, "A Scanning Micromirror with Angular Comb Drive Actuation" *15th IEEE International Conference on Micro Elecrro Mechanical Systems (MEMS 2002), Las Vegas, USA*, January 2002.

Appendices

[72] B.E.A. Saleh, and M.C. Teich, "Fundamentals of Photonics," Chapter 1.4, pp.26-36, Wiley-Interscience, New York, 1991.

[73] W. B. Joyce, and B.C DeLoach, "Alignment of Gaussian Beams," *Appl. Opt.*, vol. 23, no. 23, pp. 4187-4196, December 1984.